Numerical studies of Quantum Lattice Systems

by

Alexios Michailidis

Thesis submitted to the University of Nottingham for the degree of Doctor of Philosophy, November 2016

Abstract

The research work in this thesis is based on strongly interacting quantum lattice systems. The biggest part of research was conducted using state-of-the-art tensor network simulations. Tensor networks provide efficient and highly accurate representations of quantum states when any simply connected patch of the quantum state is slightly entangled. Matrix Product States (MPS) is a tensor network representation for quantum states which is quasi-exact for one-dimensional systems ($d = 1$) when entanglement entropy of any bipartition of the state follows "area-law", i.e. $S \propto L^{d-1}$. Projected Entangled Pair States (PEPS) is the extension of MPS for higher dimensional systems, where entanglement entropy area-law is non-trivial. These formalisms and their relevant ground state optimization techniques, Density Matrix Renormalization Group (DMRG) for MPS and Simple Update (SU) with Tensor Renormalization Group (TRG) for PEPS are thoroughly analysed.

Entanglement entropy area-law is usually obeyed by the ground state of local Hamiltonians, while generic highly excited states follow a volume-law (they span a finite part of the Hilbert space). Recently, a class of interacting system was shown to undergo a dynamical phase transition (Many Body Localization) where the entropy of every eigenstate follows an area-law. This transition is achieved when the system is highly disordered and the quantum many body state becomes localized similarly to the free particle Anderson localization. The area-law property makes highly excited eigenstates of Many Body Localized (MBL) systems efficiently represented by the MPS ansatz. We develop a highly optimized algorithm (eDMRG) which goes beyond ground state optimization and successfully target eigenstates in any part of the spectrum. This algorithm is used together with analytical calculations, based on local integrability of MBL systems, to identify the universal behaviour of the entanglement spectrum of highly excited eigenstates in MBL systems.

In the second part we study interacting bosons in 2D optical lattices. Strongly interacting bosons are simulated using the Bose-Hubbard (BH) model when the interactions are strictly local and the Extended Bose-

Hubbard (EBH) model, when additional dipolar interactions are present. The ground states of BH/EBH Hamiltonians in a hexagonal lattice are studied. The phase spectrum includes various insulating and critical phases which are studied in detail using infinite-PEPS ansatz. Additional results on entanglement entropy scaling with respect to the filling of the lattice are presented.

Finally, a strongly interacting Harper-Hofstadter Hamiltonian is realized by combining synthetic fields with the BH model. The homogeneity of the system is then broken by a parabolic trapping potential, similar to the ones used in cold atom experiments. Using time-dependent Gutzwiller ansatz (GA) the expansion dynamics of the cloud in large square lattices are studied. In contrast to the expansion dynamics of the BH model, it is found that the synthetic fields generate a self-trapping effect. Using phenomenology and simulations the dynamics are studied in the hard-core and soft-core limit.

Manuscripts

Maksym Serbyn, **Alexios A. Michailidis**, Dmitry A. Abanin, and Z. Papić, 2016. Power-Law Entanglement Spectrum in Many-Body Localized Phases, Phys. Rev. Lett. 117, 160601.

Acknowledgements

Undertaking this PhD has been a valuable experience for me and it would not have been possible to do without the support that I received from various people.

Colleagues from the office for valuable discussions about physics and beyond, as well as various activities.

Dr. Keith Benedict as my principal supervisor for funding my PhD and proofreading this thesis.

Prof. Mark Fromhold as my secondary supervisor for discussions during the first period of my PhD.

Dr. Yury Kosevich for valuable and insightful discussions about physics during the first period of my PhD which is not included in this thesis.

Dr. Maksym Serbyn for creative discussions, ideas and collaboration that contributed significantly to my progress in science.

Dr. Zlatko Papić for introducing me to the fascinating concept of many body localization and for his support and guidance. Our discussions contributed significantly to my understanding of many body physics.

To my parents for providing unwavering support in all steps of my life.

More importantly, to Maria's support during the period of our PhDs. Sharing the past four years with her was a pleasure and a lot of fun. Her patience and support during the last steps of my writing was one of a kind.

Contents

1 Efficient representations for slightly entangled states 1

1.1 The Many Body State 2

1.1.1 State Definition 2

1.1.2 Quantum Entanglement 3

1.2 1D: Matrix Product States 5

1.2.1 Matrix Product Operators 11

1.2.2 Density Matrix Renormalization Group 12

1.2.3 Abelian symmetries 16

1.2.4 Current State of MPS 17

1.3 Beyond 1D 19

1.3.1 State Optimization: Simple Update 21

1.3.2 State Contraction: Tensor Renormalization Methods 26

1.3.3 Progress on Tensor Renormalization methods 31

2 Entanglement of arbitrary excited eigenstates in Many Body Localized systems 32

2.1 Many-Body localization 33

2.1.1 Local integrals of Motion 34

2.2 Variational MPS optimization for arbitrary excited eigenstates: eDMRG algorithm 39

2.2.1 eDMRG validation and error sources 41

2.3 Entanglement spectrum of MBL eigenstates 47

2.3.1 Entanglement structure of MBL Eigenstates 47

2.3.2 Entanglement structure of resonant MBL eigenstates 52

2.4 Discussion 57

3 Strongly interacting bosons in 2-dimensional lattices 59

3.1 Strongly interacting Bosons in optical lattices 60

3.1.1 From Continuum to Lattice 60

3.1.2 Physics of the Ground State (T=0) 63

3.2 iPEPS approximation of the ground state 69

3.2.1 Bose-Hubbard model 70

3.2.2 Extended Bose-Hubbard model 72

3.2.3 Discussion 77

3.3 Cloud expansions of the strongly interacting Harper-Hofstadter Hamiltonian 79

3.3.1 Time evolution protocol 82

3.3.2 Hard-core regime: $\rho < 1$ 83

3.3.3 Soft-core regime: $\rho > 1$ 87

3.3.4 Discussion 89

Outline **92**

4.1 Summary 92

4.2 Future Work 93

Appendix A Reduced-Rank-Randomized Singular Value Decomposition **95**

Appendix B Shift-invert algorithm **99**

Appendix C Gutzwiller ansatz and Mean Field theory **104**

C.1 Mean field theory 104

C.1.1 Mott Insulator-Superfluid boundary 105

C.2 Gutzwiller ansatz 106

C.2.1 Ground state optimization 107

C.2.2 Time-Dependent Gutzwiller Ansatz 109

C.2.3 Trapped boson gasses 111

References **113**

Chapter 1

Efficient representations for slightly entangled states

Chapter 1 provides an introduction of the sophisticated numerical methods which are used throughout this thesis. These methods are a class of Tensor Networks which can efficiently represent quantum states that share a common property, namely, entanglement entropy area-law. The area-law characterizes the complexity of quantum states and is often satisfied by eigenstates of physically interesting systems. The states that satisfy area-law can be efficiently represented in the thermodynamic limit by classical computers. More specifically, in section 1.1 the Hilbert space is introduced and quantum entanglement is described as a measure of the complexity of pure states in the Hilbert space. Additionally, the entanglement spectrum (ES) is defined as a complexity measure that goes beyond entropies and in certain cases it is sensitive to information indistinguishable to entropy measurements. In section 1.2, the Matrix-Product-State (MPS) ansatz is introduced, as a natural ansatz for states that obey area-law. The celebrated Density-Matrix-Renormalization-Group (DMRG) algorithm [1], is introduced as an efficient method for ground state optimization using MPS ansatz. In section 1.3, MPS formalism is generalized to higher dimensions, namely Projected-Entangled-Pair-States (PEPS)[2]. As MPS naturally reproduce the area-law in 1D, PEPS naturally reproduce the area-law in higher dimension. Additional difficulties arising in higher dimensions are discussed. A simple algorithm for ground state optimization of PEPS based

on Vidal's work [3] and an algorithm for calculation of correlation functions based on the Tensor-Renormalization-Group (TRG) [4] are discussed.

1.1 The Many Body State

1.1.1 State Definition

The behaviour of complex vectors (states) in a Hilbert space is the object of interest in many body physics, as it encapsulates all the information of an isolated quantum system. In this thesis, the focus is placed upon lattice systems. The basis of states is built within the framework of second quantization: For each site i, we define a local d-dimensional Hilbert space $\mathscr{H}_i$ with an orthonormal basis $\{|n_i\rangle\,, n_i \leq d\}$, which contains all local degrees of freedom. An orthonormal basis for the full Hilbert space of N sites $\mathscr{H} = \otimes^N \mathscr{H}_i$, consists of the set of Fock states $\mathscr{F} = \{\prod_i \sum_{n_i} |n_i\rangle\,, i \leq N, n_i \leq d\}$.

For example, in case of bosons or fermions, n_is are occupation numbers of particles, while in case of s $= 1/2$ spins, n_is usually denote the eigenvalues of σ_z Pauli operator. As such, local degrees of freedom may vary from $d = 2$ for spins or spinless fermions up to $d = \infty$ for bosons. An arbitrary state can be written as a superposition of the basis elements,

$$|\psi\rangle = \sum_{n_1 \ldots n_N} C_{n_1 \ldots n_N} |n_1 \ldots n_N\rangle\,. \tag{1.1}$$

The state provides a probability amplitude for the outcome of any measurement in the system. The size of the Hilbert space scales as d^N. Therefore, with an increasing size of the system, exponentially increasing resources are required to store or process states with classical computers. However, eigenstates of physical systems are usually much simpler than arbitrary states, because Hamiltonians that govern the dynamics of physical systems, tend to restrict correlations over large distances. This is a consequence of "locality" of interactions in nature.

Over the past few decades, a main area of research of quantum statistical

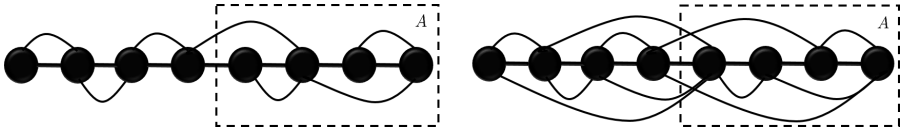


Figure 1.1: Illustrations of 1D chains. Correlations are demonstrated by curves connecting the lattice sites. The entanglement entropies of the reduced density matrix ρ_A are proportional to the curves crossing the boundaries. Area-law states (left) have only a small number of curves crossing the boundary, which corresponds to correlations of sites close to the boundary. Volume-law states (right) correspond to sites correlated over large distances.

physics is to understand under which circumstances the generic exponential scaling of classical resources of many-body states, can be reduced to a polynomial scaling approximation without a significant loss of information about the state. A considerable effort was made towards a rigorous mathematical classification of quantum states with respect to their complexity. A way to define complexity in quantum physics is through quantum entanglement (section 1.1.2). Numerical schemes discussed in this chapter are polynomially scaling algorithms which capture the physics of slightly entangled systems with very high accuracy.

1.1.2 Quantum Entanglement

By tracing out a part of the degrees of freedom of a physical system a theoretical analysis can reveal important information about the nature of correlations featured between different parts of the system. This is achieved by investigating the reduced density matrix of the system [5] [1]. Fig. 1.1 illustrates an example of a bipartition in a 1D system. The amount of correlations between the two subsystems can be measured from their boundary. For a pure state, (eq. (1.1)) defined over degrees of freedom of $A \cup B$, the reduced density matrix of A is

$$\rho_A = \mathrm{Tr}_B \left|\psi\right\rangle \left\langle\psi\right| . \tag{1.2}$$

[1] In this thesis we only use bipartitions of the Hilbert space in real space.

To quantify the quantum complexity physicists use Rényi entropies [5],

$$S_q(A) = \frac{1}{1-q} \ln \mathrm{Tr}\,(\rho_A^q), \tag{1.3}$$

where S_1 is the celebrated Von-Neumann entanglement entropy,

$$S_1(A) = -\,\mathrm{Tr}\,\rho_A \ln \rho_A. \tag{1.4}$$

Entanglement entropy area-law. The property of the entropy of a subsystem A to scale proportion to its boundary, is referred as area-law,

$$S_q \approx C_q L^{D-1}, \tag{1.5}$$

where D is the dimensionality of the system and C_q a system-dependent constant. Area-law provides a system-independent complexity characterization of quantum states. Thus, in addition to deeper conceptual understanding of quantum statistics, it is a significant tool in the development of efficient, classical computer algorithms for quantum simulations.

Area-law in 1D. In 1D, an area-law simply states that all entropies are bounded by a constant number even in the thermodynamic limit (infinite system). As such, subsystems of any size are only finitely correlated with the rest of the system. Hastings [6] proved that gapped ground states of 1D systems with finite range interactions follow an area-law. Furthermore, it was recently shown by Brandão et al. [7] that exponential clustering of correlations imply an area-law for entanglement entropy, relaxing the gap condition. An area-law entropy scaling is also observed in many body localized systems [8]. In the case of many body localization every eigenstate in the spectrum obeys an area-law, resulting in the breakdown of Eigenstate Thermalization Hypothesis [9]. Ground states of local Hamiltonians with diverging correlation length (critical states) display logarithmic violations of the area-law [1], $S_q \propto \log L$. The universal form of logarithmic corrections is analytically known from conformal field theory (CFT) in 1+1 dimensions [10, 11]. In section 1.2, we describe how the MPS ansatz provides a natural and efficient representation of states that obey an area-law in 1D.

Area-Law beyond 1D. For higher dimensions, few general rigorous results exist. Cho [12] showed that under some general constraints, ground states of gapped spin systems in any dimension obey an area-law. Systems with continuous symmetry breaking in higher dimensions feature an extra logarithmic term due to the Nambu-Goldstone modes [13, 14] e.g., superfluid phase. In section 1.3, optimization algorithms which can reproduce area-law in 2D are described. In chapter 3, the algorithm is applied to strongly interacting bosonic systems with continuous symmetry breaking (Bose-Hubbard model).

Entanglement spectrum. Beyond entropies, Li and Haldane [15] proposed that the low-lying part of the spectrum of the reduced density matrix, known as entanglement spectrum (ES) can be used as a "fingerprint" to identify topological order in exotic quantum phases (beyond Landau paradigm). ES was found to be a probe that can identify the $n = 5/2$ Fractional Quantum Hall (FQH) state. This idea has been applied on various topological systems, including FQH effect [16], topological insulators [17] and valence bond states [18]. Alba et al.[19] showed that in gapped states, the spectrum is dominated by contributions around the boundary of the subsystems. More precisely, important contributions to the spectrum come from expansion terms in which the perturbation is applied an equal number of times to each subsystem. Furthermore, it was recently shown by Serbyn et al. [20], that the ES of MBL systems features a power-law structure as a consequence of a complete set of local integrals of motion. A thorough derivation is given in chapter 2.

1.2 1D: Matrix Product States

In this section we illustrate the MPS ansatz and its most common optimization algorithm, (DMRG)[21]. The MPS ansatz is illustrated by fig. 1.2 and reads,

$$|\psi\rangle = \sum_{n_1 \dots n_N} C_{n_1 \dots n_N} |n_1 \dots n_N\rangle = \sum_{\substack{n_1 \dots n_N \\ \alpha_1 \dots \alpha_N}} A^{[1]n_1}_{\alpha_1} A^{[2]n_2}_{\alpha_1 \alpha_2} \dots A^{[N]n_N}_{\alpha_N} |n_1 \dots n_N\rangle \,. \tag{1.6}$$

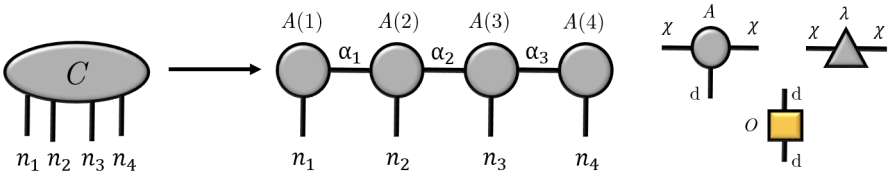


Figure 1.2: *Left*: Mapping the full state to the matrix product representation. *Right*: Often used tensors with the respective dimensions of each bond. MPS element A, Schmidt values λ which form a diagonal matrix and local operator O.

where $A^{[i]}$ are tensors of dimension $\chi^2 d$ on site i, $\alpha_i \epsilon \{1, \dots \chi\}$, $n_i \epsilon \{1, \dots d\}$. χ is usually referred to as virtual dimension and d is the physical dimension of the MPS. The first straightforward difference with respect to the exact representation is the scaling of the number of state elements with respect to the system size. The exact tensor C scales as d^N while the MPS scales as $N\chi^2 d$. The exponential scaling with respect to the system size is equivalent to an exponential scaling of the parameter χ. We shall see that when entanglement entropy follows an area-law, then there exists a size-independent cutoff value for χ, for which the MPS approximation of the full state is numerically exact.

Singular Value Decomposition and MPS. Before continuing with the MPS formalism, it is essential to introduce a decomposition that plays a central role in nearly all optimization algorithms for MPS. This decomposition is Singular Value Decomposition (SVD), namely if M is a m by n matrix whose entries are complex numbers, then there exits a (unique up to a sign) factorization, called a singular value decomposition of M, of the form

$$M = USV^{\dagger}, \tag{1.7}$$

where U is a unitary m by m matrix , S is a real diagonal m by n matrix and V is a unitary n by n matrix. SVD is very effective for low-rank approximations. Eckart–Young theorem [22] states that in order to approximate M by a matrix M' of $\text{rank}(M') < \text{rank}(M)$ in terms of minimizing the Frobenius norm, SVD provides the optimal answer by truncating to the largest $\text{rank}(M')$ elements of S. The truncation error to the Frobenius

norm from a rank k approximation is

$$\|M - M_k\|_F^2 = \sum_{i>k}^{\min(m,n)} \lambda_i^2. \tag{1.8}$$

In terms of a 1D lattice system we can consider a bond in the system, say, i and using eq. (1.7), the elements of eq. (1.1) are expressed as

$$C_{n_1 \ldots n_N} = \sum_{\alpha_i} U_{(n_1 \ldots n_i)\alpha_i} \lambda^{[i]}_{\alpha_i} V^*_{\alpha_i (n_{i+1} \ldots n_N)}, \tag{1.9}$$

where sum extends to $\min(d^i, d^{N-i})$ and N is the size of the chain. The parenthesis denotes vectorization of indices. Left and right orthonormal states are defined as

$$\begin{aligned} |\alpha_i, L_i\rangle &= \sum_{n_1 \ldots n_i} U_{n_1 \ldots n_i \alpha_i} |n_1 \ldots n_i\rangle, \\ |\alpha_i, R_i\rangle &= \sum_{n_{i+1} \ldots n_N} V^*_{\alpha_i n_{i+1} \ldots n_N} |n_{i+1} \ldots n_N\rangle. \end{aligned} \tag{1.10}$$

Using eq. (1.10) the state is written as $|\psi\rangle = \sum_{\alpha_i} \lambda^{[i]}_{\alpha_i} |\alpha_i, L_i\rangle |\alpha_i, R_i\rangle$. The singular values $\lambda^{[i]}_{\alpha_i}$ are the Schmidt values of the state for the bipartition of the system $\{1, \ldots, i\} \cup \{i+1, \ldots, N\}$. The abbreviations "bond i" or "cut i" are often used to identify the position of the boundary between the subsystems. Normalization of the state can be straightforwardly imposed by the constraint

$$\sum_{\alpha_i} \left(\lambda^{[i]}_{\alpha_i}\right)^2 = 1. \tag{1.11}$$

Using eqs. (1.9) and (1.10) the elements of the reduced density matrix $\rho_L = \mathrm{Tr}_R |\psi\rangle \langle\psi|$ are,

$$\begin{aligned} \rho_{n_1 \ldots n_i n'_1 \ldots n'_i} &= \sum_{n_{i+1} \ldots n_N} C_{n_1 \ldots n_i n_{i+1} \ldots n_N} C^*_{n'_1 \ldots n'_i n_{i+1} \ldots n_N} \\ &= \sum_{\substack{n_{i+1} \ldots n_N \\ \alpha_i \alpha'_i}} U_{n_1 \ldots n_i \alpha_i} \lambda^{[i]}_{\alpha_i} V^*_{\alpha_i n_{i+1} \ldots n_N} V_{\alpha'_i n_{i+1} \ldots n_N} \lambda^{[i]}_{\alpha'_i} U^*_{n'_1 \ldots n'_i \alpha'_i} \\ &= \sum_{\alpha_i} U_{n_1 \ldots n_i \alpha_i} \lambda^{[i]2}_{\alpha_i} U^*_{n'_1 \ldots n'_i \alpha_i}, \end{aligned} \tag{1.12}$$

where V is unitary. The last expression is the eigenvalue decomposition of the reduced density matrix, whose eigenvalues are the squared Schmidt coefficients.

Area-Law. It is evident that "small" bipartite entanglement entropy corresponds to a "small" number of significant singular values. In particular, for area-law in 1D, entanglement entropy $S(i) = \sum_{\alpha_i} \lambda_{\alpha_i}^{[i]2} \ln(\lambda_{\alpha_i}^{[i]2})$ is bounded by a constant whose value is dependent on the system. Thus, for a large enough subsystem L, where finite size effects are negligible, the number of singular values (bond dimension χ) required to reproduce the state with exponentially small error is independent of the system size.

Open boundary MPS can now be linked to a successive implementation of SVD on the exact state. Starting from the left edge of the chain,

$$\begin{aligned} C_{n_1 \ldots n_N} &= \sum_{\alpha_1} U_{\alpha_1}^{[1]n_1} \lambda_{\alpha_1}^{[1]} (V_{\alpha_1}^{[2+]n_2 \ldots n_N})^* \\ &= \sum_{\alpha_1 \alpha_2} U_{\alpha_1}^{[1]n_1} \lambda_{\alpha_1}^{[1]} U_{\alpha_1 \alpha_2}^{[2]n_2} \lambda_{\alpha_2}^{[2]} (V_{\alpha_2}^{[3+]n_3 \ldots n_N})^* \\ &\ldots \\ &= \sum_{\alpha_1 \ldots \alpha_N} U_{\alpha_1}^{[1]n_1} \lambda_{\alpha_1}^{[1]} \left(\prod_{1<i<N} U_{\alpha_{i-1}\alpha_i}^{[i]n_i} \lambda_{\alpha_i}^{[i]}\right) (V_{\alpha_{N-1}}^{[N]n_N})^*, \end{aligned} \tag{1.13}$$

Where $\alpha_i \epsilon \{1 \ldots \min(d^i, d^{N-i})\}$. For area-law states a constant bond dimension χ is enough, so $\alpha_i \epsilon \{1 \ldots \min(d^i, d^{N-i}, \chi)\}$. Critical systems, $S \propto \log N$, are also efficiently represented by MPS in finite systems [23], when for each bond of the chain $S \ll \log \chi$. This is in general true if the size of the chain $N \ll \chi$.

Two constraints arise from eq. (1.13). Consider two successive cuts of the chain at bonds $i, i+1$, then

$$|\alpha_{i+1} L_{i+1}\rangle = \sum_{\alpha_i n_i} U_{\alpha_{i+1}\alpha_i}^{[i]n_i} \lambda_{\alpha_i}^{[i]} |n_i\rangle |\alpha_i L_i\rangle$$

From the fact that $|\alpha_i L_i\rangle$ is orthonormal, $\langle \alpha_i L_i | \alpha_i L_i \rangle = 1$, for all bonds, the following two equations, (using left and right sub-lattice) can be concluded,

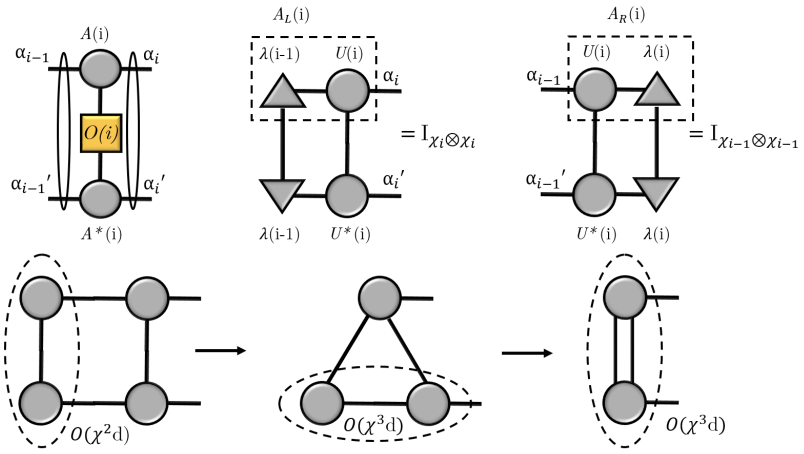


Figure 1.3: Top Left: Transfer Matrix $T_O(i)$; bonds in the same oval region are vectorized. Top Centre/Right: Orthonormal gauge constraint. The dashed boxes show the contraction which converts to left/right orthonormal tensors. Bottom: Efficient contraction steps and the scaling. By repeating this process arbitrary large parts of the chain can be contracted with a constant cost per site.

$$\begin{aligned}\sum_{\alpha_{i-1}n_i} U^{[i]n_i}_{\alpha_{i-1}\alpha_i}\lambda^{[i-1]2}_{\alpha_{i-1}}U^{[i]n_i*}_{\alpha_{i-1}\alpha_i'} &= \delta_{\alpha_i,\alpha_i'},\\ \sum_{\alpha_i n_i} U^{[i]n_i}_{\alpha_{i-1}\alpha_i}\lambda^{[i]2}_{\alpha_i}U^{[i]n_i*}_{\alpha_{i-1}'\alpha_i} &= \delta_{\alpha_{i-1},\alpha_{i-1}'}.\end{aligned} \tag{1.14}$$

The decomposition of the MPS in the form of eq. (1.13) is called canonical decomposition [24]. Singular values can be absorbed to the left or right of each tensor to create right or left orthonormal tensors

$$\begin{aligned}A^{[i+1]}_{L\alpha_i\alpha_{i+1}} &= \lambda^{[i]}_{\alpha_i}U^{[i+1]}_{\alpha_i\alpha_{i+1}}\\ A^{[i+1]}_{R\alpha_i\alpha_{i+1}} &= U^{[i+1]}_{\alpha_i\alpha_{i+1}}\lambda^{[i+1]}_{\alpha_{i+1}}\end{aligned} \tag{1.15}$$

Swapping between left and right gauge can be efficiently performed by a singular value decomposition.

Polynomial contraction scaling. We have shown that the memory required for MPS is exponentially smaller than that required for the full state $\chi^2 dN \ll d^N$. Overlaps of MPS $\langle\psi|\psi\rangle$-which appear in all correlators-can also be calculated efficiently (in polynomial time with respect to the

system size). This is possible by contracting site by site along a direction, as shown in fig. 1.3. This is only a special property of the area-law in 1D. In higher dimensions contractions must be performed in an approximate way as the rank of the tensor increases with respect to the size of the contracted lattice.

Finitely Correlated states. MPS express correlation functions with finite correlation length. In order to illustrate that, we use a connected correlation function

$$C(i, i+r) = \langle O_1(i) O_2(i+r) \rangle - \langle O_1(i) \rangle \langle O_2(i+r) \rangle .$$

To enhance understanding, this calculation can be separated in 3 steps and the assumption of a uniform MPS can be made [25].

1. Contraction of sites 1 to $i-1$. This corresponds to $V_L T_I^{i-2}$ where V_L is the left boundary which is unimportant since the site i lies in an "infinite" distance from the boundary (the projection of V_L to the dominant eigenvector must be non-zero). The application of the transfer matrix (fig. 1.3) $i-2$ times projects the left dominant eigenvector $V_L T_I^{i-2} \approx \langle L_1 | \gamma_1^{i-2}$, where γ_1 is the corresponding eigenvalue. For simplicity it is assumed that there is no degeneracy in the eigenspectrum of the transfer matrix. The same contraction is done from the left part of the chains through sites N to $i+r+1$ which corresponds to $T_I^{N-i-r-2} V_R \approx \gamma_1^{N-i-r-2} |R_1\rangle$.

2. The part of the chain from i to $i+r$ has the form $T_{O_1} T_I^{r-1} T_{O_2}$. We can write $T_I^{r-1} \approx \gamma_1^{r-1} |R_1\rangle \langle L_1| + \gamma_2^{r-1} |R_2\rangle \langle L_2| + \ldots$, where γ_2 is the second largest eigenvalue. For the disconnected part of the correlator this step is trivial.

3. The non-normalized correlator is written as

$$\begin{aligned} \langle O_1(i) O_2(i+r) \rangle \approx \gamma_1^{N-4} \langle L_1 | T_{O_1} | R_1 \rangle \langle L_1 | T_{O_2} | R_1 \rangle \\ + \gamma_1^{N-4-r-1} \gamma_2^{r-1} \langle L_1 | T_{O_1} | R_2 \rangle \langle L_2 | T_{O_2} | R_1 \rangle . \end{aligned} \tag{1.16}$$

   The state is normalized by dividing all terms by γ_1^{N-2}. The first

term of eq. (1.16) is cancelled because it is equal to the disconnected component of the correlator and from the second term we get

$$C(i, i+r) \approx (\frac{\gamma_2}{\gamma_1})^{r-1} \langle L_1| T_{O_1} |R_2\rangle / \gamma_1 \langle L_2| T_{O_2} |R_1\rangle / \gamma_1$$

So, $C(i, i+r) \propto e^{-r/\Lambda}$, where correlation length $\Lambda = -1/\ln(|\gamma_2/\gamma_1|)$.

1.2.1 Matrix Product Operators

Operators acting on MPS are known as Matrix Product Operators (MPO) [26, 27] and their general form is

$$O = \mathrm{Tr}\{\prod_i F^{[i]j_i j_i'}_{a_{i-1}a_i} |n_i\rangle \langle n_i'|\}, \tag{1.17}$$

where the boundary elements are ignored and the trace sums over all indices. The bond dimension of an MPO is called MPO dimension. An MPO is actually an MPS of squared local Hilbert space dimension, $\otimes^N \mathscr{H}_i^{2d}$. In most cases, the operators are represented using a non-truncated MPO. The most common MPOs used are Hamiltonians in variational algorithms. If the MPO is truncated it will act as an additional error source to the algorithm. This is in contrast to MPS, where a cutoff to the bond dimension is used. In this thesis we will use exact representation of MPO.

NN Two-Body interactions. NN coupled systems are the most common, e.g. Hubbard, Ising, Heisenberg, Bose-Hubbard models. Hamiltonian operators of these systems can be efficiently represented by a MPO[2]. For example, open boundary Ising model $H = J\sum_i \sigma_z^{[i]}\sigma_z^{[i+1]} + h\sum_i \sigma_x^{[i]}$, can be mapped to the following multiplication of local operators

$$\begin{pmatrix} h\sigma_x^{[1]} & J\sigma_z^{[1]} & I^{[1]} \end{pmatrix} \begin{pmatrix} I^{[2]} & 0 & 0 \\ \sigma_z^{[2]} & 0 & 0 \\ h\sigma_x^{[2]} & J\sigma_z^{[2]} & I^{[2]} \end{pmatrix} \begin{pmatrix} I^{[3]} & 0 & 0 \\ \sigma_z^{[3]} & 0 & 0 \\ h\sigma_x^{[3]} & J\sigma_z^{[3]} & I^{[3]} \end{pmatrix} \cdots \begin{pmatrix} I^{[N]} \\ \sigma_z^{[N]} \\ h\sigma_x^{[N]} \end{pmatrix} \tag{1.18}$$

[2]Efficiency in this case corresponds to the length of the chain being independent of the MPO dimension.

where σ's are Pauli matrices. For every extra pair of different NN interactions we add, the MPO dimension is increased by 1. Local operators do not increase the MPO dimension. For example, XXZ model is mapped to 5×5 matrices.

Long-Range Two-Body interactions. For generic two-body interactions there are two cases. First, exponentially decaying interactions are mapped efficiently to MPOs. For any other functional form the MPO dimension scales linearly with respect to the system size. In order to reduce computational time, MPO compression schemes can be employed [27]. For general many-body interactions the MPO scales exponentially. It is in general convenient to understand the scaling of MPO dimension as a complexity measure for the operator, similarly to the bond dimension in MPS. In many cases finite automata theory can be used to find exact compressed representations of MPO [28].

1.2.2 Density Matrix Renormalization Group

The major properties of MPS, as well as, the formalism of the generic operators (MPOs) that act on MPS, are illustrated in the previous section. In short, quantum states that obey an area-law, can be efficiently approximated by MPS of constant bond dimension. Although, states are stored efficiently in MPS, it is not obvious whether eigenstates of MPOs can be targeted efficiently. In this section, the most common algorithm for MPS optimization, namely DMRG is illustrated.

DMRG was developed by Steve R. White [21] in 1992. It was proposed as an improved Wilson NRG [29]. In the original formulation DMRG is described as a method that improves Numerical-Renormalization-Group (NRG) scheme. The conceptual interpretation of MPS, as the ansatz of states used in DMRG, was made much later by McCulloch [30].

The original DMRG algorithm was developed to target the ground states of closed quantum systems. The cost function for DMRG optimization is

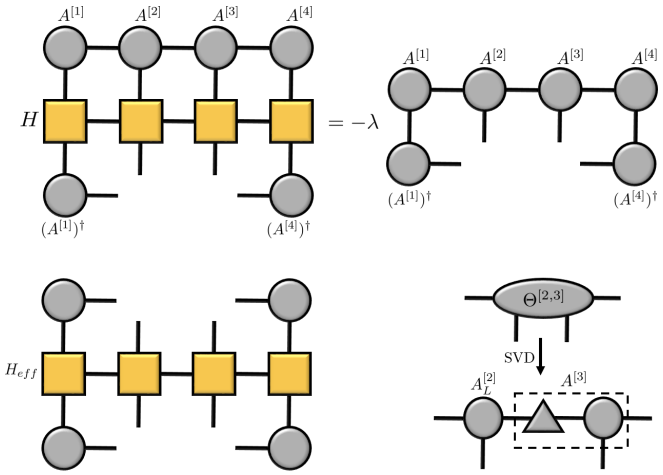


Figure 1.4: *Top*: Graphical form of eq. (1.21). *Bottom left*: Graphical representation of tensor H_{eff}. The $d^2\chi^2 \times d^2\chi^2$ matrix is formed by vectorizing the top and bottom bonds. *Bottom right*: SVD of the tensor Θ. Absorbing the weight to the right tensor fixes the gauge for the next (left-to-right) two-site optimization step.

the energy of the system:

$$E = \frac{\langle\psi| H |\psi\rangle}{\langle\psi|\psi\rangle}, \tag{1.19}$$

where H can be any hermitian operator. The quadratic function minimization, implies a vanishing gradient at the minimum,

$$\partial_{\langle\psi^\dagger|}(\langle\psi| H |\psi\rangle - \lambda\langle\psi|\psi\rangle) = 0, \tag{1.20}$$

where a Lagrange multiplier λ is used. In order to take advantage of the local tensors in MPS representation (eq. (1.6)), DMRG proposes a successive application of a local variation scheme:

$$\begin{aligned} \partial_{A^{[i]\dagger}}(\langle\psi| H |\psi\rangle - \lambda\langle\psi|\psi\rangle) = 0 \;\Rightarrow \\ H_{eff}A^{[i]} - \lambda N_{eff}A^{[i]} = 0. \end{aligned} \tag{1.21}$$

The effective Hamiltonian H_{eff} and the normalization tensor N_{eff} are the operators upon contraction with the rest of the MPS, (fig. 1.4). They contain environment effects from the rest of the chain. The problem as

defined in eq. (1.21) is a generalized eigenvalue problem $Ax = \lambda Bx$. The gauge of the MPS is used to set matrix B to identity,

$$\begin{aligned} A^{[j]} &= A_L^{[j]},\ j < i \\ A^{[j]} &= A_R^{[j]},\ j > i \end{aligned} \tag{1.22}$$

then $N_{eff} = \langle \alpha_{i-1} L_{i-1} | \langle \alpha_i R_i | \, | \alpha_{i-1} L_{i-1} \rangle \, | \alpha_i R_i \rangle$ is an identity operator and the generalized eigenvalue problem reduces to a standard eigenvalue problem. The gauge defined by eq. (1.22) is usually referred to as mixed gauge.

The solution of the eigensystem can be performed using exact diagonalization, which has an asymptotic complexity $O((\chi^2 d)^3)$. Since the target is the ground state (or the low-lying spectrum), it is more efficient to use a Power method (eq. (B.1)) or Lanczos method [31] to reduce the cost to $O((\chi^2 d)^2)$. In optimized DMRG algorithms the matrix H_{eff} is never formed. The matrix-vector multiplication is done in two steps (see fig. 1.5) with asymptotic complexity $O(\chi^3)$.

Convergence of the state to the exact eigenstate can be measured from the energy variance:

$$\langle \psi | \, H^2 \, | \psi \rangle - \langle \psi | \, H \, | \psi \rangle^2 , \tag{1.23}$$

which is 0 for an exact eigenstate. Energy variance is using the full Hamiltonian, so it provides a very accurate error measurement.

One-site DMRG features a property that may result in problems on the optimization. The MPS dimension χ doesn't increase naturally with every optimization step meaning that the Hilbert space doesn't naturally expand. This results in an artificial constraint of simple one-site DMRG methods. There is a number of ways to fix that problem [32, 33], in the one-site optimization algorithm by adding noise in the reduced density matrix. Instead, it is usually preferred to use two-site DMRG [34] which optimizes pairs of NN tensors,

$$\Theta^{[i,i+1]}_{\alpha_{i-1}\alpha_{i+1}} = \sum_{\alpha_i} A^{[i]}_{\alpha_{i-1}\alpha_i} A^{[i+1]}_{\alpha_i \alpha_{i+1}} . \tag{1.24}$$

After diagonalization a SVD is used on Θ to get the new local tensors. The

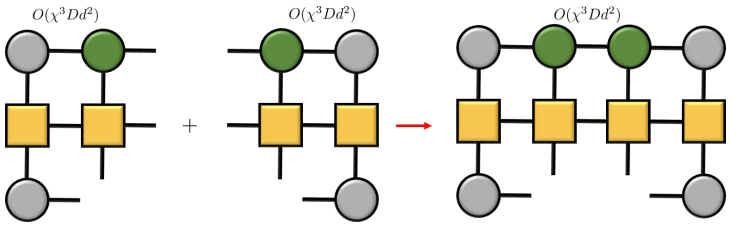


Figure 1.5: *Top*: Application of the two-site effective Hamiltonian to the local tensors in two steps. In the first step, the left and the right part of the effective Hamiltonian contract to the local tensors. In the second step, the left and right part are contracted. Each step has an asymptotic complexity, $O(\chi^3)$.

dimensionality of Θ is $d\chi \otimes d\chi$. So, SVD naturally increases the dimension of bond i to $d\chi$. A maximum bond dimension χ_{max} is set and each SVD is truncated accordingly. In practical calculations χ_{max} can range between $O(10^2) - O(10^4)$.

A short description of the two-site DMRG algorithm following [34] is presented below.

1. The state is initialized. Usually, a random MPS or a product state is chosen. Formally, the state must have a finite overlap with the ground state.

2. For each site i, the MPS is transformed to a mixed canonical form around the tensor at site i: $\ldots A_L^{[i-1]} A^{[i]} A_R^{[i+1]} \ldots$. The two-site tensor if formed: $\Theta^{[i,i+1]} = A^{[i]} A_R^{[i+1]}$.

3. An efficient local solver is used to find the ground state of H_{eff} and $\Theta^{[i,i+1]}$ is updated.

4. $\Theta^{[i,i+1]}$ is decomposed using SVD and the bond is truncated to the desired dimension. The MPS is transformed, by absorbing the singular values appropriately to satisfy eq. (1.22) for the next iteration and step 2 is initialized for $i+1$.

5. Once the right edge of the chain is reached a left-to-right sweep is finished. The algorithm works by alternating left to right and right to left sweeps until the state converges to the ground state with the desired precision (precision is measured by energy variance).

1.2.3 Abelian symmetries

Quantum systems have symmetries which are explicitly conserved to accelerate the simulations [35, 36]. For example, in a closed system of particles the particle number is expected to be constant $N_{total} = \sum_i n_i$. The Hamiltonian of the system commutes with the particle number operator $[H, N_{total}] = 0$. The conserved operator is a sum of local operators and consequently makes the symmetry abelian.

More precisely, particle conservation (or magnetization conservation in spin language) corresponds to a $U(1)$ symmetry group, which consists of all complex numbers with unit absolute value (obviously numbers commute with each other). The generators are $U(\phi) = e^{i\phi N} = \prod_j e^{i\phi n_j}$. Abelian symmetries are applied to MPS in a straightforward way using charge calculus. Local irreducible tensors are created by adding a quantum number (charge) to physical and virtual bonds. On each tensor $A^{[i]n_i}_{\alpha_{i-1}\alpha_i}$, quantum numbers $q(n_i), q(\alpha_{i-1}), q(\alpha_i)$ are added. Each local tensor is irreducible if

$$q(\alpha_{i-1}) + q(n_i) = q(\alpha_i). \tag{1.25}$$

On the last tensor a bias term is added to specify the global sector $q(\alpha_{N-1}) + q(n_L) = q(N_{total})$. So, particle conservation implies $\sum_i q(n_i) = q(N_{total})$. Every bond is identified by a quantum number and a degeneracy vector $\{q(\alpha_{i-1}), \alpha^q_{i-1}\}$. The total bond dimension χ is given by the sum of the degeneracy vectors of all quantum numbers. Quantum numbers are used in MPOs, in a similar fashion to MPS.

Tensor Contraction. Let's assume tensors $A^{[i]}, A^{[i+1]}$ need to be contracted. From eq. (1.25), $q(\alpha_{i-1}) + q(n_i) + q(n_{i+1}) = q(\alpha_{i+1})$. Then, the contraction can be decomposed as:

$$\sum_{q(\alpha_i)} \sum_{\alpha^q_i} A^{[i]q(n_i)}_{[q(\alpha_{i-1})\alpha^q_{i-1}][q(\alpha_i)\alpha^q_i]} A^{[i+1]q(n_{i+1})}_{[q(\alpha_{i1})\alpha^q_{i1}][q(\alpha_{i+1})\alpha^q_{i+1}]} \delta_{q(\alpha_{i-1})+q(n_i)+q(n_i),q(\alpha_{i+1})}. \tag{1.26}$$

where the sum over $q(\alpha_i)$ can be performed in parallel. Since the dimensionality of each degeneracy vector is usually much smaller than the bond dimension χ, the symmetry provides a significant boost to the tensor con-

tractions.

Singular value decomposition. Symmetries can also be exploited in the singular value decomposition. For example, an SVD of a two site tensor $\Theta^{[i,i+1]}$ corresponds to

$$\Theta^{[i,i+1]q(n_i)q(n_{i+1})}_{q(\alpha_{i-1})q(\alpha_{i+1})} = \sum_{q(\alpha_i)} U^{q(n_i)}_{q(\alpha_{i-1})q(\alpha_i)} \lambda^{q(\alpha_i)} V^{q(n_{i+1})}_{q(\alpha_i)q(\alpha_{i+1})} \\ \delta_{q(\alpha_{i-1})+q(n_i),q(\alpha_i)} \delta_{q(\alpha_{i+1})-q(n_{i+1}),q(\alpha_i)} \tag{1.27}$$

where the degeneracy vectors are not written for simplicity. The SVD can be performed for each quantum number $q(\alpha_i)$ separately. The truncation on the SVD is performed as in DMRG algorithm. It is important to group the singular values of all irreducible representations and then truncate to ensure that the bond truncation is globally optimal.

1.2.4 Current State of MPS

In the previous sections, the basic properties of MPS were illustrated. In this section, an overview of the current state of the field is given.

Time evolution. A main topic of MPS algorithms is real time evolution of states. Although it may sound counter-intuitive, quantum evolution is a simpler problem than eigenstate optimization. It can be understood by the entanglement properties of highly excited eigenstates. Excited states of most systems obey volume-law and are approximately random vectors in the corresponding Hilbert space [37]. To access such regime eigenstate optimization is futile as volume law states cannot be described by MPS. However, global quenches from random product states (which are superpositions of many eigenstates) are used to explore a broad part of the spectrum in a dynamical way. The allowed evolution time is dictated by the rate the system builds up correlations, i.e., gets entangled. The maximum time for real time evolution is reached when the bond dimension of the MPS is not sufficient to describe the correlations. For finite size interactions, Lieb-Robinson bounds [38] set a bound to the rate of entanglement entropy increase, $S \leq ct$. So, systems far from equilibrium can be investigated with

MPS techniques for a short amount of time, $t_{max} \propto \ln \chi_{max}$.

Evolution of MPS was first achieved by Vidal [39] for NN Hamiltonians and is known as Time-Evolving-Block-Decimation (TEBD). Vidal used NN unitary gates to perform the evolution, so his method is useful, only for systems with finite range interactions. Later a tDMRG algorithm was introduced by White et al. [40], capable of evolving any Hamiltonian which has an MPO representation. More recently, through better understanding of the MPS manifold Haegeman et al. [41, 42] solved the Time-Dependent-Variational-Principle (TDVP) with MPS.

Excited states. Significant progress has also been made in extensions of static MPS algorithms in order to target eigenstates beyond the ground state energy. In terms of calculating the low lying excitation spectrum, various approaches have been proposed. Using the tangent MPS manifold Haegeman et al. proposed algorithms that could target eigenstates of one and two particle excitations [43, 44], thus providing non-perturbative dispersion relations, spectral weights and scattering matrices. Nakatani et al. applied Tamm-Dancoff and Random Phase Approximation on MPS and used them to calculate the excitations of simple molecules [45]. A deeper connection between the eigenvalues of local transfer matrix of the ground state in uniform systems and the low-lying excitations was made in [46]. The authors used the imaginary and real part of the eigenvalues to reconstruct the dispersion relations for various commonly used Hamiltonians.

As aforementioned the full spectrum of many body localized systems obey an area-law. This implies that every eigenstate is a matrix product state [47]. Various optimization algorithms for arbitrary excited states have been proposed. Most accurate up-to-date methods are Shift-Invert Hamiltonian optimizations [48, 20]. Other approaches include minimization of the distance to the closest product state [49], and systematic Hilbert space expansion [50].

Another aspect of matrix product states is their application to continuous systems (cMPS) as proposed by Verstraete and Cirac [51, 52]. cMPS calculus is slightly more complicated than the MPS, however, generalizations of static and dynamical algorithms, that work for MPS, are possible.

1.3 Beyond 1D

In the previous section we described how MPS are efficient representations of states that obey an area-law. 1D is very special as area-law is trivial, e.g. $S =$ constant. A generalization of MPS to higher dimensions, is computationally challenging. In general, quasi 1D systems can be efficiently encoded in MPS provided that the second dimension is small [53].

To approach higher dimensions naturally, we consider a tensor network where the virtual bonds connect nearest neighbors (NN) in the lattice. The tensor network has the underlying lattice geometry. This ansatz is known as Projected-Entangled-Pair-States (PEPS) [2] and captures entanglement entropy area-law of the underlying lattice. In direct analogy to MPS, the wave-function of the PEPS ansatz is a product of local tensors $A^{[i]n_i}_{\alpha_i\beta i\ldots}$:

$$|\psi\rangle = \mathrm{Tr}\prod_{i\in lattice} A^{[i]n_i}_{\alpha_i\beta_i\gamma_i\ldots}\,|n_i\rangle\,, \tag{1.28}$$

where the number of the bonds of each tensor reflects the connectivity of the underlying lattice.

Area-Law for PEPS. In 2D it is not practical to use a bipartition of the system to show how eq. (1.28) corresponds to entropy area-law. Instead a simply connected patch of the lattice is used as a subsystem, to measure how entropy increases with respect to the volume of the patch. For simplicity a square lattice is used to observe how the rank of the reduced density matrix increases as we increase the volume of the patch. Consider the general environment of a simply connected square patch A of dimensions $L_A \times L_A$. The state elements of the environment are written as

$$\begin{aligned} C^{[Env]} &= \mathrm{Tr}\prod_{i\in Env} A^{[i]n_i}_{\alpha_i\beta_i\gamma_i\delta_i} = C^{[Env]n_{Env}}_{\alpha^1_\partial\ldots\alpha^{L_A}_\partial\beta^1_\partial\ldots\beta^{L_A}_\partial\gamma^1_\partial\ldots\gamma^{L_A}_\partial\delta^1_\partial\ldots\delta^{L_A}_\partial} = \\ &= C^{[Env]n_{Env}}_{s_\partial}, \end{aligned} \tag{1.29}$$

where trace contracts over the internal virtual bonds. n_{Env} is used to indicate all site indices of the environment. Similarly, s_∂ is used to indicate all

virtual indices across the boundary of the patch A. The number of virtual bonds is proportional to the boundary of the patch. The dimensionality of s_∂ is χ^{2L_A}, where χ is the bond dimension. Doing the same contraction for patch A, the full wave-function elements can be written as

$$C_{n_{Env}n_A} = \sum_{s_\partial=1}^{\chi^{2L_A}} C_{s_\partial}^{[Env]n_{Env}} C_{s_\partial}^{[A]n_A}. \tag{1.30}$$

Using the definition of the reduced density matrix (eq. (1.2)), it is straightforward to observe that its rank is $\leq \chi^{2L_A}$. Eq. 1.30 is exact when $\chi^{2L_A} = d^{L_A^2}$, where d is the local Hilbert space dimension. The bond dimension scales as $\chi = d^{L_A/2}$. As with MPS, a constant bond dimension is used for the network, which is enough for states that obey area-law $S_A \leq \ln(\chi^{2L_A}) = 2L_A \ln \chi$. Using the same approach it can be shown that whenever the tensor network has the real space lattice geometry, an area-law always comes out naturally for a constant bond dimension[3] .

A difference from MPS is directly observed. Since every local tensor has more than 2 virtual bonds, the result of a contraction between two NN tensors consists of a tensor of higher rank. This can not be avoided, as it is a direct outcome of a non-trivial entanglement entropy area-law. Rank increase corresponds to an exponential increase in memory and computational time as large regions of space are contracted. Various solutions to the problem have been proposed including the projections of PEPS to a boundary MPS [55], Corner-Transfer-Matrix-Renormalization-Group [56] or lattice renormalization [4]. Tensor Renormalization Group (TRG), initially developed by Levin et al.[4] for classical systems and incorporated by Xiang et al [57] to quantum systems is used in this thesis (section 1.3.2).

Infinite bosonic systems (section 3.2) in a Honeycomb lattice, where the unit cell contains at most two-sites (NN interactions) are studied in the thesis. Since the lattice is translation-invariant an infinite-PEPS wave

[3]Ge and Eisert have recently [54] shown that PEPS can efficiently represent only an exponentially small part of the Hilbert space that spans area-law states which includes gapped ground states of local Hamiltonians.

function is used:

$$|\psi\rangle = \mathrm{Tr} \prod_{i \in \mathscr{W}, j \in \mathscr{B}} A^{n_i}_{\alpha_i \beta_i \gamma_i} B^{n_j}_{\alpha_j \beta_j \gamma_j} |n_i n_j, \rangle \tag{1.31}$$

where i/j, index the white/black translation-invariant sub-lattice, the trace sums over all bonds and site indices. It is convenient to separate the algorithm in two parts. An optimization scheme for the quantum state and a renormalization scheme, which is important for the calculation of correlation functions.

1.3.1 State Optimization: Simple Update

The simple update scheme (SU) is the most computationally efficient way to optimize a (i)PEPS, however, it is not a quasi-exact method, as it avoids an accurate environment computation. The construction of SU method is based on Vidal's TEBD algorithm [39] and its infinite variant in 2007 [3], applied to $D > 1$ systems. The basic requirement for the method to work is a state in canonical form. For MPS it was illustrated that a canonical gauge is always possible (eq. (1.13)). The reason is that there is only one direction to decompose tensors in 1D. In higher dimensions this is not true, however, in practice, the numerical error for assuming a canonical gauge is very small. The algorithm is self-consistent and the partial separability of the state is not affecting considerably the precision of results[4]. The method is presented for the honeycomb lattice but generalization to any lattice geometry is trivial.

Using the canonical form of the state we can write it as:

$$|\psi\rangle_{can} = \mathrm{Tr} \prod_{i \in \mathscr{W}, j \in \mathscr{B}} \lambda_{\alpha_i} \lambda_{\beta_i} \lambda_{\gamma_i} \Gamma^{n_i}_{\alpha_i \beta_i \gamma_i} \tilde{\Gamma}^{n_j}_{\alpha_j \beta_j \gamma_j} |n_i n_j\rangle \,, \tag{1.32}$$

[4]For example, in [56] an extensive comparison between SU and CTMRG optimization is made. Even for very small bond dimension, the difference in accuracy is small and it is more sensitive to the bond dimension itself compared to the method.

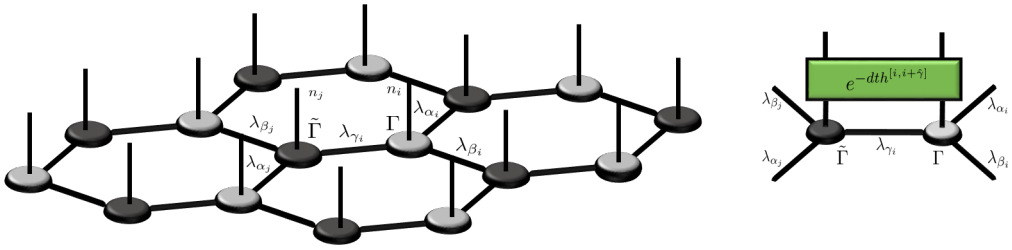


Figure 1.6: *Left:* iPEPS wavefunction in canonical form. The tensors $\tilde{\Gamma}/\Gamma$ occupy the black/white sublattice sites. λs "live" on the bonds of the network. *Right:* Application of the two-site optimization gate.

where λ's represent the singular values along each bond. The equation

$$\begin{aligned} A^{n_i}_{\alpha_i\beta_i\gamma_i} &= \sqrt{\lambda_{\alpha_i}}\sqrt{\lambda_{\beta_i}}\sqrt{\lambda_{\gamma_i}}\Gamma^{n_i}_{\alpha_i\beta_i\gamma_i} \\ B^{n_j}_{\alpha_j\beta_j\gamma_j} &= \sqrt{\lambda_{\alpha_j}}\sqrt{\lambda_{\beta_j}}\sqrt{\lambda_{\gamma_j}}\tilde{\Gamma}^{n_j}_{\alpha_j\beta_j\gamma_j} \end{aligned} \tag{1.33}$$

maps eq. (1.32) form to eq. (1.31). The canonical constraint

$$\sum_{\alpha_i\beta_i n_i} \lambda^2_{\alpha_i}\lambda^2_{\beta_i}\Gamma^{n_i}_{\alpha_i\beta_i\gamma_i}(\Gamma^{n_i}_{\alpha_i\beta_i\gamma_i'})^* \approx \delta_{\gamma_i\gamma_i'}, \tag{1.34}$$

holds for all three permutations of bond indices and for both tensors. The approximate equality of this constraint reflects the fact that an exact canonical gauge for two or more dimensional systems doesn't exist. In numerics we have observed that this constraint is practically exact.

The next steps are a simple generalization of iTEBD algorithm to a 2D system [3]. Using imaginary time evolution the ground state is projected from any quantum state, if the two states have a finite overlap.

$$|\psi\rangle_{GS} = \lim_{t\to\infty} \frac{e^{-tH}}{\|e^{-tH}\,|\psi\rangle\,\|}\,|\psi\rangle\,. \tag{1.35}$$

In honeycomb lattice a NN Hamiltonian is decomposed as,

$$H = \sum_{i\in\mathscr{W}} h^{[i,i+\hat{\alpha}]} + \sum_{i\in\mathscr{W}} h^{[i,i+\hat{\beta}]} + \sum_{i\in\mathscr{W}} h^{[i,i+\hat{\gamma}]} = H_\alpha + H_\beta + H_\gamma, \tag{1.36}$$

where hats on the indices are used to indicate the direction of the NN of

i[5]. It is obvious that all terms within each of the three terms of the right-hand side of eq. (1.36) commute, i.e. $[h^{[i,i+\hat{\alpha}]}, h^{[j,j+\hat{\alpha}]}] = [h^{[i,i+\hat{\beta}]}, h^{[j,j+\hat{\beta}]}] = [h^{[i,i+\hat{\gamma}]}, h^{[j,j+\hat{\gamma}]}] = 0$. Vidal took advantage of this decomposition to perform a Suzuki-Trotter expansion on the evolution operator:

$$e^{-dtH} \approx e^{-dtH_\alpha} e^{-dtH_\beta} e^{-dtH_\gamma} + O(dt^2). \tag{1.37}$$

This equation physically means that imaginary evolution steps can be applied on the whole lattice in three steps. In each step, the NN gates are applied in the whole network across the corresponding dimension. Using the fact that a translation-invariant lattice is used, it is enough to only evolve tensors in a unit cell. So, given a local tensor Γ at site i, each Suzuki-Trotter step corresponds to evolving the tensor at i with each of the NN tensors $\tilde{\Gamma}$. In order to achieve convergence with imaginary time evolution the total evolution time $t_{total} \gg 1/E$, where E is the inverse energy scale of the system.

For example, it will be demonstrated how to apply $e^{-dtH_\gamma} = \prod_{i \in \mathscr{W}} e^{-dt\, h^{[j,j+\hat{\gamma}]}}$.

$$\begin{aligned} e^{-dtH_\gamma} &= \prod_{i \in \mathscr{W}} e^{-dt\, h^{[i,i+\hat{\gamma}]}} \\ &= \prod_{i \in \mathscr{W}} \mathrm{Tr}\left\{ e^{-dt\, h^{[i,i+\hat{\gamma}]}} \left| n'_i, n'_{i+\hat{\gamma}} \right\rangle \left\langle n_i, n_{i+\hat{\gamma}} \right| \right\} \\ &= \prod_{i \in \mathscr{W}} \mathrm{Tr}\left\{ G^{n'_i, n'_{i+\hat{\gamma}}}_{n_i n_{i+\hat{\gamma}}} \left| n'_i, n'_{i+\hat{\gamma}} \right\rangle \left\langle n_i, n_{i+\hat{\gamma}} \right| \right\} \end{aligned} \tag{1.38}$$

In this thesis, a random initial PEPS is chosen. In some cases, it is more useful to start from a product state, and build-up the dimension in the optimization process. For each site $i \in \mathscr{W}$ and $j = i + \hat{\gamma}$, the two-site tensor is formed using eqs. (1.32) and (1.33). In a similar fashion to the 1D

[5]Translation-invariant white and black sub-lattices are defined in order to treat the infinite case. However, in order to apply SU method in non-translation-invariant systems we would still have to create two sub-lattices which would not be translation-invariant.

case:

$$\Theta_{n_i\alpha_i\beta_i n_j\alpha_j\beta_j} = \sqrt{\lambda_{\alpha_i}\lambda_{\beta_i}}\Big(\sum_{\gamma_i}\sqrt{\lambda_{\alpha_i}\lambda_{\beta_i}}\Gamma^{n_i}_{\alpha_i\beta_i\gamma_i}\lambda_{\gamma_i}\tilde{\Gamma}^{n_j}_{\alpha_j\beta_j\gamma_i}\sqrt{\lambda_{\alpha_j}\lambda_{\beta_j}}\Big)\sqrt{\lambda_{\alpha_j}\lambda_{\beta_j}}, \tag{1.39}$$

where the free bonds have been multiplied by λ instead of $\sqrt{\lambda}$. The extra $\sqrt{\lambda}$ act as a mean-field renormalization effect from the environment. The two-site gate G (eq. (1.38)) is then applied,

$$\Theta'_{(n'_i\alpha_i\beta_i)(n'_j\alpha_j\beta_j)} = \sum_{n_i n_j} G^{n'_i,n'_j}_{n_i n_j}\Theta_{n_i\alpha_i\beta_i n_j\alpha_j\beta_j}, \tag{1.40}$$

where the parenthesis is used to show which indices are vectorized. Vectorization is needed in order to consider the tensor Θ as a matrix for the SVD. It is important to observe that lattice connectivity dictates the size of Θ. The matrix dimensions are $d\chi \times d\chi$ in 1D, $d\chi^2 \times d\chi^2$ in honeycomb lattice (fig. 1.6), $d\chi^3 \times d\chi^3$ in square lattice, etc. .

The next step is to decompose the two-site tensor to single site tensors. To do this, SVD is used,

$$\Theta'_{(n'_i\alpha_i\beta_i)(n'_j\alpha_j\beta_j)} = \sum_{\mu} U_{(n'_i\alpha_i\beta_i)\mu}\lambda'_\mu V^*_{\mu(n'_j\alpha_j\beta_j)}. \tag{1.41}$$

The bond in the direction γ is truncated to a constant dimension, keeping only the largest χ singular values. For a general lattice the amount of truncation scales as $d\chi^{z-1} \to \chi$ where z is the connectivity of the lattice.

In the final step, the λs from the non-contracted bonds are removed to store the state in a canonical form and the λ of the bond that was optimized is replaced by the new set of singular values:

$$\begin{aligned}\Gamma^{n_i}_{\alpha_i\beta_i\gamma_i} &= \lambda^{-1}_{\alpha_i}\lambda^{-1}_{\beta_i}U_{(n_i\alpha_i\beta_i)\gamma_i},\\ \tilde{\Gamma}^{n_j}_{\alpha_j\beta_j\gamma_i} &= V^*_{\gamma_i(n_j\alpha_j\beta_j)}\lambda^{-1}_{\alpha_j}\lambda^{-1}_{\beta_j},\\ \lambda_{\gamma_i} &= \lambda'_{\gamma_i}.\end{aligned} \tag{1.42}$$

A time step on γ direction was illustrated. The same steps are followed

for all directions. The SU algorithm [57] is summarized as:

1. The state is initialized to a random state. The initial state projection to the ground state should be non-zero, although numerical errors artificially produce some overlap even in these rare cases.

2. For each bond direction, eqs. (1.39) to (1.42) are calculated. Higher order Trotter expansions can be made to decrease the time-step error. However, in imaginary time evolution the error is not accumulated, so the first order expansion gives fine results.

3. The previous step is repeated enough times to approximate $t \to \infty$. To optimize the performance, it is better to start with a large time step dt and slowly reduce it, to vanishing Suzuki-Trotter errors. In most cases, this can be achieved within $10^4 - 10^5$ steps.

The numerical cost of SU optimization scheme is dictated by the asymptotic complexity of SVD decomposition being $O((d\chi^{z-1})^3)$. SVD can be approximated using Reduced-Rank-Randomized SVD (RRSVD)[58] (see chapter A). The cost of RRSVD is $\approx O(\chi(d\chi^{z-1})^2)$. RRSVD can be used to approximate the singular value spectrum of a matrix when a severe truncation in the singular value spectrum is made, e.g. $d\chi^{z-1} \to \chi$ and the spectrum decays rapidly. For RRSVD to be efficient, the singular value spectrum must decay as $\lambda_i < \lambda_1 i^{-a}, a > 1$. This decay is satisfied as we mostly observe that singular values decay as power-laws with $a \gg 1$. In 1D the singular value spectrum are the Schmidt coefficients which usually decay faster than a power-law in gapped ground states [19]. In higher dimensions the singular value spectrum doesn't have a simple interpretation, as it is only a measure of tensor to tensor correlations. However, in the systems considered in this thesis we observe that it indeed decays exponentially

In contrast to full update or cluster update methods [59], SU allows for bigger bond dimensions and is less complicated because the simplest possible environment approximation is used. Approximating the environment beyond the mean-field level is the most costly part of the algorithm. In 1D, SU can also be used for real time evolution if the imaginary time is swapped with real time, $t \to it$. In higher dimensions, a real time evolution using

SU update is impossible because the errors of the mean field environment accumulate, rendering the method highly unstable.

1.3.2 State Contraction: Tensor Renormalization Methods

Ground state optimization for a PEPS was illustrated in the previous section. Ultimately we are interested in computing expectation values of operators:

$$\langle O \rangle = \frac{\langle \psi | \, O \, | \psi \rangle}{\langle \psi | \psi \rangle}. \tag{1.43}$$

This equation includes contractions of the state which were not present in the optimization process. An exact contraction is a #P-Hard problem [60] and an approximation scheme is required. TRG is used for the calculations of inner products of states and eventually the expectation values of one and two site operators.

To understand the basis of the problem, let's write the full form of eq. (1.43). The denominator has the form:

$$\langle \psi | \psi \rangle = \mathrm{Tr} \prod_{\substack{i \in \mathscr{W} \\ j \in \mathscr{B}}} \sum_{n_i n_j} A^{n_i}_{\alpha_i \beta_i \gamma_i} (A^{n_i}_{\alpha_i' \beta_i' \gamma_i'})^* B^{n_j}_{\alpha_j \beta_j \gamma_i} (B^{n_j}_{\alpha_j' \beta_j' \gamma_i'})^*, \tag{1.44}$$

where the trace is over all bond indices and tensors A, B are first calculated from eq. (1.33). In TRG physical-index contracted tensors (local transfer matrices) are used[6]. In direct analogy to the 1D transfer matrix, the two-dimensional analogue (although not a transfer matrix) is defined as:

$$T_{\tilde{\alpha}_i \tilde{\beta}_i \tilde{\gamma}_i} = T_{(\alpha_i \alpha_i')(\beta_i \beta_i')(\gamma_i \gamma_i')} = \sum_{n_i} A^{n_i}_{\alpha_i \beta_i \gamma_i} (A^{n_i}_{\alpha_i' \beta_i' \gamma_i'})^*, \tag{1.45}$$

where the bonds lying in the same direction are vectorized. The bond dimension of the local transfer matrices is χ^2. From tensor B the transfer matrix $\tilde{T}$ is constructed. The tensors of the right-hand side of eq. (1.44)

[6] In other contraction approximations, for example using MPS projections [55], physical-index contraction can be performed after the bond contraction process.

are $T_{\tilde{\alpha}_i\tilde{\beta}_i\tilde{\gamma}_i}\tilde{T}_{\tilde{\alpha}_j\tilde{\beta}_j\tilde{\gamma}_i}$. The action of the NN operator

$$O_{i'j'} = \mathrm{Tr}\left\{ O^{n'_{i'},n'_{j'}}_{n_{i'}n_{j'}} \left|n'_{i'}n'_{j'}\right\rangle \left\langle n_{i'}n_{j'}\right| \right\},$$

on the local tensors has the form:

$$\phi_{\tilde{\alpha}_{i'}\tilde{\beta}_{i'}\tilde{\alpha}_{j'}\tilde{\beta}_{j'}} = \sum_{\substack{n_{i'}n_{j'}\\ n'_{i'}n'_{j'}}} \sum_{\tilde{\gamma}_i} O^{n'_{i'},n'_{j'}}_{n_{i'}n_{j'}} A^{n_{i'}}_{\alpha_{i'}\beta_{i'}\gamma_{i'}} (A^{n_{i'}}_{\alpha'_{i'}\beta'_{i'}\gamma'_{i'}})^* B^{n_{j'}}_{\alpha_{j'}\beta_{j'}\gamma_{i'}} (B^{n_{j'}}_{\alpha'_{j'}\beta'_{j'}\gamma'_{i'}})^*, \tag{1.46}$$

where it is assumed that the tensor O acts on direction γ. The numerator of eq. (1.43) is written as

$$\left\langle\psi\right| O_{i'j'} \left|\psi\right\rangle = \phi_{\tilde{\alpha}_{i'}\tilde{\beta}_{i'}\tilde{\alpha}_{j'}\tilde{\beta}_{j'}} \mathrm{Tr} \prod_{\substack{i\in\mathscr{W}\neq i'\\ j\in\mathscr{B}\neq j'}} T_{\tilde{\alpha}_i\tilde{\beta}_i\tilde{\gamma}_i}\tilde{T}_{\tilde{\alpha}_j\tilde{\beta}_j\tilde{\gamma}_i}. \tag{1.47}$$

Tensor Renormalization Group. In order to avoid an exact calculation of eqs. (1.44) and (1.47) TRG is employed to renormalize $\{T, \tilde{T}\}$, thus renormalization in this case is performed in the tensor network and must not be confused with Hamiltonian renormalization techniques. The TRG process is shown geometrically in figs. 1.7 and 1.8. It is an iterative coarse graining process where at each iteration we limit the degrees of freedom to the most important ones. The geometry of the lattice remains the same at every iteration, which allows for a reset of the length-scale of the problem.

More precisely, the tensors $\{T, \tilde{T}\}$ can be connected in 3 different directions α, β, γ. The two-site tensors along every direction are constructed as:

$$\begin{aligned} M^{[\gamma]}_{(\tilde{\beta}_i\tilde{\alpha}_j)(\tilde{\beta}_j\tilde{\alpha}_i)} &= \sum_{\tilde{\gamma}_i} T^{[k]}_{\tilde{\alpha}_i\tilde{\beta}_i\tilde{\gamma}_i} \tilde{T}^{[k]}_{\tilde{\alpha}_j\tilde{\beta}_j\tilde{\gamma}_i}, \\ M^{[\alpha]}_{(\tilde{\gamma}_i\tilde{\beta}_j)(\tilde{\gamma}_j\tilde{\beta}_i)} &= \sum_{\tilde{\alpha}_i} T^{[k]}_{\tilde{\alpha}_i\tilde{\beta}_i\tilde{\gamma}_i} \tilde{T}^{[k]}_{\tilde{\alpha}_i\tilde{\beta}_j\tilde{\gamma}_j}, \\ M^{[\beta]}_{(\tilde{\alpha}_i\tilde{\gamma}_j)(\tilde{\alpha}_j\tilde{\gamma}_i)} &= \sum_{\tilde{\beta}_i} T^{[k]}_{\tilde{\alpha}_i\tilde{\beta}_i\tilde{\gamma}_i} \tilde{T}^{[k]}_{\tilde{\alpha}_j\tilde{\beta}_i\tilde{\gamma}_j}, \end{aligned} \tag{1.48}$$

where the superscripts on M's denote the direction of contraction and the superscripts on T's denote the TRG iteration. The main idea of TRG is that the tensors are decomposed perpendicular to the direction of contraction,

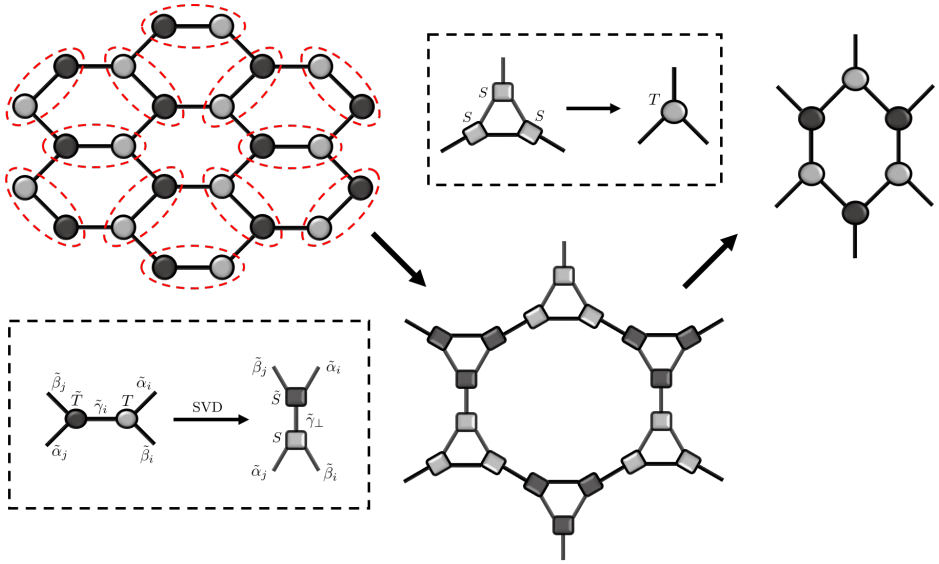


Figure 1.7: *TRG scheme*: NN local transfer matrices are contracted and decomposed along the perpendicular direction. The rewired tensors $\{S, \tilde{S}\}$ are then contracted to form the renormalized lattice. A counter-clockwise rotation by 90° resets the lattice and the length-scale is reset. *Left box*: The geometrical representation of eqs. (1.48) to (1.50). *Top box*: Contraction of the rewired tensors (eq. (1.51)).

as in eq. (1.48). The parenthesis is used to group the indices in order to decompose along the perpendicular direction. The next step is the SVD along the perpendicular direction. For $M^{[\gamma]}$ the decomposition reads:

$$M^{[\gamma]}_{(\tilde{\beta}_i\tilde{\alpha}_j)(\tilde{\beta}_j\tilde{\alpha}_i)} = \sum_{\gamma_\perp=1}^{\chi^4} U^{[\gamma]}_{(\tilde{\beta}_i\tilde{\alpha}_j)\gamma_\perp} \Lambda^{[\gamma]}_{\gamma_\perp} V^{[\gamma]\dagger}_{\gamma_\perp(\tilde{\beta}_j\tilde{\alpha}_i)}. \tag{1.49}$$

The symbol $\perp$ is used to indicate that the new index is along a perpendicular direction to the bond indicated by γ. In order to keep the bond dimension constant the singular values are truncated to the largest χ^2. This is a severe truncation $\chi^4 \to \chi^2$. The singular value spectrum decays fast enough for RRSVD to be used. The decomposition has an asymptotic complexity of $O(\chi^2(\chi^4)^2)$ instead of $O((\chi^4)^3)$.

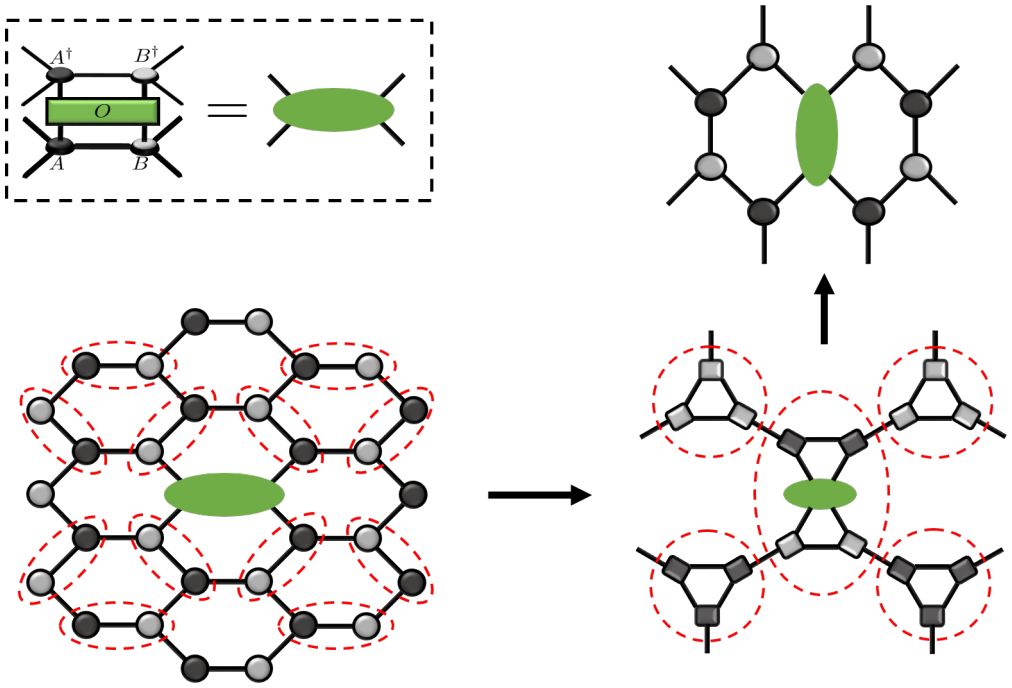


Figure 1.8: Renormalization of the two-body correlation function. *Top-Left*: Graphical form of eq. (1.46). The lattice is renormalized according to TRG. In addition to fig. 1.7, the correlator is also rewired in the bottom-left picture according to the 3rd equation of eq. (1.50).

The rewired tensors are defined as:

$$\begin{aligned} S^{[\gamma]}_{\tilde{\beta}_i\tilde{\alpha}_j\tilde{\gamma}_\perp} &= U^{[\gamma]}_{(\tilde{\beta}_i\tilde{\alpha}_j)\gamma_\perp}\sqrt{\Lambda^{[\gamma]}_{\gamma_\perp}}, \\ \tilde{S}^{[\gamma]}_{\tilde{\beta}_j\tilde{\alpha}_i\tilde{\gamma}_\perp} &= \sqrt{\Lambda^{[\gamma]}_{\gamma_\perp}}V^{[\gamma]\dagger}_{\gamma_\perp(\tilde{\beta}_j\tilde{\alpha}_i)}. \end{aligned} \tag{1.50}$$

The same steps (eqs. (1.49) and (1.50)) are repeated for directions α, β. In the final step the lattice is coarse grained as:

$$\begin{aligned} T^{[k+1]}_{\tilde{\alpha}_\perp\tilde{\beta}_\perp\tilde{\gamma}_\perp} &= \sum_{\tilde{\alpha}\tilde{\beta}\tilde{\gamma}} S^{[\gamma]}_{\tilde{\beta}\tilde{\alpha}\tilde{\gamma}_\perp} S^{[\alpha]}_{\tilde{\gamma}\tilde{\beta}\tilde{\alpha}_\perp} S^{[\beta]}_{\tilde{\alpha}\tilde{\gamma}\tilde{\beta}_\perp}, \\ \tilde{T}^{[k+1]}_{\tilde{\alpha}_\perp\tilde{\beta}_\perp\tilde{\gamma}_\perp} &= \sum_{\tilde{\alpha}\tilde{\beta}\tilde{\gamma}} \tilde{S}^{[\gamma]}_{\tilde{\beta}\tilde{\alpha}\tilde{\gamma}_\perp} \tilde{S}^{[\alpha]}_{\tilde{\gamma}\tilde{\beta}\tilde{\alpha}_\perp} \tilde{S}^{[\beta]}_{\tilde{\alpha}\tilde{\gamma}\tilde{\beta}_\perp}, \\ \phi^{[k+1]}_{\tilde{\alpha}_\perp\tilde{\beta}_\perp\tilde{\alpha}'_\perp\tilde{\beta}'_\perp} &= \sum S^{[\alpha]}_{\tilde{\gamma}'\tilde{\beta}\tilde{\alpha}_\perp} S^{[\beta]}_{\tilde{\alpha}\tilde{\gamma}'\tilde{\beta}_\perp} \tilde{S}^{[\alpha]}_{\tilde{\gamma}''\tilde{\beta}'\tilde{\alpha}'_\perp} \tilde{S}^{[\beta]}_{\tilde{\alpha}'\tilde{\gamma}''\tilde{\beta}'_\perp} \phi^{[k]}_{\tilde{\alpha}\tilde{\beta}\tilde{\alpha}'\tilde{\beta}'}. \end{aligned} \tag{1.51}$$

The position sub-index is dropped for clarity. In the renormalization of the local correlator (eq. (1.46)), the sum is over all indices that do not appear

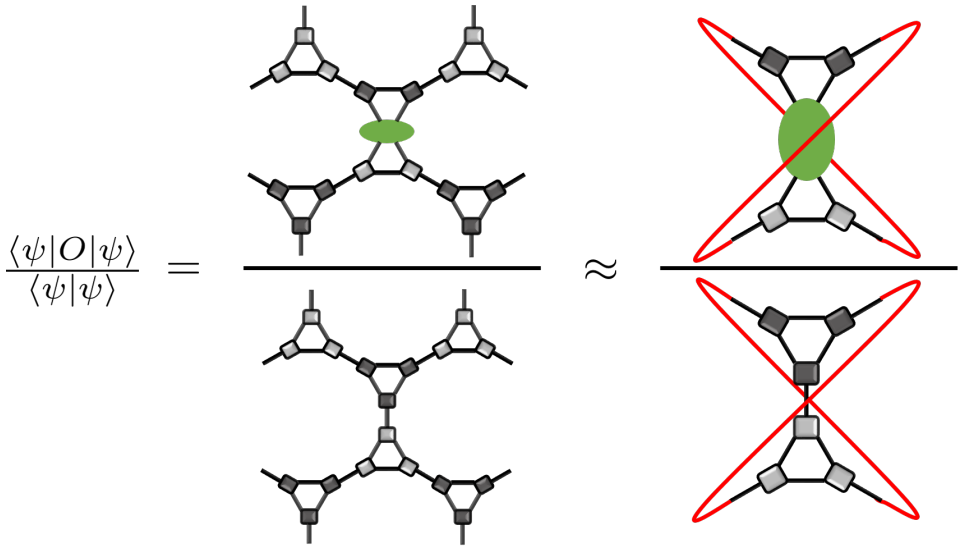


Figure 1.9: Graphical form of eq. (1.52). Given enough TRG iterations, the calculation can be efficiently approximated by imposing periodic boundary conditions on the unit cell.

on the left hand side of the equation. One renormalization iteration consists of equations eqs. (1.48) to (1.51).

The number of sites contracted after N iterations is $2 \cdot 3^N$. It is expected that after a few iterations $(5 - 10)$, the unit cell includes the full renormalization effects of the environment. Therefore it is possible to use periodic boundaries on the unit cell in order to calculate expectation values only from the tensors of eq. (1.51). The correlator of eq. (1.43) is calculated from

$$\frac{\langle\psi|\,O\,|\psi\rangle}{\langle\psi|\psi\rangle} \approx \frac{\sum\limits_{\tilde{\alpha}_\perp\tilde{\beta}_\perp} \phi^{[N]}_{\tilde{\alpha}_\perp\tilde{\beta}_\perp\tilde{\alpha}_\perp\tilde{\beta}_\perp}}{\sum\limits_{\tilde{\alpha}_\perp\tilde{\beta}_\perp\tilde{\gamma}_\perp} T^{[N]}_{\tilde{\alpha}_\perp\tilde{\beta}_\perp\tilde{\gamma}_\perp}\tilde{T}^{[N]}_{\tilde{\alpha}_\perp\tilde{\beta}_\perp\tilde{\gamma}_\perp}}, \tag{1.52}$$

for every two-site operator O. Fig. 1.9 illustrates the graphical form of eq. (1.52).

The bottleneck of TRG scheme is the SVD in eq. (1.49) and the contraction of the last term in eq. (1.51) with asymptotic complexity $O((\chi^4)^3)$. RRSVD reduces the cost of SVD process, however, eq. (1.51) cannot be accelerated further because of containing only tensor-tensor multiplications.

1.3.3 Progress on Tensor Renormalization methods

TRG renormalizes the lattice by minimizing the truncation error of a local tensor M, i.e. eq. (1.49), meaning that TRG is a local optimization method. However, M has an environment which we have ignored but its effect can increase the convergence rate and improve the accuracy of the renormalization algorithm. To this end, eq. (1.44) can be written using M and its environment M^{env},

$$\langle\psi|\psi\rangle = \mathrm{Tr} M M^{env}. \tag{1.53}$$

A global optimization algorithm minimizes the truncation error of MM^{env}. The method that optimizes the lattice taking into account the environment correction is known as Second Renormalization Group (SRG)[61].

Significant progress has been made towards 3D systems. This was possible using a Higher Order SVD (HOSVD) [62]. HOSVD practically truncates many bonds of a tensor "simultaneously", and therefore it is useful in lattices with high connectivity. Xie et al. [63] took advantage of HOSVD to create a High Order Tensor Renormalization Group (HOTRG/HOSRG) and applied it to the 2D quantum and 3D classical Ising model.

Recently, Evenbly and Vidal [64] combined TRG with Multiscale Entanglement Renormalization Ansatz (MERA)[65], to form Tensor-Network-Renormalization (TNR). MERA is an ansatz which efficiently describes quantum states with logarithmic corrections to the entropy area-law in the thermodynamic limit. Using the disentangling gates of MERA in TRG the local tensors are disentangled before each renormalization. This ansatz produces the correct RG flow and an exponential rate of convergence (with respect to the bond dimension) of the free energy error at the critical point of the 2D classical Ising model. Using TRG, the convergence rate at the critical point is polynomial. SRG improves the scaling but it still fails to disentangle the blocks completely.

Chapter 2

Entanglement of arbitrary excited eigenstates in Many Body Localized systems

This chapter is divided in three sections. In the first section the many-body localized (MBL) phase is introduced. We briefly review the history and the state of the field. The local integral of motion (LIOM) formalism is presented in more detail as a generic emergent formalism of MBL systems.

In the second section, a new variational MPS algorithm (eDMRG) that efficiently targets arbitrary excited states of any quantum system, is presented. The only physical constraint of the algorithm is the entanglement of states around the target energy. If the eigenstates around the target are slightly entangled, the optimization works efficiently for arbitrary system sizes. The eDMRG algorithm is validated using MBL systems. A universal property of MBL systems is a characteristic eigenspace, composed of eigenvectors that have exponentially clustering correlations [66]. This implies that *all* eigenstates of MBL systems are efficiently represented by matrix product states. We find that, certain properties of the MBL phase predicted using exact diagonalization (ED), are retained in the thermodynamic limit.

In the third section, the quasilocal integral of motion (QLIOM) formalism is used to identify the structure of the eigenvalues of the reduced

density matrix, i.e. Entanglement Spectrum (ES). The ES features a simple power-law structure. This distinguishes MBL eigenstates from ground states of local gapped models, where ES has a faster than power-law decay [67, 17], while in both cases entanglement entropy obeys an area-law. The phenomenological results are backed up by ED and eDMRG large scale simulations.

2.1 Many-Body localization

One of the main challenges of statistical physics is to understand transport properties of large complicated systems. Anderson formulated a mechanism known as Anderson Localization to describe transport of non-interacting electrons in a disordered system [68]. He argued that, if the disorder is sufficiently strong, the particle becomes localized. This implied a breakdown of quantum ergodicity for a particle in a disordered potential and led to deeper understanding regarding thermalization/equilibration of closed quantum systems.

Although, Anderson Localization was extensively studied in the past four decades [69], interacting systems had not received much attention. This was partially because: 1) experiments of isolated systems of strongly interacting particles [70](trapped ions or cold atoms) have been only recently made possible. 2) interacting systems require the use of the full Hilbert space, which complicates both theory and simulation. In 2006, Basko et al. [71] showed that an interacting electronic system in a disordered potential exhibits a vanishing conductivity at finite temperature for all orders of perturbation theory, verifying previous findings for interacting electrons [72]. This breakthrough was followed by a large amount of numerical research trying to reproduce and generalize the concept to other systems [73, 74, 75, 8, 76]. Lattice systems in 1D have received special attention due to their finite Hilbert space, which is easier to simulate. The main difference between continuous and discrete systems is the existence of a mobility edge in the latter. In particular, continuous systems at high enough temperature/energy density have finite conductivity independently of how strong the disorder is. To this end, continuous systems feature a

phase transition at high enough temperature (mobility edge in the spectrum). On the other hand, discrete systems have bounded spectra and a full spectrum localization is possible for sufficient disorder strength. Experimental evidence of MBL existence was found using cold atoms in [77] for 1D and in [78] for 2D systems.

2.1.1 Local integrals of Motion

MBL systems are non-ergodic. The microscopic mechanism responsible for ergodicity is the eigenstate thermalization hypothesis (ETH) [79]. Non-ergodicity is also a feature of non-disordered (integrable) systems that satisfy Yang-Baxter relations [80]. The Hamiltonians of integrable systems commute $[H, O_a] = 0$ with an extensive set $\{O_a\}$ of mutually commuting $[O_b, O_a] = 0$, non-trivial operators referred to as integrals of motion. Understanding of integrable systems led to the idea that MBL systems must feature a similar set of integrals of motion [81, 82]. In contrast to the case of integrable systems, MBL integrals of motion $\{\tau_a\}$ are localized and the integrability of MBL systems is stable with respect to the addition of perturbative terms to the Hamiltonian. The existence of local integrals of motion (LIOMS) is numerically [83, 84] and analytically [85, 86] verified for various locally disordered 1D systems. In this section, the LIOM picture is illustrated and is further modified to a generic quasi-local (QLIOM) picture.

The formalism is independent of the local Hilbert space dimension. For concreteness a spin-1/2 Fock space is used. The local operator basis is chosen to be the identity plus the Pauli matrices $\{\sigma_0, \sigma_1, \sigma_2, \sigma_3\}$. A generic operator can be written as an expansion in the operator basis

$$O = \sum_{n_1 n_2 \ldots n_L = 0}^{3} C_{n_1 n_2 \ldots n_L} \sigma_{n_1}^{[1]} \sigma_{n_2}^{[2]} \ldots \sigma_{n_L}^{[L]}. \tag{2.1}$$

Operator O is a 2^{2L} dimensional vector.

Quasilocal operators. A quasilocal operator $\tau^{[j,i]}$ is a generic operator, which acts non-trivially on a finite support S_R. In the present context, S_R denotes a spin-1/2 Hilbert space spanned by $j - i + 1 = R$ sites. Matrix

elements of the operator that involve sites outside the support, decay exponentially with respect to the distance of the site from the support boundary. An operator acting on a finite support S_R of a length L system, from sites i to j can be written as

$$O^{[i,j]} = \sum_{n_i \dots n_j = 0}^{3} O^{[i,j]}_{n_i \dots n_j} \sigma_0^{[1]} \dots \sigma_0^{[i-1]} \sigma_{n_i}^{[i]} \dots \sigma_{n_j}^{[j]} \sigma_0^{[j+1]} \dots \sigma_0^{[L]}. \tag{2.2}$$

To have compact sized equations, trivial identity operators will not be written explicitly and the matrix elements of the operator will be denoted by a single 4^{j-i+1} dimensional index Λ. Using these conventions, quasilocal operators are written as an operator expansion around the support

$$\begin{aligned} \tau^{[i,j]} = O^{[i,j]} &+ \sum_{k n_k} \sigma_{n_k}^{[k]} J_{n_k}^{[ijk]} + \sum_{k n_k \Lambda} O'^{[i,j]}_{\Lambda} \sigma_{n_k}^{[k]} J_{n_k \Lambda}^{[ijk]} + \sum_{k n_k l n_l} \sigma_{n_k}^{[k]} \sigma_{n_l}^{[l]} J_{n_k n_l}^{[ijkl]} \\ &+ \sum_{k l n_k n_l \Lambda} O''^{[i,j]}_{\Lambda} \sigma_{n_k}^{[k]} \sigma_{n_l}^{[l]} J_{\Lambda n_k n_l}^{[ijkl]} + \dots \ . \end{aligned} \tag{2.3}$$

Primes in O operators denote that the matrix elements of these operators are not equal. However, all of these operators act non trivially in the same area. In summations, different local operators act on different sites and outside the non-trivial area. For example, in the fourth term, $k \neq l$ and $k > j$ or $k < i$. The couplings J decay exponentially with respect to the maximum distance between operators and the boundary of the support. Quasilocal operators constructed as in eq. (2.3) are a natural choice for localized integrals of motion, as the exponentially suppressed non-local couplings provide exponentially decaying correlations. The simplest quasilocal operator $\tau^{[i]}$ has a local support $O^{[i]}$ spanned by the local spin basis.

Hamiltonian diagonalization. In the many body localized phase such quasilocal operators form integrals of motion. Most MBL phenomena can be explained in the limit where the support of the quasi-local operator is a single site [81, 82] and a complete set of LIOMS $\tau^{[i]}$ exists.

To understand the idea it is easier to use a concrete model; in this case,

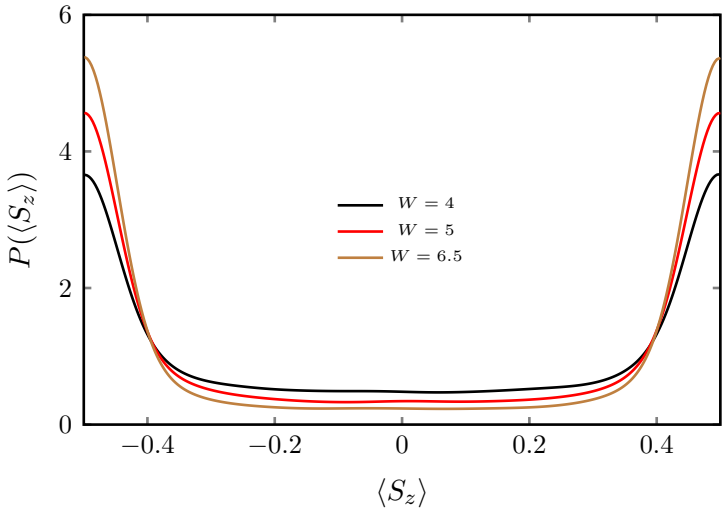


Figure 2.1: Probability distributions of expectation values of S_z operators for an $L = 30$ XXZ chain. The sample is taken over ≈ 1000 disorder realizations and over all sites. Increasing disorder makes the distribution sharper around the two eigenvalues of S_z operator, indicating quasi-product eigenstates which become increasingly factorized as disorder increases.

spin-1/2, site-disordered XXZ chain,

$$H_{XXZ} = \frac{J}{2}\sum_i (\sigma_+^{[i]}\sigma_-^{[i+1]} + \sigma_-^{[i]}\sigma_+^{[i+1]}) + \frac{J_z}{4}\sum_i \sigma_3^{[i]}\sigma_3^{[i+1]} + \frac{1}{2}\sum_i w_i \sigma_3^{[i]}. \quad (2.4)$$

The couplings are set to $J, J_z = 1$ and $\sigma_\pm = 2(\sigma_1 \mp i\sigma_2)$. Disorder is sampled from a uniform distribution $w_i \in [-W, W]$. When disorder is set to zero the model corresponds to Heisenberg Hamiltonian. The site disordered XXZ chain is known to undergo a localization transition for $W \approx 3.7$ [8]. For intermediate disorder $W = 3 - 3.7$, eigenstates are believed to have a multifractal behavior where entanglement entropy of a system bipartition obeys a volume-law but is sub-thermal [50, 87].

In the strongly disordered limit $W >> J, J_z$. In that limit, the typical disorder mismatch between NN sites is much larger than the non-local Hamiltonian terms. Similarly to a step potential, particle hopping is suppressed $\propto e^{-|\Delta w|/O(J,J_z)}$. The Hamiltonian of the model is approximately a diagonal matrix spanned by the $\sigma_3^{[1]} \otimes \ldots \sigma_3^{[L]}$ basis. The product state-like form of the eigenstates is probed by measuring projections of the spins to

the z axis, as shown in fig. 2.1. For high disorder, the distribution has a finite weight around the two eigenvalues of the S_z operator.

Corrections to the product states are exponentially small and phenomenologically understood by the use of LIOMs. In the case of the XXZ Hamiltonian, the LIOMs are just quasilocal rotations of σ_3 operators,

$$\tau_3^{[i]} = U\sigma_3^{[i]}U^\dagger = \sigma_3^{[i]} + \text{ small nonlocal corrections.} \tag{2.5}$$

To the 0th order $\tau_3^{[i]}$ and $\sigma_3^{[i]}$ operators are equal. However, in contrast to the σ_3 operators, LIOMs are exactly conserved. Any eigenstate is a simultaneous eigenstate of all LIOMs. The diagonalized Hamiltonian is spanned by the $\tau_3^{[1]} \otimes \dots \tau_3^{[L]}$ basis,

$$H_{diag} = \sum_i K_0^{[i]}\tau_3^{[i]} + \sum_{ij} K^{[ij]}\tau_3^{[i]}\tau_3^{[j]} + \sum_{ijk} K^{[ijk]}\tau_3^{[i]}\tau_3^{[j]}\tau_3^{[k]} \dots \tag{2.6}$$

where $K^{[jkl]} \propto e^{-a\mathcal{D}_{jkl}}$ decay exponentially in proportion to the maximum distance of the operators, i.e., $\mathcal{D}_{jkl} = \max\{|j-k|, |l-k|, |j-l|\}$. LIOMs do not necessarily commute with the conserved charges of the Hamiltonian. Given a conserved operator C, the commutator $[H, [\tau^{[i]}, C]] = 0$, however $[\tau^{[i]}, C] \neq 0$.

The existence of a complete set of LIOMs fails to capture the physics of systems that:

1. feature a mobility edge. It was shown in [88] that a mobility edge doesn't completely "kill" LIOMs. In the case of a mobility edge, the spectrum has f delocalized states and $M-f$ localized states (M being the size of the spectrum). If the Hamiltonian is first projected to the localized part of the spectrum, the localized part of the system can be described by a set of globally dressed LIOMs, i.e., $[P_{loc}HP_{loc}, \tau^{[i]}] = 0$.

2. contain large rare resonances occurring in areas where disorder is "abnormally" low. The resonant areas are harder to understand phenomenologically due to their ability to thermalize the environment around them. Resonant areas can be addressed when the environ-

ment around the area is large enough to be thermalized, or equivalently, when the resonant areas are very rare. In this case, we propose a quasilocal operator (eq. (2.3)), where the non-trivial support spans the resonant area.

2.2 Variational MPS optimization for arbitrary excited eigenstates: eDMRG algorithm

To efficiently simulate large 1D systems we resort to the MPS ansatz, see section 1.2. The states are approximated accurately, if the bond dimension χ is large enough ($S_{ent} \ll \ln \chi$) to capture the entanglement of the state on every bond of the chain. Assume a quantum system whose spectrum is efficiently represented by an MPS of bond dimension χ. The DMRG algorithm (section 1.2.2) is modified to accurately and efficiently target any part of the spectrum, using a shift-invert method (chapter B). The eDMRG algorithm requires a very small number of modifications on the standard DMRG method and has the same cost with respect to the bond dimension ($O(\chi^3)$).

A direct optimization of the quadratic form $\langle\psi| (H-\lambda)^{-1} |\psi\rangle$, would be ideal, however, it is impossible to implement in MPS formalism. The main problem is that the inverse Hamiltonian is a highly non-local matrix. Thus, the MPO representation of the Hamiltonian has a bond dimension $D \propto 2^{2L}$, rendering the exact Hamiltonian MPO representation impossible.

The eDMRG method is based on the squared, shifted Hamiltonian $\tilde{H}^2 = (H-\lambda)^2$ and does a variational optimization on the quadratic form

$$\langle\psi| \tilde{H}^2 |\psi\rangle . \tag{2.7}$$

In standard DMRG, the ground state is found for each local variational update and local tensors are updated in a sweeping process. In eDMRG, we target any energy and shift-invert the effective local Hamiltonian iteratively (chapter B) by solving the linear system of equations,

$$(\tilde{H}^2)^{[i,i+1]}_{eff} X^{[i,i+1]} = \Theta^{[i,i+1]}, \tag{2.8}$$

where $\Theta^{[i,i+1]}$ is defined in eq. (1.24) and the effective square Hamiltonian

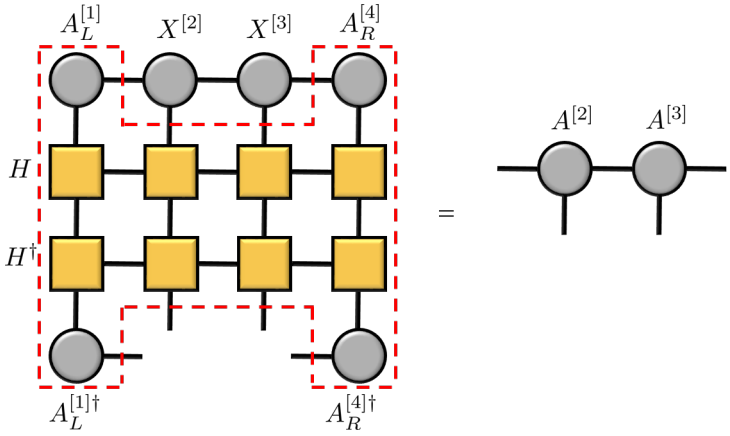


Figure 2.2: Graphical representation of the local update scheme for the eDMRG algorithm. The red boundary denotes $(\tilde{H}^2)^{[2,3]}_{eff}$. As in standard DMRG, the mixed canonical gauge is used for the MPS.

is shown in fig. 2.2. When the linear system is solved, the tensor $X^{[i,i+1]}$ updates $\Theta^{[i,i+1]}$ and the algorithm proceeds to the next local update. After a few sweeps of the chain the algorithm converges to an eigenstate close to the target energy. The quadratic form has to be optimized for the squared Hamiltonian for two reasons: 1) if the Hamiltonian is used, the sweeping process is very unstable and 2) the conjugate gradient algorithm requires a sign-definite operator. Squaring a MPO operator can be achieved site by site with a cost per site $O(d^3D^4)$, where d is the local Hilbert space dimension and D is the bond dimension of the MPO representation of the Hamiltonian. It is thus, a cost efficient calculation in contrast to the squaring of the matrix representation of the Hamiltonian, where the cost is $O((d^L)^4)$. By squaring the Hamiltonian, the convergence rate of the power-method (eq. (B.3)) is also squared providing significant acceleration to the algorithm. The price paid to use the squared MPO operator is a larger MPO dimension. Squaring the operator leads to a MPO of dimension D^2, D being the dimension of the Hamiltonian MPO. Finite automata techniques [28] can be used to store the squared Hamiltonian in a $2D-1$ MPO (if local Hilbert space dimension $d = 2$) [89]. The matrix-vector multiplication is the bottleneck of the shift-invert algorithm and scales as $O(D^2)$. Therefore, reducing the dimension provides a significant speedup to the algorithm. In practice, the acceleration provided by squaring the convergence ratio of the Power method, is cancelled by the application of a MPO with larger bond dimension. The scaling of the algorithm with respect to the bond dimension

of the state is the same as to the ground state DMRG algorithm $O(\chi^3)$, so the MPS used can be of similar size.

The full eDMRG scheme for a left to right sweep is shown below:

1. The shifted square Hamiltonian MPO $\tilde{H}^2$, and the initial MPS $|\psi_0\rangle$ are initialized.

2. For each site i, the MPS is transformed to a mixed canonical form around the tensor at site i: $\ldots A_L^{[i-1]} A^{[i]} A_R^{[i+1]} \ldots$. The two-site tensor is formed, $\Theta^{[i,i+1]} = A^{[i]} A_R^{[i+1]}$.

3. Eq. (2.8) is solved using the conjugate gradient solver, (algorithm 2).

4. The updated tensor $\Theta^{[i,i+1]}$ is decomposed via SVD to get the new local tensors and in the same way as ground state DMRG, the singular values are absorbed by the next tensor. The state now is in mixed gauge form around $i+1$: $\ldots A_L^{[i]} A^{[i+1]} A_R^{[i+2]} \ldots$, ready to optimize the next pair of tensors, $i+1, i+2$ at step 2.

2.2.1 eDMRG validation and error sources

To validate this method a spin-1/2 XXZ site disordered chain is used (eq. (2.4)). Varying disorder while in the MBL phase, changes the average amount of entanglement per eigenstate, thus providing an appropriate model to test the quality of the eDMRG algorithm and further verify the phenomenological and exact diagonalization predictions in the thermodynamic limit. The center of the energy band is approximately at $E \approx 0$. As such the target energy is set to $E = 0$. The model conserves total magnetization $S_z = \sum_i^L s_z^{[i]}$ which corresponds to a $U(1)$ symmetry and is explicitly conserved by eDMRG. We target eigenstates in the $S_z = 0$ sector.

The number of conjugate gradient iterations used is $O(10^2 - 10^3)$. The number of sweeps is $N_{sw} = 50$. In order to achieve better precision it is more efficient to modify conjugate gradient iterations than the number of sweeps. The initial states are chosen as random Fock states in the $S_z = 0$ sector. The truncation error used in the SVD of $\Theta^{[i,i+1]}$ is set to be the machine

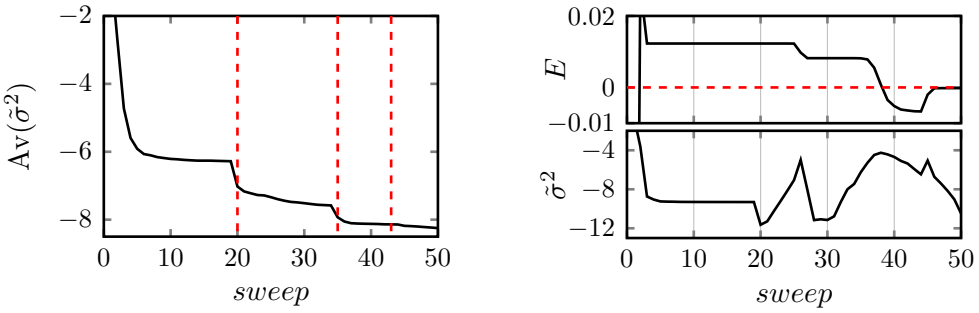


Figure 2.3: *Left*: Mean logarithmic energy variance plot with respect to the DMRG sweeps for $L = 30, W = 4$. The red perpendicular lines show when the maximum bond dimension χ_{max} is increased. The corresponding values are $\{24, 60, 200, 400\}$. *Right*: Convergence of energy and energy variance for a single eigenstate for $L = 30$ chain. The red horizontal line denotes the targeted energy.

precision limit for double precision numbers $\approx 10^{-16}$ in the sense that the error eq. (1.8) is below machine precision. Additionally, a maximum bond dimension χ_{max} is set for all eigenstates. The bond dimension at each bond of each state is hard-bounded by the maximum bond dimension and soft-bounded by the machine precision limit in the singular value decomposition. In addition, the hard-bound of the bond dimension is slowly increased to the final value. This is commonly used in ground state DMRG algorithms to swiftly get a crude initial approximation of the state and slowly increase bond dimension to improve accuracy.

For the eDMRG numerical data, in this chapter, we use samples of $10^3 - 10^4$ eigenstates. Each eigenstate is drawn from a different disorder realisation and a different initial state. The ED data are samples of $O(10^4)$ eigenstates. For chains $L > 16$, a shift-invert algorithm from PETSc/SLEPc package [90] with MUMPS eigensolver is used. For each disorder realization $50 - 100$ eigenstates around $E = 0$ are drawn.

In fig. 2.3 (left), we show the convergence of eDMRG algorithm with respect to the number of sweeps for disorder $W = 4$, in terms of the logarithmic energy variance $\tilde{\sigma}^2 = \log_{10} \sigma^2$, averaged over the sample. The maximum bond dimension allowed is slowly increased to its final value to speed up the algorithm. When χ is increased, a "jump" to lower energy

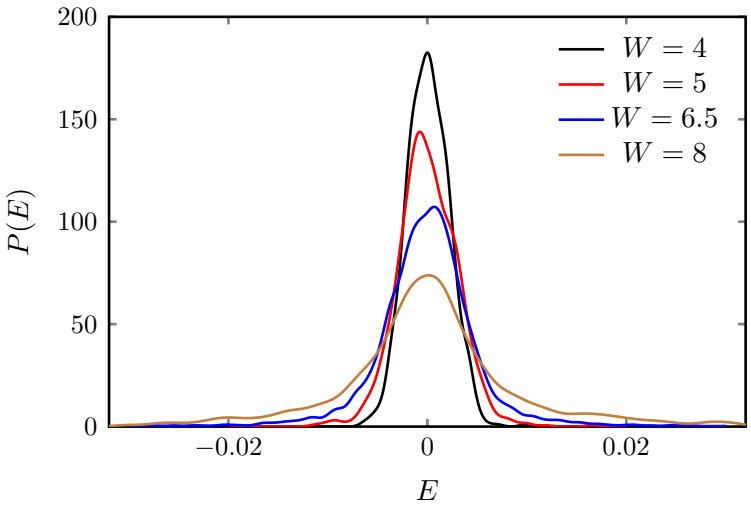


Figure 2.4: Probability distribution function of eigenstate energy for an $L = 30$ chain, for various disorder strengths. The probability distributions are approximatelly Gaussian around the target energy.

variance appears. The right plot of fig. 2.3, shows the convergence of a single eigenstate. From the energy plot it can be seen that the state is often stuck in specific energies. These energies are eigenstates of the Hamiltonian since they have very low energy variance (bottom-right plot). The state tends to converge to eigenstates closer and closer to the target. This behavior is not typical of a ground state DMRG algorithm, in which the ground state quality is steadily improved without "jumps".

Fig. (2.4) illustrates the distribution of energies for samples at various disorder strengths. The distribution of energy is approximately Gaussian around the target energy, indicating no bias with respect to the energy. Interestingly, the width of the distribution becomes larger for larger disorder due to higher eigenstate hybridization for smaller disorder. For high disorder, the eDMRG algorithm gets easily stuck into some eigenstate. The hybridization of eigenstates is very small. As such, the algorithm is less likely to "jump" and converges closer to the target energy. On the other hand, as disorder becomes weaker, "jumping" is easier, and the final eigenstate is closer to the target.

Fig. (2.5) shows the distribution of the logarithmic energy variance for various disorder strengths. The peak of $-\tilde{\sigma}^2 \approx 13$ indicates the machine precision limit. For low disorder the quality of eigenstates becomes

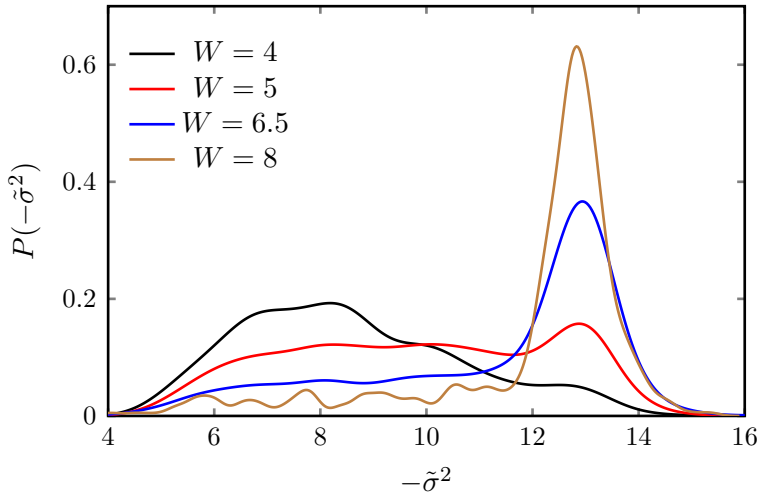


Figure 2.5: Probability distribution function of energy variance for various disorder strengths. The peak at ≈ 13 indicates the double precision limit. The set of states that converge to machine precision vanishes as the system approaches the delocalized limit.

considerably worse and eventually standard deviation σ and energy are approximately equal.

In addition to the eigenstate error, eDMRG algorithm is also susceptible to statistical error. Is eDMRG biased against slightly or highly entangled states? It is expected that since we use MPS of small bond dimension, the selection of the eigenstate could be slightly biased towards lower entropy. In fig. 2.6 we show that this is not the case, at least up to $S < 1.6$. The distributions of entanglement remain unchanged between large and small systems which are directly accessible through ED. This is expected, since correlations from larger distances do not reach the center of the chain. The probability distribution of entropy decays exponentially $P(S) = e^{-aL}$ for $S > \ln 2$, with the inverse localization length a being a monotonically increasing function of disorder strength. For $S < \ln 2$, there is a plateau with a quantized value at $S = \ln 2$. This corresponds to resonant NN sites around the cut $|\psi\rangle_{res} = 1/\sqrt{2}(|01\rangle \pm |10\rangle)$. These entangled pairs appear when the disorder mismatch on the sites around the bipartition is approximately equal to the hopping strength or 0, i.e., $w_i - w_{i+1} = \pm \mathrm{J}$ or 0.

In parallel to the development of the eDMRG algorithm, several other MPS optimization algorithms for arbitrary excited states were published

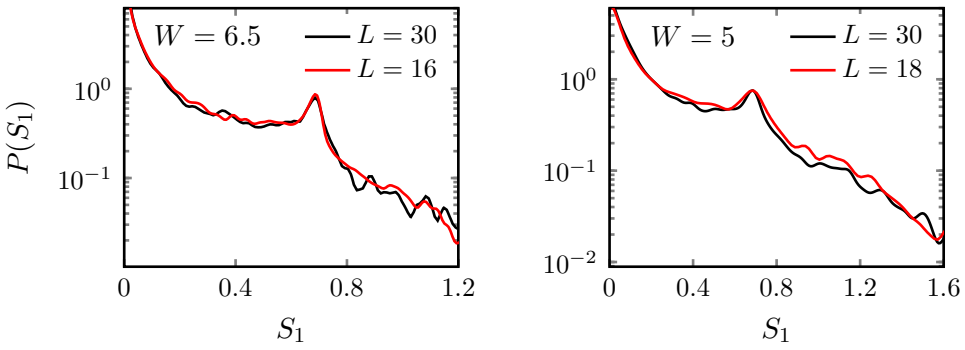


Figure 2.6: *Left*: Probability distribution function of entanglement entropy for different system sizes L=16, 30, for disorder $W = 6.5$. The entropy is taken along a cut in the middle of the chain. eDMRG algorithm was used for $L = 30$ and exact diagonalization was used for $L = 16$. The sample size in both cases is $O(10^4)$. *Right*: The same plots for L=18, 30 and disorder $W = 5$. The fact that distribution remains the same with respect to the system size is an indication of an area-law scaling of entanglement entropy.

[49, 50, 48, 89]. The most interesting approaches are briefly reviewed and compare them with eDMRG in terms of the average logarithmic energy variance of each eigenstate (fig. 2.4).

Khemani et al. [49] developed an algorithm based on the fact that MBL eigenstates are approximately product states (see section 2.3). A DMRG algorithm is initialized as a Fock state. For each local update, a full diagonalization of the effective Hamiltonian is conducted. The eigenvector with maximum overlap with the MPS is chosen for the update. This method is rather expensive, $O(\chi^6)$, and works accurately only deep in the MBL phase where resonating states are rare.

Lim et al. [50] used a DMRG optimization on the shifted squared Hamiltonian $\tilde{H}^2$. For each local update, instead of a full diagonalization, the Lanczos algorithm is used to obtain a few eigenvectors. The full system state is built slowly using the infinite-DMRG method [91] and a small bond dimension χ. Once the required system size is reached, χ is slowly increased to improve the quality of the eigenstate. Since this method uses the squared Hamiltonian, convergence rate suffers from the exponentially small gap of highly excited eigenstates, therefore, it is more accurate deep in the MBL phase.

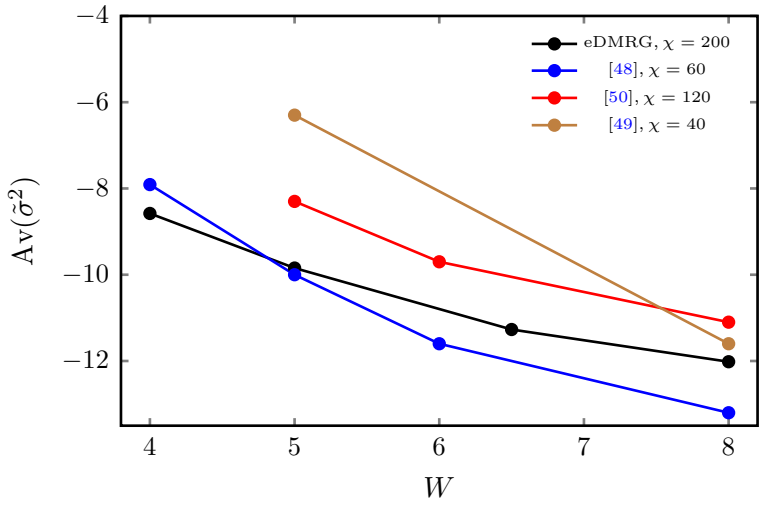


Figure 2.7: Average energy variance for various MPS optimization algorithms for highly excited states. The size of the system is the same $L = 30$ for all implementations with the exeption of [49] ($L = 24$).

A different approach by Yu et al. [48], consists of finding the full spectrum of the effective Hamiltonian H_{eff} for each local update (eq. (1.21)) of the standard DMRG optimization algorithm. After an exact diagonalization, the eigenstate closest to the target energy is extracted and local tensors are updated. In a few sweeps the algorithm converges to some eigenstate around the target energy. The main problem for this approach is the scaling of exact diagonalization ($O(\chi^6)$) for each local update which allows for a maximum $\chi \approx 30$. This limits the applicability of the method to slightly correlated states. They additionally developed a more general shift-invert method for matrix product states (SIMPS). The method minimizes the distance $\left\| H\left|x\right\rangle - \left|b\right\rangle \right\|$ using a local variational sweeping method similar to the eDMRG algorithm.

In the strong disorder limit, all approaches find the eigenstates accurately. Closer to the MBL transition, where the states tend to have large resonant regions, approaches based on operator inversion -eDMRG and [48]- are $1-2$ orders of magnitude more accurate. Interestingly eDMRG is more accurate than SIMPS close to the phase transition. This is due to the use of bigger bond dimension and the conjugate gradient algorithm, instead of small bond dimension and exact inversion.

2.3 Entanglement spectrum of MBL eigenstates

This section presents new results for the structure of ES of MBL systems. It is separated in two parts. Initially we consider typical MBL eigenstates, i.e. states where the LIOM is valid deep in the MBL phase. In the second part we focus on states which include large resonances and thus a LIOM picture does not apply. We argue that if the resonances are well "insulated" by the localized environment, the structure of ES is similar to that of typical MBL eigenstates.

2.3.1 Entanglement structure of MBL Eigenstates

To understand the structure of eigenstates in a system-independent way, it is convenient to switch to quantum information measurements such as quantum entanglement. As was previously mentioned in section 1.1.2, quantum entanglement in a 1D system is measured by the eigenvalues of the reduced density matrix $\rho_{\mathcal{L}} = \mathrm{Tr}_{\mathcal{R}} |\psi\rangle \langle\psi|$, where $\mathcal{L}/\mathcal{R}$ denotes the left/right subsystem, and span L/R lattice sites. The Von-Neumann entropy $S = \mathrm{Tr}_{\mathcal{L}} \rho_{\mathcal{L}} \ln \rho_{\mathcal{L}}$ is often used to classify the complexity of the state. In 1D, the scaling of entropy interpolates between a volume-law ($S \propto L$) and an area-law ($S =$ constant). In the context of correlations, area-law provides exponentially decaying correlations with respect to the size of the partition $\mathcal{L}$. In the opposite limit, volume-law scaling supports any kind of long-range correlations and is a natural law for generic vectors in the Hilbert space spanned by the system.

The eigenstates of MBL systems obey an area-law[1][92]. Thus, at the level of entanglement entropy MBL, *all* eigenstates have an identical scaling to ground states of gapped systems [6], while highly excited eigenstates of ergodic systems feature the generic volume-law scaling.

[1]Rare disorder realizations could produce volume-law states, however the appearance rate of such rare areas vanishes exponentially with respect to the area size, see fig. 2.6. So, in the thermodynamic limit even large rare areas are surrounded by exponentially larger localized environments and the area-law scaling is restored.

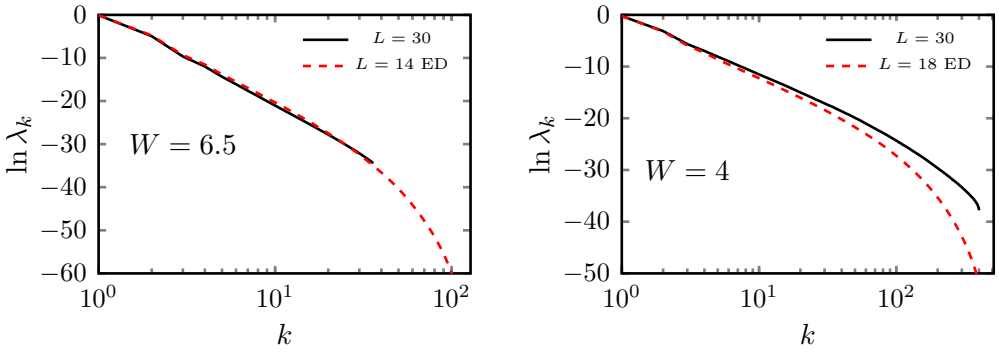


Figure 2.8: Typical disorder average of the density matrix eigenvalues for different disorder strengths and system sizes across half-system partitions. eDMRG and ED curves have the same slope, validating the prediction of the phenomenological picture in the thermodynamic limit.

Since entanglement entropy cannot "distinguish" between MBL eigenstates or gapped ground states, it is natural to search for a more generic entanglement measurement in order to classify MBL eigenstates. More information as to how degrees of freedom are correlated can be obtained by investigating the structure of the reduced density matrix spectrum, namely ES, $\{\lambda_k, k \leq \dim(\rho_{\mathcal{L}})\}$. ES has already been extensively used to describe exotic quantum orders [15, 17, 93, 18]. Beyond the classification of quantum orders, ES of highly excited eigenstates of ergodic systems obey Marcenko-Pastur distribution [94, 37]. Marcenko-Pastur distribution is the signature distribution of random vector sampling in Hilbert space. This means that highly entangled eigenstates of ergodic systems are independent of the Hamiltonian. We show that highly excited eigenstates of MBL systems follow a simple power-law distribution, as an outcome of the LIOM structure of MBL systems. In addition, resonant areas where the QLIOM picture is relevant also feature a power-law structure, where the onset of the power-law is a function of the size of the resonant area.

Deep in the MBL phase, each eigenstate of the Hamiltonian eq. (2.6) can be written using LIOMs around a bipartition as,

$$|\mathcal{I}\rangle = \sum_{\{\tau\}_{\mathcal{L}}\{S\}_{\mathcal{R}}} C_{\{S\}_{\mathcal{L}}\{S\}_{\mathcal{R}}} |\{S\}_{\mathcal{L}}\rangle |\{S\}_{\mathcal{R}}\rangle . \tag{2.9}$$

where the left/right sets of spin indices are defined as $\{S\}_{\mathcal{L}} = S^{[1]} \dots S^{[L]}$

and $\{S\}_{\mathcal{R}} = S^{[L+1]} \dots S^{[R+L]}$. To the 0th order approximation, for every eigenstate, the physical spin basis and the LIOM basis are the same since every eigenstate is a product state $|\mathcal{I}_0\rangle = |0110\dots\rangle$. The 0th order matrix element is taken to be the state with all spins pointing down $|C_{00\dots00}| = O(1)$. Picking a special 0th order matrix element does not affect the calculation, as it only acts as a template upon which spin flips are defined. The eigenstate in terms of the physical spins can be rotated by a quasilocal rotation to the LIOM basis. Each LIOM is an expansion of physical operators, exponentially suppressed with respect to the distance of operators, i.e., eq. (2.3). Thus, the matrix elements of the state in the physical spin basis decay exponentially with respect to the maximum distance between spin flips,

$$\left|C_{0\dots0\underbrace{1010101}_{r}0\dots0}\right| \propto e^{-ar}. \tag{2.10}$$

The inverse localization length a may vary with respect to the disorder pattern. The hierarchy in the matrix elements is a consequence of the couplings in the effective Hamiltonian eq. (2.6). The reduced density matrix elements

$$\begin{aligned} &\rho_{\{S\}_{\mathcal{L}},\{S'\}_{\mathcal{L}}} = \sum_{\{S\}_{\mathcal{R}}} C_{\{S\}_{\mathcal{L}}\{S\}_{\mathcal{R}}} C^*_{\{S'\}_{\mathcal{L}}\{S\}_{\mathcal{R}}} \\ &\Rightarrow \rho_{0\dots0\underbrace{1101}_{r_{\mathcal{L}}},\underbrace{011}_{r'_{\mathcal{L}}}0\dots0} \approx e^{-a(r_{\mathcal{L}}+r'_{\mathcal{L}})} \sum_{r_{\mathcal{R}}=0}^{R} \sum_{\{r_{\mathcal{R}}\}} O(1) e^{-2ar_{\mathcal{R}}} \end{aligned} \tag{2.11}$$

feature a hierarchical structure. As a consequence of eq. (2.10), spin flips around the partition suppress the elements as $e^{-a(r_{\mathcal{L}}+r_{\mathcal{R}})}$. Each radius has a degenerate block of matrix elements $\{r\}$ of size 2^{r-1}. The elements inside the reduced density matrix trace are of $O(1)$ and are not written explicitly in eq. (2.11). The diagonal elements of the density matrix are suppressed to the highest order as $\propto e^{-2ar_{\mathcal{L}}}$. To find the eigenvalues we can perturbatively diagonalize the density matrix starting from the most important sectors, namely $r_{\mathcal{L}} = 0$ or 1,

$$
\begin{pmatrix} \rho_{0,0} & \rho_{0,1} & \dots \\ \rho_{1,0} & \rho_{1,1} & \\ \vdots & & \ddots \end{pmatrix} =
$$
$$
\begin{pmatrix} c_{00}^2 + O(\epsilon^2) & \epsilon c_{00} c_{10}^* + O(\epsilon^3) & \dots \\ \epsilon c_{00}^* c_{10} + O(\epsilon^3) & \epsilon^2 c_{10}^2 + O(\epsilon^4) & \\ \vdots & & \ddots \end{pmatrix} \overset{GE}{=} \tag{2.12}
$$
$$
\begin{pmatrix} c_{00}^2 + O(\epsilon^2) & 0 & \dots \\ 0 & O(\epsilon^4) & \\ \vdots & & \ddots \end{pmatrix}.
$$

By using $\epsilon = e^{-a}$, the matrix elements are written with respect to ϵ, e.g., $C_{01} = \epsilon c_{01}$, where c is of order $O(1)$. We have not written explicitly the trivial part of the non-flipped spins in the density matrix elements. All off-diagonal terms can be removed by Gaussian elimination, sector by sector. The terms that flip unequal number of spins to the left and right partitions of the chain are removed in the diagonalization process. Only the terms $r_{\mathcal{L}} = r_{\mathcal{R}}$ contribute to the eigenvalues. A similar process is used for the perturbative calculation of ES by Alba et al.,[19]. In their work it is found that entropy is produced when the perturbative term -which is the hopping parameter- acts the same number of times to each partition of the chain. In our approximation, this corresponds to the same number of spin flips in each partition. The density matrix eigenvalues are thus,

$$
\begin{aligned}
&\lambda_1 \propto O(1) \\
&\lambda_2 \propto \epsilon^4 \\
&\lambda_{3-4} \propto \epsilon^8 \\
&\vdots \\
&\lambda_{2^{L-1}+1-2^L} \propto \epsilon^{4L}
\end{aligned} \tag{2.13}
$$

In fig. 2.10, the existence of the hierarchical sectors is numerically shown for the XXZ model using exact diagonalization. In order to observe the sectors clearly, the variance of the "typical entanglement gap" $\mathrm{Var}(\ln \lambda_{k+1} - \ln(\lambda_k))$ is used. Jumps in the variance appear for $k = 2, 4, 8, \dots$ indicating that adjacent eigenvalues belong to different hierarchical sectors. As the chain

becomes larger, the jumps beyond the first few sectors smooth out and it becomes harder to distinguish in between sectors. The word "typical" is used to denote that the logarithm of each eigenvalue is used.

The typical statistical measures are used, when the data follow hard-tailed distributions. In [95] it is shown that λ_1 obeys a Levy-distribution, which is a heavy-tailed distribution with mean value being infinity. In [87, 75] the distribution of matrix elements (eq. (2.10)) is shown to feature lognormal statistics (also heavy-tailed). A lognormal distribution has a finite average but requires a very large sample to accurately approximate the mean. In fig. 2.9 the distribution of various eigenvalues is shown for the site disordered XXZ model. Beyond the first few largest eigenvalues the distributions of their logarithms are normal implying that the eigenvalues follow a lognormal distribution.

Since $\lambda_k^{[r_\mathcal{L}]} = e^{-4ar_\mathcal{L}}$ for $k \in \{2^{r_\mathcal{L}-1}+1, \ldots, 2^{r_\mathcal{L}}\}$, we can estimate $r_\mathcal{L} \approx \ln k / \ln 2$. The power-law structure of the ES becomes clear since,

$$\lambda_k \propto \frac{1}{k^{\frac{4a}{\ln 2}}}. \tag{2.14}$$

Fig. 2.8 illustrates the disorder averaged ES around a partition in the middle of the chain. The slope of the curve is constant with respect to the size of the chain indicating that the slope saturates in the thermodynamic limit to a fixed value depending on the disorder amplitude W. The eDMRG curve is cut above the maximum allowed bond dimension which is $\chi_{max} = 200$ for $W = 6.5$ and $\chi_{max} = 400$ for $W = 4$. This happens because of the soft cutoff of SVD (cutoff $= 10^{-16}$) in the eDMRG algorithm. Let's assume that for some eigenstate the soft cutoff kicks in at some $k_{max} < \chi_{max}$, thus $\{\lambda_{k_{max}+1}, \ldots, \lambda_{\chi_{max}}\} = 0$. The logarithm becomes problematic for these eigenvalues since $\{\ln \lambda_{k_{max}+1}, \ldots, \ln \lambda_{\chi_{max}}\} = -\infty$. Eigenvalues feature lognormal statistics, so $\ln \lambda_k$ features Gaussian statistics. A "smart" method is used to find the average over the sample when some states are cutoff below the eDMRG hard cutoff. A Gaussian distribution is symmetric around the mean. Therefore, when a number of $\chi_{max} - k_{max}$ λ_ks in the sample are zero they correspond to the tail of the Gaussian, where exponents are below machine precision. To cancel the missing eigenvalues,

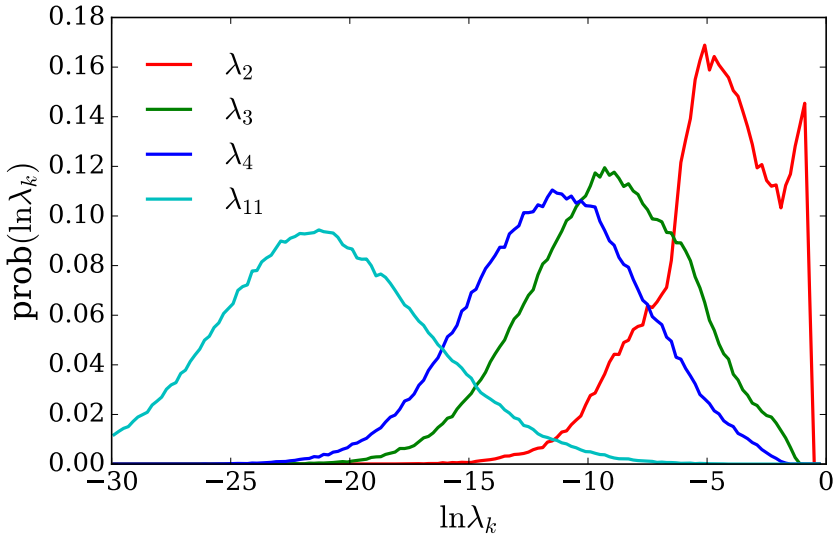


Figure 2.9: Probability distributions of the logarithm of density matrix eigenvalues for $W = 6.5$. The structure of the distributions is approximately Gaussian for small eigenvalues.

the same number of eigenvalues are removed from the opposite tail of the distribution. Since the distribution is symmetric, the mean value will remain unchanged, when the problematic cases and their reflections around the mean are removed. This method works until the tip of the distribution approaches machine precision $\approx e^{-35}$.

2.3.2 Entanglement structure of resonant MBL eigenstates

Eigenstates which include resonant clusters also feature a power-law structure to the ES. The resonant cluster cannot be described by the conventional LIOMs. A quasilocal operator $\tau^{[i,j]}$ with support approximately equal to the "abnormally" disordered area acts as a QLIOM to the resonant cluster. In analogy to classical statistics, the resonant cluster corresponds to a "hot bubble" and the rest of the system to a "cold environment" [96]. There is also a small area around the bubble where the environment is partially thermalized. The environment is taken to be "infinite", thus far from the bubble the temperature of the environment is unaffected by the temperature of the bubble.

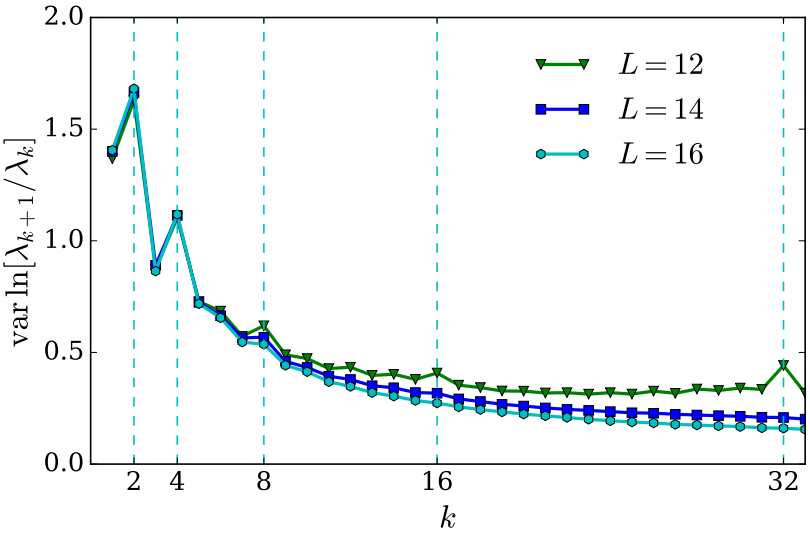


Figure 2.10: Variance of the typical gap of adjacent eigenvalues. Jumps appear at the boundary of each hierarchical sector of the reduced density matrix.

In the phenomenological approach, the environment around the boundary of the bubble is taken to be only slightly thermalized and so a LIOM picture is possible close to the boundary. In analogy to the non-resonant eigenstates, the 0th order expansion of the cold environment is a product state, however, the resonant cluster does not admit a perturbative expansion,

$$
\begin{aligned}
|\mathcal{I}\rangle = &\sum_{S_i \ldots S_j} C_{0\ldots 0 S_i \ldots S_j 0 \ldots 0} \, |0 \ldots 0 S_i \ldots S_j 0 \ldots 0\rangle \\
&+ \sum_{k \in \{1, i-1\}} \sum_{\mathcal{F}_{ik} S_i \ldots S_j} C_{0\ldots 1_k \mathcal{F}_{ik} S_i \ldots S_j 0 \ldots 0} \, |0 \ldots 1_k \mathcal{F}_{ik} S_i \ldots S_j 0 \ldots 0\rangle \\
&+ \sum_{k \in \{j+1, L\}} \sum_{S_i \ldots S_j \mathcal{F}_{kj}} C_{0\ldots 0 S_i \ldots S_j \mathcal{F}_{kj} 1_k \ldots 0} \, |0 \ldots 0 S_i \ldots S_j \mathcal{F}_{kj} 1_k \ldots 0\rangle \\
&+ \sum_{k \in \{j+1, L\}, l \in \{1, i-1\}} \sum_{\mathcal{F}'_{il} S_i \ldots S_j \mathcal{F}_{kj}} C_{0\ldots 1_l \mathcal{F}'_{il} S_i \ldots S_j \mathcal{F}_{kj} 1_k \ldots 0} \\
&\times |\ldots 1_l \mathcal{F}'_{il} S_i \ldots S_j \mathcal{F}_{kj} 1_k \ldots 0\rangle \, .
\end{aligned}
\tag{2.15}
$$

In the second third and fourth terms, we denote by $\mathcal{F}_{kj}$ a 2^{k-j-1} dimensional index which counts all the combinations of spin flips between sites k and j. For a given k, the matrix elements of the second and third term of

the expansion are suppressed $\propto e^{-a(i-k)}$ and $\propto e^{-a(k-j)}$. The elements of the fourth term are suppressed with respect to the distance between the furthest 2 spin flips minus the size of the resonant region, i.e. $\propto e^{-a(k-j+l-i)}$. Intuitively, the spins tunnel "freely" in the resonant area and thus matrix elements do not accumulate significant additional suppression. Let's note that eq. (2.15) contains all matrix elements of the state.

The resonant bubble is conveniently assumed to lie at the center of the chain. In real space the chain is structured as $L_{env} - L_{res} - R_{res} - R_{env}$, where for example L_{res} is the length of the resonant area in the left partition. Each partition spans half chain. In order to make the formalism simpler, the matrix elements are written as $C_{\{S\}_{\mathcal{EL}}\{S\}_{\mathcal{RL}}\{S\}_{\mathcal{RR}}\{S\}_{\mathcal{ER}}}$. The first letter of the subscript denotes either environment "E", or resonant bubble "R". The second letter indicates the position of those indices with respect to the partition of the chain. The indices are defined as:

$$\begin{aligned}
\{S\}_{\mathcal{EL}} &= S_1 \dots S_{i-1}, \\
\{S\}_{\mathcal{RL}} &= S_i \dots S_{\frac{j-i}{2}}, \\
\{S\}_{\mathcal{RR}} &= S_{\frac{j-i}{2}+1} \dots S_j, \\
\{S\}_{\mathcal{ER}} &= S_{j+1} \dots S_L.
\end{aligned} \tag{2.16}$$

The reduced density matrix elements after tracing the right half of the chain are

$$\begin{aligned}
&\rho_{\{S\}_{\mathcal{L}}\{S\}_{\mathcal{RL}}\{S'\}_{\mathcal{RL}}\{S'\}_{\mathcal{L}}} = \sum_{\{S\}_{\mathcal{RR}}\{S\}_{\mathcal{R}}} C_{\{S\}_{\mathcal{L}}\{S\}_{\mathcal{RL}}\{S\}_{\mathcal{RR}}\{S\}_{\mathcal{R}}} C^*_{\{S'\}_{\mathcal{L}}\{S'\}_{\mathcal{RL}}\{S\}_{\mathcal{RR}}\{S\}_{\mathcal{R}}} \\
&\Rightarrow \rho_{0\dots0\underbrace{1101}_{r_{\mathcal{L}}}\{S\}_{\mathcal{RL}},\{S'\}_{\mathcal{RL}}\underbrace{011}_{r'_{\mathcal{L}}}0\dots0} \propto e^{-a(r_{\mathcal{L}}+r'_{\mathcal{L}})} \sum_{r_{\mathcal{R}}=0}^{R_{env}} \sum_{\{r_{\mathcal{R}}\}} O(1) e^{-2a r_{\mathcal{R}}}.
\end{aligned} \tag{2.17}$$

Similarly to the case of non-resonant eigenstates, the reduced density matrix elements feature a spatial hierarchy. However, the hierarchy is not as strong as in the non-resonant case, since the elements in the hot bubble can be arbitrary. The eigenvalues are separated in two classes. Those that do not feature hierarchical structure and are generated by the resonant block of the density matrix and those that are suppressed. The resonant block contributes $\approx 2^{L_{res}}$ eigenvalues. A Gaussian elimination is much more com-

plicated for the resonant eigenstate and similar cancellations to those in the non-resonant case are assumed, where at some distance far enough from the hot bubble only terms which flip equal number of spins in each partition contribute. In this case, this is not exactly true since the resonant area may add a number of flipped spins proportional to the size of the resonance, which are neglected as they do not qualitatively alter the phenomenology. The eigenvalues are thus structured as:

$$\begin{aligned} &\lambda_{1-2^{L_{res}}} \approx \text{ resonant}, \\ &\lambda_{2^{L_{res}}+1} \propto \epsilon^4, \\ &\vdots \\ &\lambda_{2^{L-1}+1-2^L} \propto \epsilon^{4L_{env}}. \end{aligned} \tag{2.18}$$

The small number ϵ is slightly dependent on the size/form of the hot bubble. As it was aforementioned, hot bubble could thermalize a small part of the environment, L_{Tenv}, affecting an additional $2^{L_{res}+L_{Tenv}} - 2^{L_{res}}$ eigenvalues. In this regime, eigenvalues still have a hierarchical structure, but it is not as strong as in the cold part of the environment.

To sum up, the hot bubble, the partially thermalized boundary and the cold environment generate the following structure to the ES,

$$\lambda_k = \begin{cases} \text{arbitrary}, & \text{if } k \leq 2^{L_{res}} \\ \text{approximately power-law}, & \text{if } 2^{L_{res}+L_{Tenv}} \geq k > 2^{L_{res}} \\ \text{power-law}, & \text{if } 2^L \geq k > 2^{L_{res}+L_{Tenv}}. \end{cases} \tag{2.19}$$

To observe the proposed behavior for the resonant eigenstates we create a sample of resonant states and study the typical mean of the ES. To make a resonant region appear on a predefined region of the chain, we vary the amplitude of local disorder. The environment sites have a $W = 10$ amplitude while the resonant sites have $W = 1$. The one order of magnitude difference in order to have minimum environment thermalization from the hot bubble. In the thermodynamic limit this is not needed, however the exponentially increasing size of the Hilbert space allows only small chains to be exactly diagonalized. Therefore, to avoid thermalization of the full

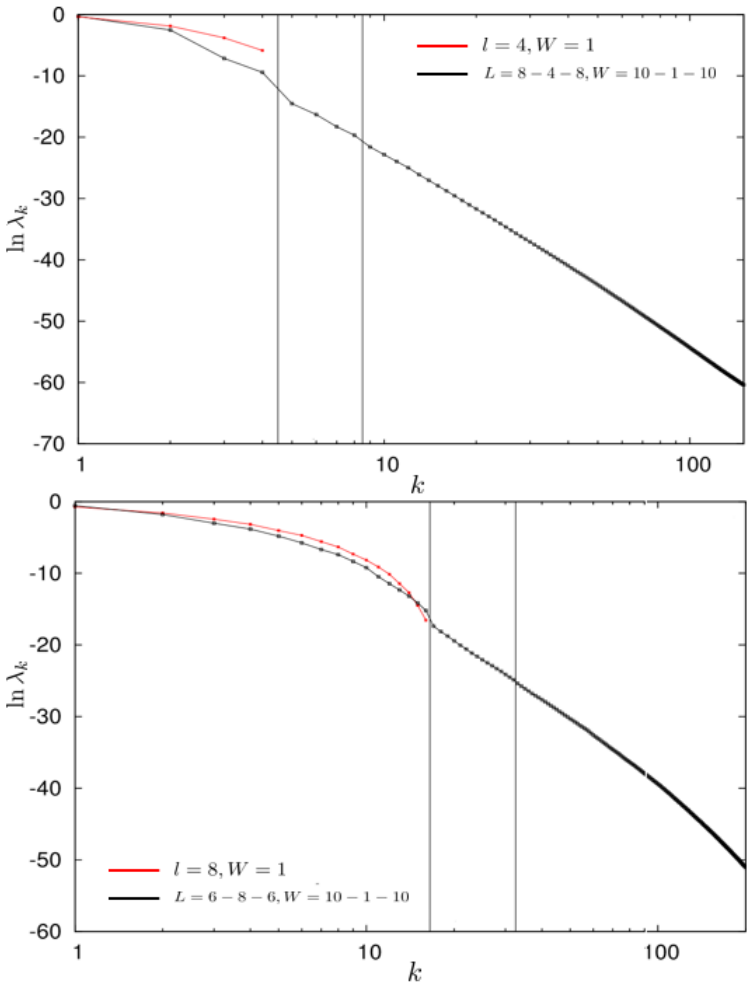


Figure 2.11: Typical mean of ES across a cut in the middle of a strongly disordered -length L- chain with a "hot" -radius l- patch in the middle. The red lines show the corresponding ES of the hot region if it is treated as a closed quantum system. The perpendicular lines at $k = d^l, d^{l+1}$ are guides to the eye.

chain, the environment has to be highly disordered.

Fig. 2.11 illustrates the structure of the spectrum for various sizes of the hot bubble. The perpendicular lines show the part of the spectrum that is affected if the hot bubble partially thermalizes the site closest to the bubble and corresponds to $2^{L_{res}}$ eigenvalues. The slope of the curves $\ln \lambda_k = -\gamma \ln k$ considering the eigenvalues outside the resonant area is approximately the same and independent of the size of the hot bubble $\gamma \approx -13.5$. The constant slope indicates that the slope is a characteristic of the disorder strength of the many body localized system and is independent of rare intermediate resonant regions.

2.4 Discussion

In section 2.2 we presented the eDMRG algorithm, a variant of the standard DMRG algorithm to efficiently target slightly entangled eigenstates of many-body systems, anywhere in the spectrum. eDMRG was applied to the many body localized XXZ chain to verify the area-law of entanglement entropy for much larger systems than previously accessible by exact diagonalization studies ($L = 30$).

This algorithm can be used to investigate whether MBL appears in translation-invariant systems. In translation-invariant systems [97, 98, 99, 100] finite size constraints play a very important role as localization is expected to appear when some parameter is much smaller than some other parameter in the Hamiltonian. For example, mixtures of light and heavy particles. Most of these models are possibly ergodic in the thermodynamic limit. eDMRG can access the thermodynamic limit and thus, it is a tool which can verify or prove wrong the conjectures about MBL in translation-invariant systems.

Another open question in MBL systems is whether mobility edges survive in the thermodynamic limit [96]. Concerns about the existence of mobility edges are based on the assumption that the delocalized eigenstates above the mobility edge act as a hot environment to the rest, leading to the

delocalization of the full spectrum. A study of large chains with eDMRG could clarify whether mobility edges vanish in the thermodynamic limit.

In section 2.3, we illustrated a phenomenological framework to construct quasilocal operators, which form integrals of motion in MBL systems. It was shown that the existence of a complete set of LIOMs characterizes the ES and provides a more complete description of the complexity of eigenstates compared to entanglement entropy. For example, although MBL eigenstates and gapped ground states feature an area-law, the ES of MBL systems have a power-law structure while gapped systems have a faster than power-law structure.

Eigenstates that have resonant regions (hot bubbles) and are, thus, impossible to describe using complete sets of LIOMs, are shown to also feature a power-law scaling in ES. The resonant region only modifies the onset of the power-law, but the non-resonant environment provides a power-law with a characteristic slope of the non-resonant system.

Chapter 3

Strongly interacting bosons in 2-dimensional lattices

In this chapter we explore the physics of strongly interacting bosons in 2D optical lattices. In the section 3.1.2 we introduce Extended Bose-Hubbard (EBH) model [101] and qualitatively explore the nature phases at the strongly interacting limit. In section 3.2, we use an iPEPS algorithm section 1.3, to find the ground state of strongly interacting bosons in honeycomb lattice. We determine the phase diagram of Bose-Hubbard model (BH) and compare it to mean field limit and quantum Monte Carlo simulations [102, 103, 104]. Additionally, entanglement entropy across the insulator to superfluid transition is investigated. Using EBH, we investigate the behavior of bosons in different phases, with respect to the doping of the lattice. Particular focus is given in the Supersolid phase.

In section 3.3 additional synthetic fields are used on top of BH model to realize the flux-1/2 Harper-Hofstadter Hamiltonian [105] using strongly interacting bosons. A parabolic trap is used to create a localized many body wave-packet in a 2D square lattice. Using time-dependent GA, we study the expansion dynamics of the wave-packet in the frustrated lattice.

3.1 Strongly interacting Bosons in optical lattices

3.1.1 From Continuum to Lattice

A collection of bosons is described by the second-quantized Hamiltonian:

$$H = \int d\mathbf{x}\hat{\psi}^\dagger(\mathbf{x})(\frac{-\hbar}{2m}\nabla^2 + V_{ext}(\mathbf{x}) - \mu)\hat{\psi}(\mathbf{x}) + \frac{1}{2}\int d\mathbf{x}d\mathbf{x}'\hat{\psi}^\dagger(\mathbf{x})\hat{\psi}^\dagger(\mathbf{x}')V_I(\mathbf{x}-\mathbf{x}')\hat{\psi}(\mathbf{x}')\hat{\psi}(\mathbf{x}), \tag{3.1}$$

where $V_{ext}(\mathbf{x})$ is a position-dependent external potential (optical lattice, trap, ...), $\psi(\mathbf{x})$ is the second quantized bosonic field and $V_I(\mathbf{x}-\mathbf{x}')$ is the boson-boson interaction potential.

Optical lattice potential. Experimentally, this is often achieved by the interference of counter-propagating laser beams [106]. As the optical lattice potential is taken to be periodic, the field operators are expanded in the Bloch basis[1]

$$\hat{\psi}(\mathbf{x}) = \sum_{n,\mathbf{k}} \hat{a}_{n,\mathbf{k}}\phi_{n,\mathbf{k}}(\mathbf{x}), \tag{3.2}$$

labelled by the band n and quasi-momentum $\mathbf{k}$. $\hat{a}^\dagger/\hat{a}$ are bosonic creation/annihilation operators. If the optical lattice is deep enough and temperature is low, particle excitations from the first to higher bands are suppressed. It is then reasonable to disregard higher bands and assume $n = 0$ in eq. (3.2). Using Wannier functions to write the Bloch state and eq. (3.2) the field operator is written as:

$$\hat{\psi}(\mathbf{x}) = \sum_i \hat{a}_i w_i(\mathbf{x}-\mathbf{x}_i), \tag{3.3}$$

where $\mathbf{x}_i$ are the corresponding minima of the lattice potential.

Particle tunnelling. The optical lattice is assumed to be deep enough

[1]The Bloch basis consists of the eigenfunctions of the free particle in the optical lattice.

to prohibit tunnelling beyond NNs. To understand the validity of this statement, it is easy to check the behaviour of the optical lattice close to the minimum. For example, a simple form for the lattice potential coming from counter-propagating sinusoidal laser beams is

$$V_{OL} = \sum_{i=\{x,y,z\}} V_{0i} \sin^2(\pi i/c), \tag{3.4}$$

where the sum is defined over the real space dimensions and c is the lattice constant. In a deep lattice, we can Taylor-expand around the minimum to get the harmonic approximation,

$$V_{OL} \approx \sum_{i=\{x,y,z\}} V_{0i}(\pi/c)^2 i^2. \tag{3.5}$$

Wannier functions are therefore Gaussian wave-functions. This justifies the absence of long-range hopping. The overlap between Wannier functions centred far from each other will be exponentially small. Hopping matrix elements can be calculated from 3.1

$$J_{ij} = -\int d\mathbf{x} w(\mathbf{x}-\mathbf{x}_i)^*(\frac{-\hbar}{2m}\nabla^2 + V_{OL}(\mathbf{x}))w(\mathbf{x}-\mathbf{x}_j). \tag{3.6}$$

In the case of Gaussian Wannier functions, an analytical expression for eq. (3.6) is based on the solution of Mathieu equation [107]. Using 3.3 the kinetic part of the tight binding model is

$$H_0 = -\sum_{<i,j>} J_{ij}\hat{a}_i^\dagger \hat{a}_j, \tag{3.7}$$

where the symbol $< i,j >$ denotes the sum over i and j where j is constrained to be a NN of i.

Particle interactions. Particles interact by an isotropic contact potential, which is proportional to the s-wave scattering length and (possibly) an additional potential originating from the (electric or magnetic) dipole

moment of the atoms. The total potential has the form,

$$V_I = V_{contact} + V_{dipolar} = g\delta(\mathbf{x} - \mathbf{x}') + \frac{C}{(\mathbf{x} - \mathbf{x}')^3}, \tag{3.8}$$

where g and C are system-dependent constants (see [108]). Substituting $V_{contact}$ in eq. (3.1), the local contribution to the tight-binding model is

$$U_{contact} = g \int d\mathbf{x} \left| w(\mathbf{x} - \mathbf{x}_i) \right|^4. \tag{3.9}$$

In the absence of dipolar interactions, the contact interaction term in Bose-Hubbard model is $U = U_{contact}$. In the presence of dipolar interactions, the matrix elements of eq. (3.1) are given from

$$V_{ijnm} = \int d\mathbf{x} d\mathbf{x}' w^*(\mathbf{x} - \mathbf{x}_i) w^*(\mathbf{x}' - \mathbf{x}_j) V_{dipolar}(\mathbf{x} - \mathbf{x}') w(\mathbf{x} - \mathbf{x}_n) w(\mathbf{x}' - \mathbf{x}_m). \tag{3.10}$$

Using the deep lattice approximation, where Wannier functions are finite within a small area around the lattice centres $\mathbf{x}_i$, the significant matrix elements are the non-local $V_{ijij} \approx \frac{V}{|i-j|^3}$ and the contact term $V_{iiii} \equiv V_{loc}$. For more detailed derivation of the dipolar terms we refer to [109, 110]. Taking into account eqs. (3.3) and (3.8), the tight-binding interaction term can be written as,

$$H_I = \frac{U_{contact} + V_{loc}}{2} \sum_i \hat{n}_i(\hat{n}_i - 1) + \frac{V}{2} \sum_i \sum_{j \neq i} \frac{\hat{n}_i \hat{n}_j}{|i - j|^3}, \tag{3.11}$$

where $\hat{n}_i = \hat{a}_i^\dagger \hat{a}_i$ is the particle number operator.

Trapping potential. When the number of particles is not very large the finite size effects of the trapping potential V_{Trap} may be important. The trap can be considered with an additional term

$$H_T = \sum_i V_{Trap}(i) \hat{n}_i, \tag{3.12}$$

where V_{Trap} is given by

$$V_{Trap}(i) = \int d\mathbf{x} V_{Trap} \left| w(\mathbf{x} - \mathbf{x}_i) \right|^2 \approx V_{Trap}(\mathbf{x}_i). \tag{3.13}$$

It is assumed that the trap is approximately constant in the vicinity of each site.

Extended Bose Hubbard Model. The well known EBH model, manifests from combining eqs. (3.7), (3.11) and (3.12),

$$\begin{aligned} H_{EBH} &= H_0 + H_I + H_{Trap} - \sum_i \mu \hat{n}_i = \\ &= -\sum_{<i,j>} J_{ij} \hat{a}_i^\dagger \hat{a}_j + \frac{V}{2} \sum_i \sum_{j \neq i} \frac{\hat{n}_i \hat{n}_j}{|i-j|^3} + \frac{U}{2} \sum_i \hat{n}_i(\hat{n}_i - 1) + \sum_i (V_{Ti} - \mu) \hat{n}_i, \end{aligned} \tag{3.14}$$

where the additional chemical potential μ controls the particle number and $U_{contact} + V_{loc} = U$. In many cases, long-range terms in the dipolar potential are disregarded, and only the NN contribution is kept. This approximation is necessary when "infinite" system numerical techniques, requiring a finite size unit cell, are used.

3.1.2 Physics of the Ground State (T=0)

In this section, a qualitative characterization of the different phases of the EBH model is given. The system to be considered is a homogeneous version of eq. (3.14),

$$H = -J \sum_{<i,j>} \hat{a}_i^\dagger \hat{a}_j + \frac{V}{2} \sum_{<i,j>} \hat{n}_i \hat{n}_j + \frac{U}{2} \sum_i \hat{n}_i(\hat{n}_i - 1) - \mu \sum_i \hat{n}_i. \tag{3.15}$$

First, the dipolar interactions are switched-off $V = 0$. The phase diagram was first predicted by Fisher et al [101]. Qualitative understanding of the phases can come from the limits $U/J \gg 1$, $U/J \ll 1$.

Mott Insulator. The strongly interacting limit ($U \gg J$) can be understood as the limit where interaction energy is much larger than kinetic

energy. When $J = 0$, the state is an ideal Mott insulator (MI),

$$|\psi_{Mott}\rangle \propto \prod_i (a_i^\dagger)^{n_\mu} |0\rangle \,, \tag{3.16}$$

where $n_\mu = \text{IntegerPart}(\mu/U)$. All sites have an equal integer number of particles n_μ. When $U \gg J > 0$, perturbation theory around $J = 0$ leads to particle-hole excitations with energy $E_{ex} - E_{Mott} \approx U \gg J$. MI phase has an energy gap which protects the phase up to some $J_{crit}(\mu/U)$. Characteristic features of a Mott insulator are the vanishing compressibility $\kappa = \frac{\partial \rho}{\partial \mu} = 0$ and the vanishing superfluid order parameter (eq. (3.20)) [101].

Superfluid. Alternatively, when the kinetic term is dominant ($U \ll J$), the Hamiltonian can be approximated in the non-interacting limit by $H \approx -J \sum_{<i,j>} \hat{a}_i^\dagger \hat{a}_j + \mu \sum_i \hat{n}_i$ and is diagonalized via a Fourier transform. The dispersion relation is $E(k) = -2J \sum_{i=\{x,y,z\}} (\cos(2\pi k_i/L) - \mu)$. The ground state corresponds to a $\mathbf{k} = 0$ vector,

$$|\psi_{SF}\rangle = \frac{1}{\sqrt{N_0!}} (\hat{a}_{\mathbf{k}=0}^\dagger)^{N_0} |0\rangle \,, \tag{3.17}$$

where N_0 is the number of particles at zero momentum (eq. (3.19)). It is common to use the grand-canonical ensemble to write superfluid ground state as a coherent state of fixed average particle number $\langle \hat{a}_i \rangle = \sqrt{N_0/V}$.

$$\begin{aligned} |\psi_{SF}\rangle &= e^{-\frac{|a_{\mathbf{k}=0}|^2}{2}} \sum_n \frac{(a_{\mathbf{k}=0} \hat{a}_{\mathbf{k}=0}^\dagger)^n}{n!} |0\rangle = e^{-\frac{|a_{\mathbf{k}=0}|^2}{2}} e^{\frac{a_{\mathbf{k}=0}}{\sqrt{V}} \sum_i \hat{a}_i^\dagger} |0\rangle \\ &= \prod_i e^{-\frac{N_0}{2V} + \sqrt{\frac{N_0}{V}} \hat{a}_i^\dagger} |0\rangle \,, \end{aligned} \tag{3.18}$$

where a Fourier transform $\hat{a}_{\mathbf{k}=0} = 1/\sqrt{V} \sum_i \hat{a}_i$ is used, V being the volume of the system.

The local density probability distribution of eq. (3.18) is Poissonian, in contrast to the delta function distribution of the Mott insulator phase. Furthermore, the state admits a local factorization which is the reason behind the accuracy of Gutzwiller ansatz (GA) [111] in the superfluid phase. In the non-interacting case, all particles have zero momentum. However, in

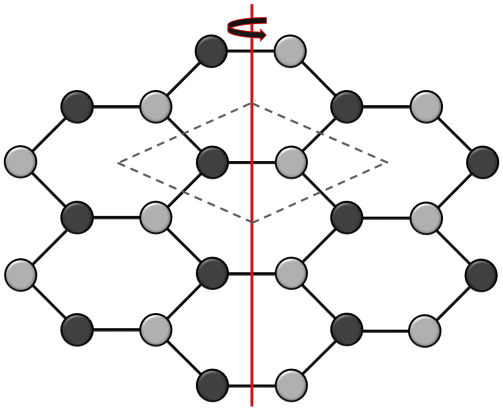


Figure 3.1: Reflection symmetry is spontaneously broken in a system with dipolar interactions. The generators of the symmetry are rotations by π around the red axis, and correspond to the Z_2 symmetry group generators. The dashed boundary denotes the unit cell.

the presence of interactions and close to the Mott insulator boundary, only a fraction of the total particle number N_0, will be in the condensate. An order parameter for the superfluid phase can be defined by the condensate density

$$N_0 = \langle \hat{a}^\dagger_{\mathbf{k}=0} \hat{a}_{\mathbf{k}=0} \rangle = \frac{1}{V} \sum_{ij} \langle \hat{a}^\dagger_i \hat{a}_j \rangle \,. \tag{3.19}$$

The number of particles in the condensate is finite only when long-range correlations are finite. This leads to a superfluid order parameter [101],

$$\lim_{(i-j)\to\infty} \langle \hat{a}^\dagger_j \hat{a}_i \rangle = \left| \langle \hat{a}_i \rangle \right|^2 > 0. \tag{3.20}$$

Characteristic features of the superfluid state are: The fractional expectation value of local density (more precisely the parameter range where the density is integer has measure zero), vanishing energy gap between the ground state and the first excited state, the finite compressibility and the finite superfluid order parameter.

If NN dipolar interactions are turned on, the reflection symmetry of the lattice is spontaneously broken fig. 3.1. The dipolar term tends to create states with unequal number of particles in NN sites. A rotation of the lattice by π doesn't result to the same state, which corresponds to a Z_2 symmetry breaking. Combinations of Z_2 and $U(1)$ symmetry breaking are responsible for the various phases observed.

Density Wave. The Density wave (DW) is an insulating phase similar to Mott insulator. The main difference between them being that, in case of the DW, the translation invariance (Z_2 symmetry) is broken. This behavior appears in the limit $zV > U \gg J$ and similarly to the Mott insulator, it features a vanishing superfluid order parameter and compressibility. Local density expectation values on NNs are different, but remain integers $\langle \hat{n}_i \rangle \neq \langle \hat{n}_j \rangle$.

Supersolid. It turns out that SF phase is not the only gapless phase in the presence of dipolar interactions [112]. Supersolid (SS) is usually formed by doping a density wave solid, where doping defects delocalize and undergo a Bose-Einstein condensation transition. Therefore, SS is expected to appear around density wave phase boundaries. In case of 2D square [113, 102] and 3D cubic [114, 115] lattices, quantum Monte Carlo studies have shown the existence of a SS phase at and below half-filling. This means that beyond 1D, doping a density wave solid is not an essential step to create a SS. A SS phase features different number of particles on neighboring sites $\langle \hat{n}_i \rangle \neq \langle \hat{n}_j \rangle$, in accordance with its partial density wave nature. Since $U(1)$ symmetry is spontaneously broken, the average number of particles at each site is fractional. Compressibility and superfluid order parameter are finite, similarly to a SF. However, since the system has a broken Z_2 symmetry, it is appropriate to redefine the order parameter using modified creation and annihilation operators as:

$$\hat{A} = \frac{1}{2}(\hat{a}_i + \hat{a}_j), \tag{3.21}$$

where i and j denote NN sites. The generalized order parameter can then be written as $\left|\langle \hat{A} \rangle\right|^2$.

Supersolidity has yet to be observed in cold atom experiments in a lattice. In a continuous space, experiments are focused on solid ^{4}He. In an early study by Kim and Chan [116], non-classical rotational inertia was associated with superfluidity in the solid. Later studies showed that non-classical inertia originate from elastic changes associated with dislocations [117, 118]. However, experiments that measure mass flow at low temperature seem to observe signs of supersolidity [119, 120, 121]. Being able to

Table 3.1: Overview of the different order parameters used to define the phases of EBH model. Indices i, j denote NN coordinates and $\rho_i = \langle \hat{n}_i \rangle$, $\bar{\rho} = 1/2(\rho_i + \rho_j)$.

Phase	$\bar{\rho}$	$\rho_i - \rho_j$	$\left\lvert \langle \hat{A} \rangle \right\rvert^2$
Mott Insulator	integer	0	0
Superfluid	fractional	0	finite
Density Wave	fractional	integer	0
Supersolid	fractional	fractional	finite

pinpoint accurately the supersolid regime in the phase diagram, would, give accurate directions for cold atom experiments.

In addition to the aforementioned phases, a Haldane Insulator phase exists in 1D EBH model [122]. Haldane phase is a topological phase which falls beyond the Landau paradigm, as it is not characterized by a local order parameter. It is an example of "Symmetry protected topological" (SPT) phase [123], meaning that: a. the topologically non-trivial phase cannot be deformed continuously to a topologically trivial state if the deformation preserves the symmetry and b. the state can be encoded in a finite depth quantum circuit, i.e., entanglement entropy obeys an area-law. In case of soft-core bosons with local Hilbert space dimension $d = 3$, the corresponding Hubbard model can be mapped to a spin-1 model, using Holstein-Primakoff transformation [124]. Haldane phase is thoroughly analysed for the spin-1 model in [18].

Entanglement Entropies. Deeper insight into the nature of states comes from entanglement entropies. It was already mentioned that in 1D gapped states of local Hamiltonians, entanglement entropies follow an area-law. In contrast, superfluid phase is gapless, thus, entanglement entropy features a logarithmic divergence which can be calculated by (1+1)D CFT [10].

In 2D, entanglement entropy scaling was explored analytically in [13, 125]. Using slave-boson approach, I. Frérot et al. verified the analytical predictions [14]. Entanglement entropy in the ground state of BH model

has a generic form

$$S(L) = aL + \frac{n_G(d-1)}{2} \ln L, \tag{3.22}$$

where n_G is the number of Nambu-Goldstone modes. In the MI phase $a \propto \ln U/U^2$ and $b = 0$. In the SF phase $a \propto \sqrt{U}$ and $b = 0.5$. As expected, deep in the SF phase the area-law factor vanishes in agreement with Bogoliubov theory [126]. In contrast, the gapped MI phase features a strict area-law. Interestingly, deep in the insulating phase and deep in the SF phase, area-law is suppressed by small pre-factors. In the $J = 0$ insulating limit this is a trivial result as the state is not entangled. Deep in the superfluid $\lim_{V\to\infty} S/V \approx 0$, providing the reason that coherent states (3.18) approximate accurately weakly interacting bosons, see eq. (C.17).

In case of the EBH model it is reasonable to expect that eq. (3.22) holds for some more complicated prefactor a. We expect that since PEPS capture the dominant term of eq. (3.22), it is possible to approximate faithfully correlations over a relatively large area. At some point, extra entanglement originating from the logarithmic term, will require higher bond dimension. This mostly affects long-range correlation functions.

3.2 iPEPS approximation of the ground state

In this section, iPEPS (section 1.3) is used to approximate the EBH model. The local Hilbert space is truncated to either $d = 3$ or $d = 4$ depending on the truncation errors. When $\mu/U > 1$, truncation errors can shift measurements, or even location of phases significantly if $d = 3$. For this reason, the constraint $\mu/U = 1$ is used as an upper boundary for $d = 3$.

The Hubbard models are studied using the superfluid order parameter as defined in eqs. (3.20) and (3.21), the local densities on NN sites, the average density of NN sites and the corresponding compressibility,

$$\begin{aligned} \rho_i &= \langle \hat{n}_i \rangle \,, \\ \bar{\rho} &= 1/2(\rho_i + \rho_j), \\ \kappa &= \frac{\partial \bar{\rho}}{\partial \mu}. \end{aligned} \tag{3.23}$$

To quantify quantum fluctuations the local entanglement entropies are calculated,

$$\begin{aligned} S_1 &= \mathrm{Tr}\, \hat{\rho}_i \ln \hat{\rho}_i, \\ S_2 &= \mathrm{Tr}\, \hat{\rho}_{ij} \ln \hat{\rho}_{ij}, \end{aligned} \tag{3.24}$$

where $\hat{\rho}_i$ is the local density matrix and $\hat{\rho}_{ij}$ is the density matrix of NN sites. The diagnostics used to calculate the phase diagrams are summarized in table 3.1.

The Z_2 symmetry breaking cannot be captured by the two-tensor iPEPS consistently without an explicit conservation of the symmetry (the two states associated by the reflection have exactly the same energy). This means that instead of a ground state in one of the two sectors of Z_2, the converged state is a superposition of the ground states in each sector, $|\psi\rangle = a\,|\psi_1\rangle + b\,|\psi_2\rangle$. The "amount" of error can be accurately estimated for the EBH model in a DW phase, since the expectation values of the local densities must be integers and have a checkerboard structure. For example, in the DW phase where the NN densities are $\{\rho_i, \rho_j\} = \{0, 1\}$ for $|\psi_1\rangle$, the densities of the reflected state, $|\psi_2\rangle$, are $\{\rho_i, \rho_j\} = \{1, 0\}$. Assuming a superposition $|\psi\rangle$ of the two states, it is expected to have $\{\rho_i, \rho_j\} \approx \{|a|^2, |b|^2\}$. In numerics the ratio is found to be $|a|^2 / |b|^2 \approx 1\%$, which means that the

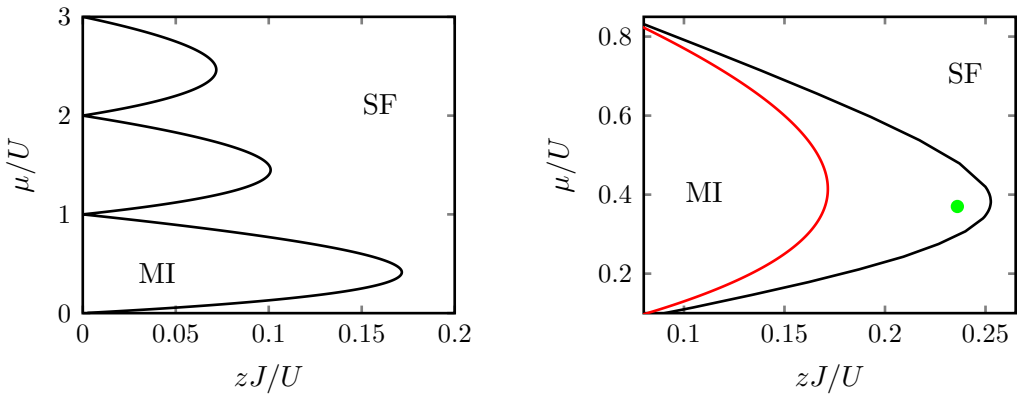


Figure 3.2: *Left*: First three Mott lobes analytically calculated using mean field theory. *Right*: Mean field (red) and iPEPS $\chi = 3$ (black) lowest Mott lobes. The green node denotes the tip of the lobe on the square lattice calculated via a quantum Monte Carlo algorithm [103]. Lower connectivity of Honeycomb lattice results in a sharper Mott lobe tip, indicating stronger quantum fluctuations.

explicit conservation of Z_2 symmetry is not necessary to achieve satisfactory precision. In addition, there is no mathematical reason to expect that the aforementioned source of error affects the boundaries between critical and non-critical phases in the model, since those boundaries are associated with a $U(1)$ symmetry breaking which is captured accurately.

3.2.1 Bose-Hubbard model

Initially, dipolar interactions are set to zero, $V = 0$. In fig. 3.2(left), the boundaries of the Mott-Insulator and Superfluid phases are calculated analytically using second order perturbation theory and the GA [127, 111], (chapter C). GA is a product state ansatz for the ground state $|\psi\rangle_{GA} = \prod_i \sum_{n_i} f_i^{[n_i]} |n_i\rangle$[2]. GA is formally a PEPS with bond dimension $\chi = 1$. As it is a product state, non-local quantum fluctuations are ignored. Since quantum fluctuations are more pronounced in lattices with small connectiv-

[2]An alternative interpretation of GA is the self-consistent, site decoupled mean field theory [128]. In GA the full Hamiltonian is optimized against a quantum state that is constrained to be product state. In mean field theory the Hamiltonian is local, coupled to a classical mean field which approximates the non-local effects, but the states are not constrained.

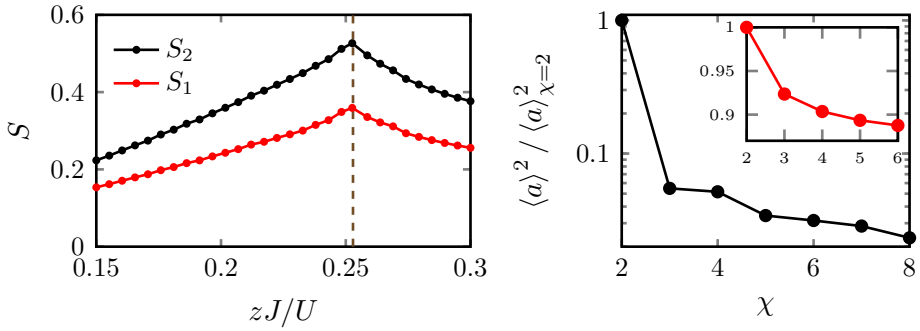


Figure 3.3: *Left*: Local entanglement across the MI-SF transition at integer filling. *Right*: Superfluid order parameter with respect to the bond dimension of the iPEPS wavefunction close to the tip of the Mott lobe ($zJ = 0.28$, $\mu/U = 0.4$). The order parameter is normalized by the order parameter for bond dimension $\chi = 2$. *Inset*: The same plot further away from the tip of the lobe ($zJ = 0.21$, $\mu/U = 0.1$).

ity, GA becomes less quantitative with decreasing connectivity. Honeycomb lattice has connectivity $z = 3$ (in 1D $z = 2$, square lattice $z = 4$). This results in significant corrections to the GA wave-function as the bond dimension is increased from $\chi = 1$. In the right plot of fig. 3.2, the mean field phase diagram and the correction to the first Mott lobe of the diagram using ($\chi = 3$) iPEPS are illustrated. The correction is more important around the tip of the lobe. This is an indication that non-local quantum fluctuations are maximal in the area around the tip. To further compare the size of fluctuations, the position of the tip for the square lattice ($z = 4$) from a QMC study [103] was added. The critical tunneling parameter for the Honeycomb lattice is larger than that of the square lattice $z_{hon} J^{[hon]}_{crit} \approx 1.08 z_{square} J^{[square]}_{crit} \approx 0.252$, which is an expected finding and verifies the accuracy of iPEPS.

As we have already discussed, deep in the superfluid regime the entanglement scales logarithmically, so in 2D, the tips of the insulating lobes are the points with the highest quantum fluctuations for the whole range of the tunnelling parameter. The MI to SF phase transition is generically Commensurate-Incommensurate (CI) and belongs to the Gaussian universality class. By varying the tunnelling parameter across the Mott tip, the phase transition occurs at constant density (integer filling). For the 2D square lattice, it belongs to the 3D XY universality class [101]. The CI

transition is shown in the left plot of fig. 3.5. Entropy has a minimum at approximately $\mu = U$. When chemical potential is approximately equal to the interaction strength, an arbitrary small tunnelling parameter always leads to superfluidity (see fig. 3.2). Thus, at $\mu = U$ (J =constant), the boson gas is deeper in the superfluid phase denoted by the minimum of entropy.

Across the transition at the Mott lobe tip, driven by the the hopping strength, we observe a sharp singularity of entanglement entropy (left plot of fig. 3.3). This result validates the slave-boson prediction for the square lattice [14] and generalizes it to the honeycomb lattice. To get the precise scaling around the critical point, larger reduced density matrices are needed. However, TRG is not an optimal method for that purpose.

In the right plot of fig. 3.3, the dependence of the superfluid order parameter is measured against the bond dimension of the state. In the main plot, the state targeted lies close to the tip of the Mott lobe. The corrections to the order parameter are important especially for $\chi = 2$. Even for large bond dimension convergence is not fully achieved $\langle \hat{a} \rangle^2_{\chi=8} \approx 0.8 \langle \hat{a} \rangle^2_{\chi=7}$. In contrast to the superfluid order parameter, energy is well converged $E_{\chi=8} \approx (1 + O(10^{-4}))E_{\chi=7}$. The inset plot illustrates the behavior of fluctuations further away from the Mott tip. In that case, the superfluid order parameter converges much faster. Even for $\chi = 3$ the prediction is quite accurate, validating the efficiency of iPEPS algorithm for relatively small bond dimensions in "almost" (aside from the area very close to the tip) all of the parameter space of BH model.

3.2.2 Extended Bose-Hubbard model

By switching on dipolar NN interactions, the phase spectrum is enriched by the broken Z_2 symmetry phases, namely, density waves and supersolids. In this study, the parameters $J = 1, U = 15J$ are fixed. In addition to the MI and SF phases, the phase diagram (fig. 3.4) includes two density wave, DW1 (1,0) and DW2 (2,0), and a SS phases. The phase diagram is compared to the quantum Monte Carlo simulation [104]. The agreement is very good around the DW1 lobe and both methods predict the same volume

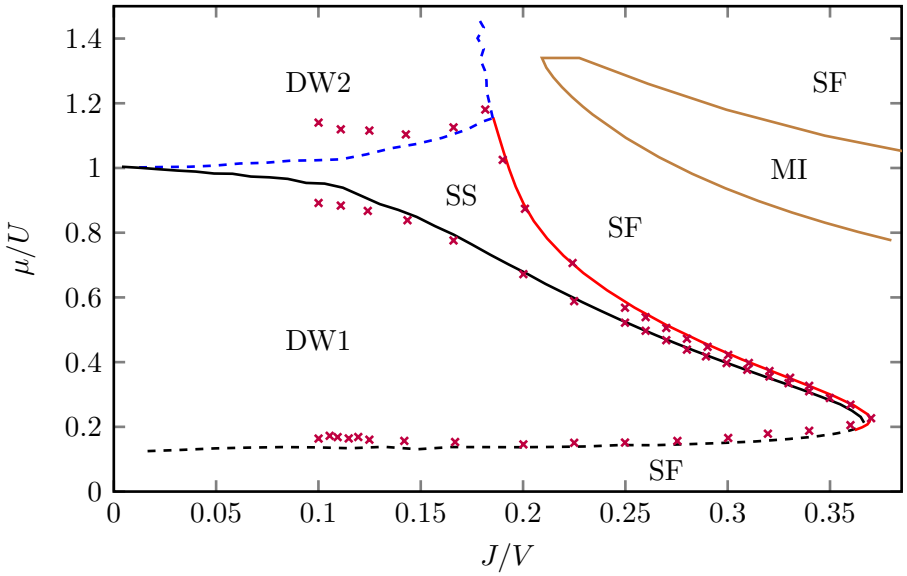


Figure 3.4: Phase diagram of EBH model for $U = 15J$, $J = 1$. Dashed lines denote first order phase transitions and continuous lines denote second order phase transitions. The bond dimension is $\chi = 3$. Cross marks indicate the phase boundaries from the quantum Monte Carlo study [104]. DW1 phase corresponds to a $(n_i, n_j) = (1, 0)$ and DW2 corresponds to a $(2, 0)$ filling, where i,j are NNs.

for the supersolid area. Slight disagreement is observed towards $V \Rightarrow \infty$. In that regime, iPEPS algorithm should be more accurate as the state is approximately factorized and is expected to give accurate predictions. For $\mu > U$, the mismatch between the phases becomes larger (not shown in the diagram). For example, the DW2 and MI phases have a common boundary in [104], while there is a clear separation of the phases by an intermediate SF phase in our study.

For low doping, $\mu < U$ the phase is DW1 for small tunnelling parameter, $J \ll V$. By lowering dipolar interactions, $U(1)$ symmetry is spontaneously broken resulting to a critical phase (either SF or SS). Further lowering of dipolar interactions, as $V \to 0$, the constraint $U = 15J$ can either result in a MI or SF phase (depending on the doping) and reflection symmetry is restored. Doping additional particles to DW1 phase causes the doped defects to delocalize and undergo a Bose-Einstein condensation transition, while Z_2 symmetry remains broken. The SS phase appears on top of DW1 lobe for all dipolar interaction strengths. However, a SS phase extends over

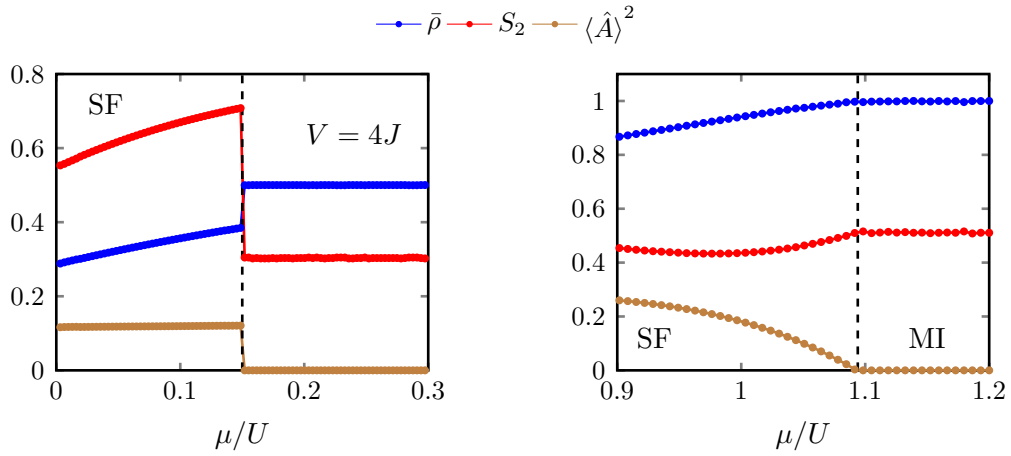


Figure 3.5: *Left*: Average unit cell density, entanglement entropy and order parameter at SF-DW1 transition. All measurements feature a discontinuity at the first order phase transition. *Right*: The SF-MI transition.

a considerable range of doping only when $|zV - U| \approx zJ$. By doping the SS phase further, a phase transition to a SF or a (2,0) density wave takes place.

Before going in more detail about each phase transition, we notice that no signs of a supersolidity at or below half-filling were found. Fig. (3.4) shows SS phase going slightly below the DW1 tip. However, by increasing the bond dimension we found that supersolidity below and at the tip was an artifact of small bond dimension. As supersolidity at half-filling seems to be a property of "more" connected lattices and is completely absent in 1D [129], identifying it in honeycomb lattice (if it exists) could be a rather sensitive process.

SF-DW1. SF and DW1 phases have different broken symmetries $U(1)/Z_2$. According to the Landau-Ginzburg-Wilson paradigm, a phase transition involving phases with different symmetries broken is first order unless an intermediate phase, where both symmetries are broken exists in between them. In the case of low doping and strong dipolar interactions, the SF phase at zero doping, transforms to the DW1 density wave phase, fig. 3.5. The order parameter remains approximately constant up to the transition, where it vanishes discontinuously. Entropy of the reduced density matrix increases up to the transition and then drops to a constant value in the DW1 phase. The constant value of entropy with respect to the chemical

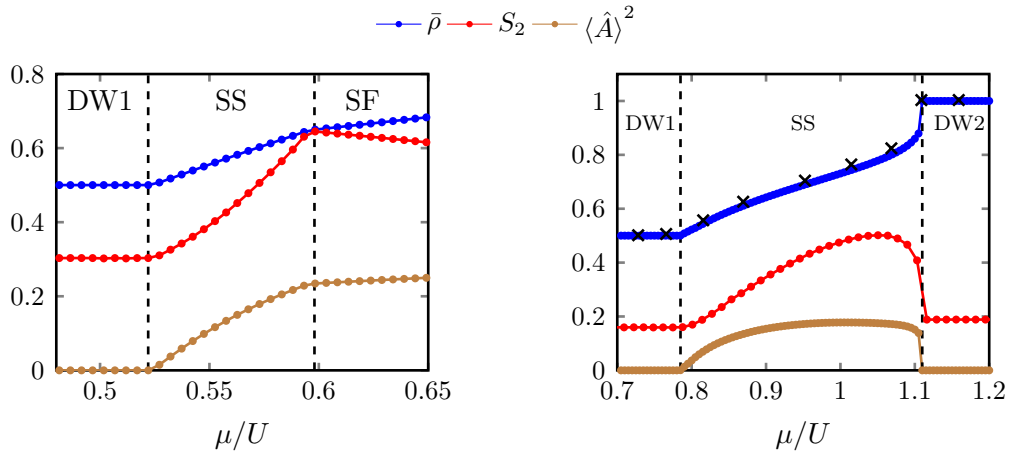


Figure 3.6: *Left*: Average density, entropy and superfluid order parameter across the DW1-SS-SF transitions for $V = 4J$. *Right*: Same quantities ploted across the DW1-SS-DW2 transitions for $V = 6J$. The black crosses denote the result of the QMC study [104].

potential in the insulating phases can be understood perturbatively (to any order). Any perturbative term is an action of hopping terms to the trivial factorized state at $J = 0$. Perturbative corrections conserve the total particle number, so expansions of any order are independent of the chemical potential.

DW1-SS. In contrast to the first order SS-DW1 phase transition, the DW1-SS transition is second order, Gaussian. This is in agreement with the theoretical predictions of [130], where a dual vortex method is used to study the transitions between density waves and supersolids. The scaling of superfluid order parameter at the boundary satisfies

$$\langle A \rangle^2 \propto \left|\bar{\rho} - 1/2\right|^{(2+z-2)\nu} \overset{\text{Gauss.}}{\approx} \left|\bar{\rho} - 1/2\right|, \tag{3.25}$$

where the exponents for the transition are the same as for the MI-SF transition, $z = 2, \nu = 1/2$, with possible logarithmic corrections [101].

SS-DW2. The behavior of the SS phase depends on the doping and magnitude of dipolar interactions. If dipolar interactions are strong, DW1 phase is stable for larger doping. Both local densities in the unit cell increase with respect to the doping up to approximately $\mu \approx U$, see fig. 3.7. At that

point, the density of the site that was empty at the transition reaches a local maximum. This point has a peak in quantum fluctuations as well, since the entropy of the unit cell has a local maximum (fig. 3.6). Particle fluctuations are approximately constant over a large range of doping. Intuitively, the boson gas has a tendency to shift to the SF and to the DW2 phases. When $\mu > U$, the additional doping favours the DW2 phase leading to a first order phase transition to the $(2, 0)$ solid phase. Lattice compressibility (eq. (3.23)) features a deep minimum around $\mu \approx U$, which signifies that the tendency to form a SF phase becomes weaker than the tendency to shift to the DW1 phase.

SS-SF. As dipolar interaction gets weaker, the DW1 lobe becomes unstable for lower doping. The SS phase occupies only a "thin" layer in the phase diagram, before the diagonal order is completely lost resulting in a second order phase transition to a SF phase. Increasing the doping in the SS phase increases the local density of the empty site of the solid but does not change the density of the filled site, (fig. 3.7). When the density of NNs becomes equal, the phase transition, to the SF phase occurs. At the point of transition the entropy of the unit cell is maximal. Additional doping in the SF phase reduces quantum fluctuations. It is not possible to study the type of transition with the iPEPS algorithm as iPEPS do not naturally capture the logarithmic violations of the area-law of entanglement entropy. Quantum Monte Carlo studies on a square lattice have shown that it belongs to the 3D Ising universality class [102]. In contrast to the SS-DW2 transition, compressibility is approximately constant in the SS regime. Intuitively this means that the tendency of the gas to form a SF phase is much bigger (for any doping) than the tendency to form a DW2 phase.

Depending on the phases on the boundary of the SS phase, doping has rather different effect on observables. More importantly, lattice compressibility $\kappa = \frac{\partial \bar{\rho}}{\partial \mu}$ is approximately constant if the next phase is SF and has a deep minimum if the next phase is DW2.

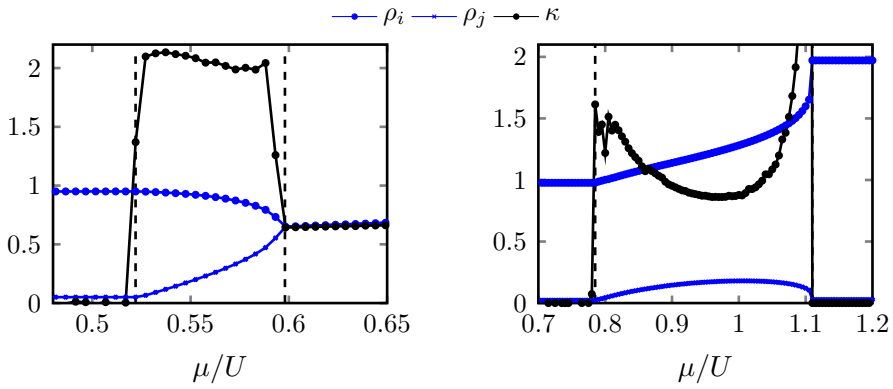


Figure 3.7: *Left*: Densities on NN sites and compressibility of the unit-cell across the DW1-SS-SF transitions for $V = 4J$. Compressibility across the SS phase is approximatelly constant. *Right*: The same plot for the DW1-SS-DW2 transition for $V = 6J$. Compressibility across the SS phase has a deep minimum, signature of a subsequent DW2 phase.

3.2.3 Discussion

We have studied strongly interacting bosons in honeycomb lattice. In the BH model ($V = 0$) the iPEPS algorithm is tested close to the highly entangled tip of the Mott lobe. We have found that particle fluctuations are much more sensitive near the Mott lobes than anywhere else in the spectrum. The phase diagram for the first Mott lobe is computed and compared to the mean field lobe and the lobe of the square lattice. Mean field severely underestimates the size of the lobe, due to the small connectivity of the lattice. Additionally, the lobe is approximately 10% bigger than the lobe of the square lattice. Our results are complementary to the study of hard-core bosons by J. Jordan et al. [131].

Adding dipolar interactions the phase spectrum becomes richer. Various phases were studied, especially the behavior of the SS phase with respect to the doping. We found good agreement with quantum Monte Carlo simulations [104], in phase diagram and local density. The particle fluctuations of the iPEPS don't seem to agree with any of the published quantum Monte Carlo studies [104, 132], in either SS or SF phase. It is noteworthy that the two published studies disagree with each other, while iPEPS results seem to lie somewhere in between. The iPEPS results were converged with respect

to the bond dimension and the imaginary time evolution which strongly suggests that the considerable mismatches are not due to iPEPS errors.

iPEPS algorithm can provide an interesting tool to study various phenomena. In particular we believe that PEPS is a key ansatz to (non-perturbatively) search for MBL in >1D systems. The eDMRG algorithm, described in the previous section can be translated to the PEPS language as a modification of the variational scheme described in [133]. The cost of variational algorithms for PEPS is much higher than DMRG, however, we believe that it is still not prohibited.

3.3 Cloud expansions of the strongly interacting Harper-Hofstadter Hamiltonian

In the previous section, we have shown that various quantum phases arise from the competition between kinetic and potential energy terms. The scattering length is controlled by Feshbach resonances, by applying an external magnetic field. In addition to the control of interactions, it is possible to couple synthetic gauge fields to neutral ultracold bosons. Engineering forces, similar to Lorentz force on electrons, is possible by using rotating/shaking lattices [134, 135] or laser-assisted tunneling [136, 137, 138]. When a rotation around a lattice cell is of the order of a flux quantum, interesting phenomena appear. In the case of the Harper-Hofstadter Hamiltonian (HH), a fractal energy spectrum emerges [105].

An interesting problem for atomic clouds is understanding of their expansion dynamics, i.e., when the trap is suddenly switched-off and the cloud is free to expand. In strongly interacting lattice systems, expansion dynamics can lead to interesting and unexpected results. We refer to [139] for a review in 1D systems. For higher dimensional systems the expansion dynamics have been studied using the time-dependent GA [140, 141, 142]. Experimentally, expansions have been observed for bosonic [143, 144] and fermionic [145] systems.

In the hard-core limit, $\rho < 1$, of BH model, the expansion is ballistic [146], while in the soft-core limit, $\rho > 1$, the core of the cloud gets self-trapped [142]. In this work, we combine the flux-1/2 limit of the HH model (see fig. 3.8), and strongly interacting bosonic clouds. The resulting Hamiltonian is a synthetic BH (SBH) model (eq. 3.26), where the hopping J is a complex number, with a phase pattern that corresponds to a flux-1/2 lattice.

We use phenomenological arguments and time-dependent GA to show that the expansion dynamics of the frustrated BH Hamiltonian are qualitatively different from the non-frustrated case. In brief, we find that in the hard-core limit the cloud is self-trapped, while in the soft-core limit the self-trapping produced by the frustration is not as strong as the self-trapping

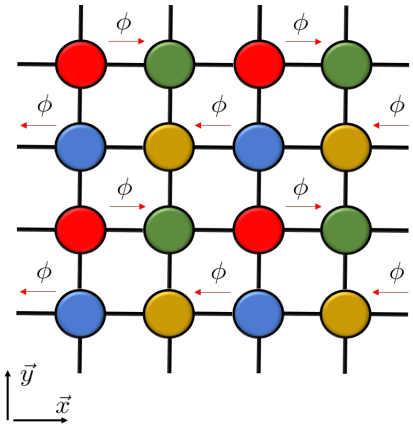


Figure 3.8: 2D lattice with an additional synthetic field. The field is applied according to the arrows and adds a phase ϕ to particles hopping to the direction of the arrow and the opposite phase for the opposite hops. The flux-1/2 lattice corresponds to $\phi = \pi$. The unit cell of BH model is broken to a unit cell containing 4 sites which are coloured differently.

produced by immobile doublons (quasiparticles composed of two particles in a single site).

Model. The synthetic field is applied to the lattice as seen in fig. 3.8. The new unit cell of the lattice contains four lattice sites. Each dimension of the lattice is decomposed to two even/odd sublattices. The 2D lattice sites are labelled as even-even (red), even-odd (green), odd-even (blue), odd-odd (yellow). The Hamiltonian has the standard BH terms with the exception of the hopping which is now complex valued,

$$H = -\sum_{<i,j>} (J_{i,j}\hat{a}_i^\dagger \hat{a}_j + H.C.) + \frac{U}{2}\sum_i \hat{n}_i(\hat{n}_i - 1) - \sum_i (\mu - V_{trap}(i))\hat{n}_i. \quad (3.26)$$

The hopping term has a constant magnitude $|J|$. The trapping potential $V_{trap}(i) = V_0 \mathbf{r}_i^2$ is a parabolic potential, positioned in the centre of the lattice. In section C.2.3 the effects of parabolic traps on a strongly interacting cloud are presented. Cloud expansions require very large lattices for numerical simulations. In this study, GA is employed, $|\psi\rangle_{GA} = \prod_i \sum_{n_i} f_i^{[n_i]} |n_i\rangle$. Time evolution of GA is possible by solving TDVP [147, 148],

$$\partial_{\langle\psi|}(\langle\psi| (-i\frac{d}{dt} + H) |\psi\rangle) = 0. \quad (3.27)$$

A detailed solution of the equation is illustrated in section C.2.2. The equations of motion (EOM) for the state elements are:

$$i\hbar\frac{df_{n_i}^{[i]}}{dt} = \left(U\frac{(n_i-1)}{2} - \mu + V_{trap}(i)\right)n_i f_{n_i}^{[i]} - \Phi_i\sqrt{n_i}f_{n_i-1}^{[i]} - \Phi_i^*\sqrt{n_i+1}f_{n_i+1}^{[i]}, \tag{3.28}$$

where the mean fields $\Phi_i = \sum_{<j>_i} J_{ij}\sum_{n_j=0}^{n_{max}} f_{n_j}^{[j]*} f_{n_j+1}^{[j]}\sqrt{n_j+1}$, include the contributions of all sites j around site i. $J_{ij} = Je^{\pm i\phi}$, where ϕ depends on the phase added for a hop of a particle from site j to site i. The systems are simulated on a 320×320 lattice and the local Hilbert space dimension cutoff is set to $n_{max} = 8$. The quantities of interest are local density, $\rho_i = \langle\hat{a}_i^\dagger\hat{a}_i\rangle$, and the momentum distribution function:

$$\rho(\mathbf{k}) = \frac{1}{L^2}\sum_{i,j} e^{i\mathbf{k}(\mathbf{r}_i-\mathbf{r}_j)}\langle\hat{a}_i^\dagger\hat{a}_j\rangle \overset{GA}{=} N - N_0 + \left|a(\mathbf{k})\right|^2, \tag{3.29}$$

where $a(\mathbf{k}) = 1/L\sum_i e^{-i\mathbf{k}\mathbf{r}_i}\langle\hat{a}_i\rangle$, N and N_0 are total particle number and condensate faction (eqs. (C.9) and (C.10)). The non-trivial part of the momentum distribution function is $\left|a(\mathbf{k})\right|^2$, and is, therefore, used to quantify the momentum distribution of the cloud. The Planck constant is taken to be $\hbar = 1$.

Technical details of the algorithm implementation. To solve the EOMs, a 4th order Runge-Kutta method is used [149]. The trunctation error per time step is $O(dt^5)$. In GA, the EOMs eq. (3.28), are solved in parallel for each site. At the end of every Runge-Kutta step, the mean fields are updated. In 2D square lattice, the cost of a time step is $O(L^2)$, where L is the number of lattice points across one dimension. The nature of this work requires large lattices as the size of the lattice constraints the total time of the simulation. The algorithm is parallelized efficiently using Graphics Processor Unit (GPU) architecture [150]. The GPU, in contrast to the Central Processing Unit (CPU), is optimized towards parallelizable routines. Instead of a few fast processing cores (4-16, for standard CPUs), it contains thousands of slower cores. For a procedure that is highly parallelizable, a GPU can be 10-100 times faster than a CPU. For the evolution of a GA, each site is "1-1" mapped to a single GPU core. The mean field updates require only a small amount of information transfer between cores

and are thus performed efficiently.

3.3.1 Time evolution protocol

Notably, an initial optimization to the ground state of the trapped gas when $\phi \neq 0$ includes large domain walls, whose shape is highly dependent on the initial random state. To avoid these issues, we use a dynamical approach which is also used in recent experiment on SBH model by Kennedy et al. [151]. The ground state of an initial "frozen" system ($J = 0.001U$, $\phi = 0$) is found using the local variational optimization scheme (section C.2.1). Since $J \approx 0$, the gas contains only a tiny layer of superfluid surrounding the Mott insulating region in the centre. The fraction of the condensed number of particles to the of the total number of particles is $N_0/N \approx 10^{-3}$. Changing the phase does not practically modify the system in the mean field level, as the Mott insulating phase is "blind" (the gap is very large) to any flux configuration. When the phase is tuned to the desired value, the hopping amplitude is slowly increased to the desired value for the quench experiment. Finally, the trap amplitude is set to $V_0 = 0$ and the cloud expands. The protocols are performed in 3 steps.

1. State optimization. For $J = 0.001U$, $\phi = 0$, $V_0 = 0.0005U$, and $\mu = 0.4U$ or $1.4U$ the ground state is found.

2. Formation of flux configuration. ϕ is dynamically increased from 0 to π. The phase is increased linearly from $t_0 = 50$ to $t = 100$.

3. Lattice heating. The hopping parameter is slowly ramped to the desired value. The slow increase is made using a hyperbolic tangent function:

$$J = J_{init} + \frac{J_{final} - J_{init}}{2}(1 + \tanh\left(2a(t - t_1) - 2\right)), \tag{3.30}$$

   where $t_1 = 150$ and $a = 1000$, where a is the time-scale of the ramp, i.e. the ramp performed over $\Delta t = 1000$. The hyperbolic tangent function is used to have a smooth increase of hopping. It is important to use smooth variations for parameters. If the function is not smooth,

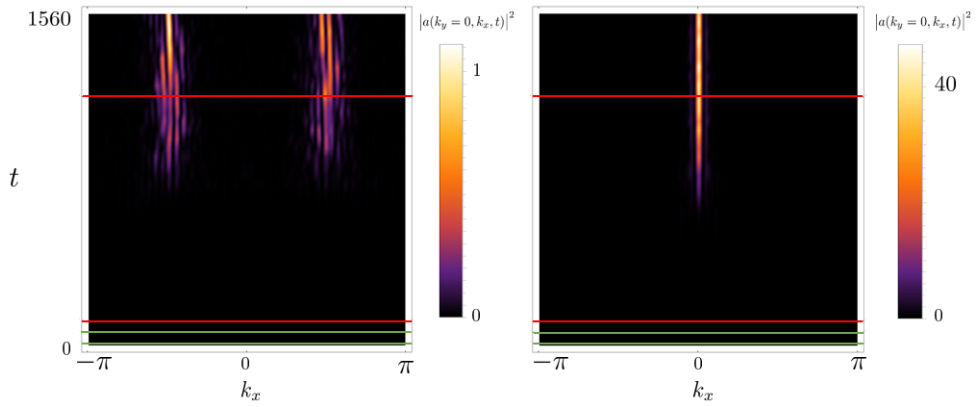


Figure 3.9: Evolution of a gas according to the described protocol, up to the trap quench. Green lines denote the time window where the phase is increased. The red lines denote the time window where the hopping elements are ramped up. *Left:* Particle fluctuations for fixed $k_y = 0$, $J_{final} = 0.045U$ and $\phi_{final} = \pi$. *Right:* Time evolution protocol of the particle fluctuations for fixed $k_y = 0$, $J_{final} = 0.07U$ and $\phi_{final} = 0$.

the delta function errors appearing when the derivative is ill-defined may destabilize the long-time evolution.

4. Trap quench. The trap is turned-off using a hyperbolic tangent function at $t_2 = 1500$. In this case, $a = 5$.

The time step is chosen to be $dt = 0.01$ and the total simulation time is $t_{total} = 3600$. To be consistent, exactly the same protocol is used when synthetic fields are not turned on. When comparing expansion dynamics, the time is normalized by the hopping parameter. In fig. 3.9 the particle fluctuations in momentum space are plotted with respect to time for a cross section $k_y = 0$. Initially, deep in the Mott insulator lobe, fluctuations are zero independently of the flux configuration. As hopping is increased, a condensate forms at $k_x = 0$ for $\phi = 0$ and $k_x = \pm\pi/2$ for $\phi = \pi$.

3.3.2 Hard-core regime: $\rho < 1$

When the density of the cloud $\rho < 1$, the expansion can be approximated by the hard-core limit where the local Hilbert space contains 0 or 1 particle states. The Hamiltonian becomes $H = -\sum_{<i,j>}(J_{i,j}\hat{a}_i^\dagger\hat{a}_j^\dagger + H.C.)$. For

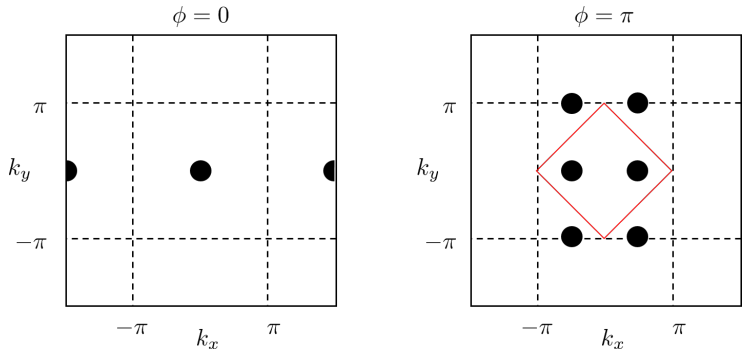


Figure 3.10: Ground state diagrams for the condensate in momentum space for $\phi = 0, \pi$. For $\phi = 0$ the gas condenses to the $\mathbf{k} = 0$ state while for $\phi = \pi$ the Brillouin zone (bounded by red lines) is twofold degenerate, with ground states at $k_x = \pm\frac{\pi}{2}$,$k_y = 0$.

$\phi = 0$, it is diagonalized by a Fourier transform and has a single particle dispersion relation

$$E_{\phi=0}(k_x, k_y) = -2J(\cos k_x + \cos k_y). \tag{3.31}$$

For $\phi \neq 0$, following the Fourier transform, an additional diagonalization of a 4×4 matrix is required:

$$-J \begin{pmatrix} 0 & \Delta(k_x) & 0 & 2\cos k_y \\ \Delta^*(k_x) & 0 & 2\cos k_y & 0 \\ 0 & 2\cos k_y & 0 & \Gamma(k_x) \\ 2\cos k_y & 0 & \Gamma^*(k_x) & 0 \end{pmatrix}, \tag{3.32}$$

where $\Delta(k_x) = e^{-ik_x} + e^{i(k_x-\phi)}$ and $\Gamma(k_x) = e^{-ik_x} + e^{i(k_x+\phi)}$. For $\phi = \pi$ the system has two bands,

$$E_{\phi=\pi}(k_x, k_y) = \pm 2J\sqrt{\cos^2 k_y + \sin^2 k_x}. \tag{3.33}$$

The ground states of eqs. (3.31) and (3.33) are illustrated in fig. 3.10. For $\phi = 0$ the cloud condenses to $\mathbf{k} = 0$, while for $\phi = \pi$ the Brillouin zone is twofold degenerate with minima at $k_x = \pm\pi/2$, $k_y = 0$.

The ballistic expansion dynamics for the hard-core BH model are the-

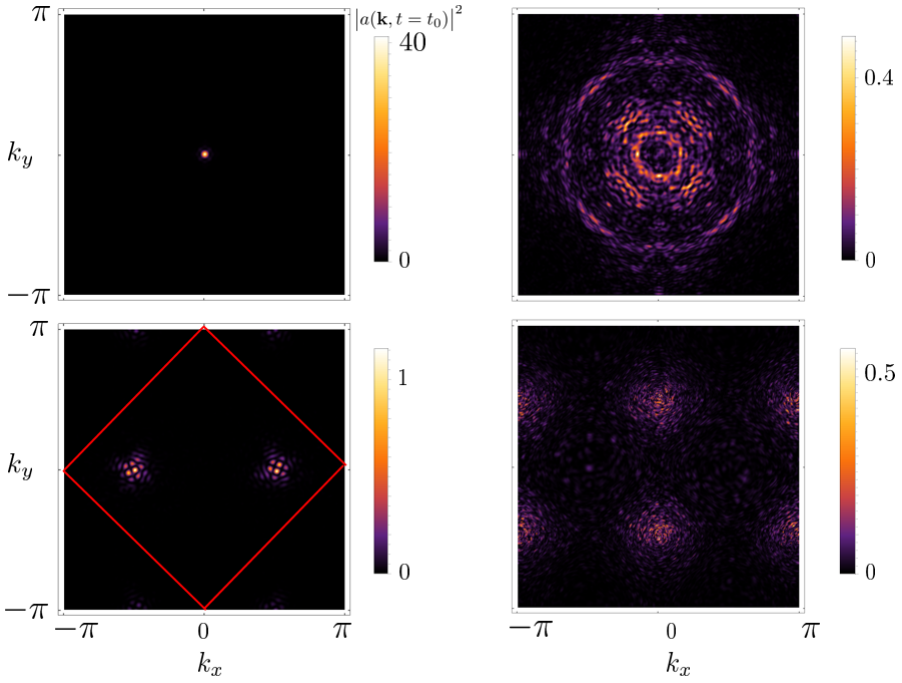


Figure 3.11: Expansion of the gas according to the described protocol in momentum space. *Left-top/bottom:* Particle fluctuations $\left|a(\mathbf{k})\right|^2$ just before the trap quench for $\phi = 0/\phi = \pi$, $J = 0.07U$, $t_0 = 0$. For, $\phi = 0$, the cloud is in a superfluid state and the fluctuations are centred around $\mathbf{k} = 0$. For $\phi = \pi$ the cloud is in the two-fold degenerate ground state $k_y = 0$, $k_x = \pm\pi/2$ (red border denotes the Brillouin zone). *Right-top:* Same diagram as left-top for $t_0 = 52(1/J)$. *Right-bottom:* Same diagram as left-bottom for $t_0 = 108(1/J)$.

oretically explained by Jreissaty et al. [146]. Experimental observations for bosons [144] and fermions [145] qualitatively agree with the theoretical predictions. We illustrate the ideas of [146] and use the same concept to understand the sub-ballistic expansion dynamics of SBH model.

$\phi = 0$. In the strongly interacting regime, $U \gg J$, the condensed number of particles is expected to be much smaller than the total number $N_0 \ll N$, or even $N_0 = 0$ if all the cloud is in the Mott insulator phase. The non-condensed part of the cloud is expected to occupy all possible momenta in the $\mathbf{k}$ space, while the condensed part will occupy $\mathbf{k} = 0$ (if $\phi = 0$). The total kinetic energy of the cloud is then $E_{kin} \approx 0$. If the whole cloud is insulating, $E_{kin} = 0$. Along the expansion, kinetic energy is conserved. Therefore, in the long time evolution the particles are expected to have

momentum $\mathbf{k}$ satisfying $E_{\phi=0}(k_x, k_y) = 0$. For eq. (3.31), this constraint corresponds to

$$k_y = \pi \pm k_x, \quad k_y = -\pi \pm k_x. \tag{3.34}$$

Such a contour is observed in the mean field expansion of the cloud in the top-right plot of fig. 3.11. The outer layer of the momentum distribution corresponds to eq. (3.34). Particles that expand according to eq. (3.34) belong to the non-condensed fraction of the gas $(N - N_0)/N \approx 0.4$. The inner slow-expanding structure of the cloud is due to the condensed fraction.

The real space expansion structure, observed in fig. 3.12 (bottom), is also understood from the described phenomenology. The group velocity $u_g(\mathbf{k}) = \nabla_{\mathbf{k}} E(\mathbf{k})$ is maximum along the contour defined by eq. (3.34) and points to the direction perpendicular to the contour. Therefore, atoms expand in a square like profile, where the edges correspond to particles with momenta according to eq. (3.34).

$\boldsymbol{\phi = \pi}$**.** Similarly to $\phi = 0$, the total kinetic energy must be approximately zero along the expansion. The cloud, therefore condenses to the modes where the dispersion relation $E_{\phi=\pi}(k_x, k_y) = 0$. For the negative band of eq. (3.31), the solutions inside the first Brillouin zone are the points:

$$k_y = \pm\frac{\pi}{2}, \quad k_x = 0. \tag{3.35}$$

The point-like solutions have a dramatic effect on the expansion of the cloud. The group velocity at the solutions are singular. Intuitively the group velocity points to a direction perpendicular to the contour. Since the contour is reduced to a point, it is impossible to define a single perpendicular vector, so the group velocity is ill-defined. This means that there is no net-motion of particles in the cloud, which corresponds to the suppression of the ballistic dynamics observed for $\phi = 0$.

The real space density of the mean field expansion dynamics is shown in fig. 3.12(top). The core of the cloud survives for much longer in the $\phi = \pi$ scenario. In addition, no net-motion of particles is visible, in contrast to $\phi = 0$, where expansion has a structured pattern. In fig. 3.11 (bottom), the long time expansion fluctuations condense around the singular modes

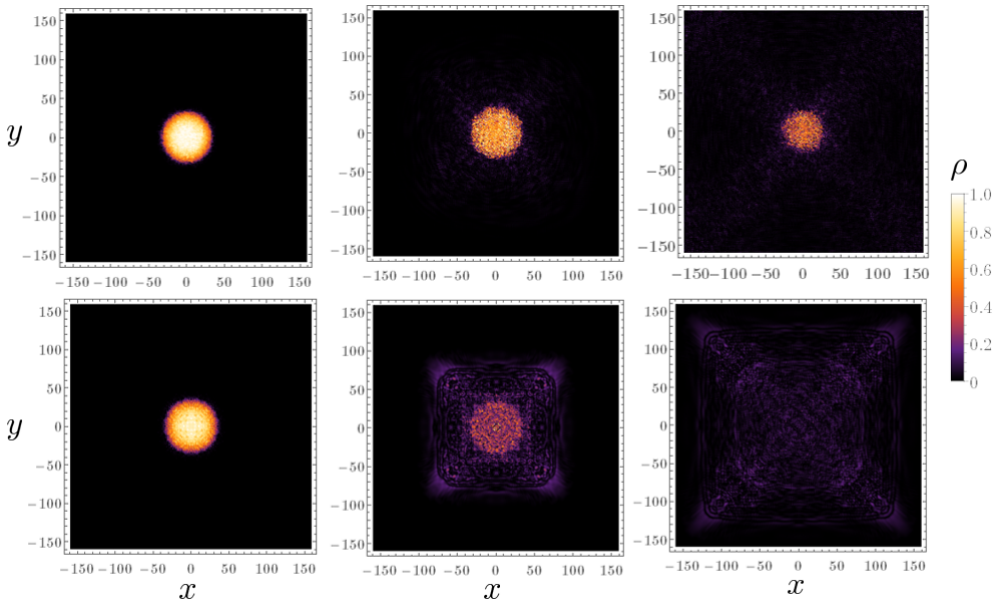


Figure 3.12: *Top:* Real space density profiles for $t = \{0, 67.2, 168\}$ and $\phi = \pi$. *Bottom:* Real space density profiles for $t = \{0, 39, 67.2\}$ and $\phi = 0$.

predicted by eq. (3.35).

To quantitatively measure self-trapping, we calculate the fraction of particles that remain within the initial radius of the trapped cloud N_R/N, as the cloud expands. The left plot of fig. 3.13 shows the behavior of N_R/N for various cases. When the flux configuration is active the number of particles that stays within the cloud core decays linearly with time $N_R = N - ct$. In addition, the hopping parameter amplitude does not affect the self-trapping in a non trivial way, i.e,. the curves for all amplitudes collapse to the same curve when the time is normalized by the amplitude. On the other hand, for $\phi = 0$, the decay of N_R is much faster than for $\phi = \pi$, however, it is hard to check if it is linear or faster than linear.

3.3.3 Soft-core regime: $\rho > 1$

Cloud expansions for $\phi = 0$, in the soft-core limit, display quantitatively and qualitatively different dynamics from the hard-core limit. In contrast to the hard-core limit, strong interactions induce a self-trapping behavior. These effects were found experimentally by K. Winkler et al. [143] and studied in various theoretical works [152, 153, 154].

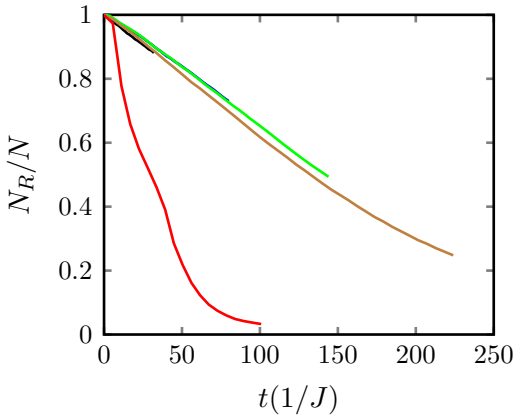


Figure 3.13: Fraction of particles remaining in the initial cloud radius with respect to the time measured from the trap quench. Expansion for $\mu = 0.4U$, $\phi = \pi$, $J = \{0.01U, 0.025U, 0.045U, 0.07U\}$ (black, blue, green, brown). The red line corresponds to $\mu = 0.4U$, $\phi = \pi$, $J = 0.07U$.

The simplest scenario is when the doping allows $0, 1, 2$ particle occupancies on each site. Consider a doublon on site i ($|2_i\rangle$). The hopping term of the Hamiltonian can cause a doublon decay to two monomers $|2_i\rangle \rightarrow |1_i\rangle |1_j\rangle$, where i, j denote neighboring sites. In addition, monomers on neighboring sites can form a doublon $|1_i\rangle |1_j\rangle \rightarrow |2_i\rangle$. The energy offset for these transitions is U, while the maximum kinetic energy in 2D for the two monomers is $8J$. Thus, for $J \ll U$, these transitions are non-resonant, and therefore, in the first order doublons do not decay and monomers undergo elastic scattering. On the other hand, given a doublon and a NN monomer, the transitions $|2_i\rangle |1_j\rangle \leftrightarrow |1_i\rangle |2_j\rangle$ are resonant, meaning that monomers act as a medium for doublons to propagate. The hopping energy associated with doublon propagation in a monomer medium is twice the energy associated with the monomer propagation in an empty medium. Doublons hop to empty lattice sites with second order perturbations, where the transition $|2_i\rangle \rightarrow |2_j\rangle$ is possible through the virtual state $|1_i\rangle |1_j\rangle$. This is a resonant process on the second order energy scale $\propto J^2/U$.

Regarding the expansion dynamics, it is clear that the time-scale for the doublons to hop to empty sites is the inverse energy scale $1/(J^2/U)$, which is much larger than the monomer case $1/J$. Since we set the chemical potential to $\mu = 1.4U$, the trapped cloud has a core which contain doublons and an outer layer $\mu - V_{trap}(i) < U$, composed of monomers. The cloud expansion

is expected to have two phases. Initially, the outer layer of monomers starts to expand similarly to the $\rho < 1$ case. However, doublons propagate twice as fast in the case that their NN is a monomer. Therefore, before all monomers escape, doublons start to reach the boundary of the cloud, trapping monomers in between doublons and thus, stopping their expansion. At that point, the second phase commences where the expansion of the cloud is dominated by the doublon hopping to empty sites.

Fig. 3.15 compares the dynamics for $\phi = 0$ and $\phi = \pi$. When the phase is zero, the outer layer of the cloud starts to expand ballistically. Doublons expand fast and density at the boundary exceeds unity. The sites that have $\rho > 1$ act as domain walls and the expansion of the cloud core is halted. The tail of the cloud, that is initially separated from the core, continues to expand ballistically. When $\phi = \pi$, the outer layer is also suppressed due to the self-trapping effect of the hard-core limit. Doublons seem to also spread much slower across the cloud than in the $\phi = 0$ case.

An interesting question is to measure which effect is stronger, namely, self-trapping due to the flux or self-trapping due to the immobile doublons. In fig. 3.14 (right), N_R/N is compared for three different cases for the same hopping $J = 0.025U$: 1) $\{\mu = 1.4U, \phi = \pi\}$, 2) $\{\mu = 1.4U, \phi = 0\}$, 3) $\{\mu = 0.4U, \phi = \pi\}$. The first and third cases seem to have a constant decay rate with different slope. In particular, doublons seem to have stronger effect to the self-trapping than the flux. The second case, initially decays faster than the third case indicating a brief ballistic expansion for the outer layer of the cloud. However, the core expands slower than the hard-core case. At the long time limit it is possible that the first and second cases expand with the same rate. Therefore, flux induced self-trapping is weaker than doublon induced self-trapping.

3.3.4 Discussion

We considered cloud expansions of strongly interacting bosons in optical lattices with synthetic fields. By carefully choosing the fields, the cloud can be self-trapped. For expansions at low occupancy, $\rho < 1$, we showed using time-dependent GA, that the typical ballistic dynamics of the BH

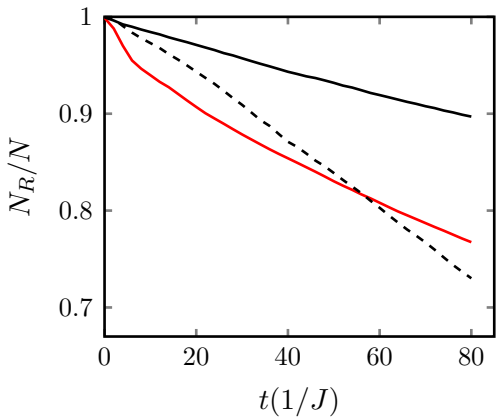


Figure 3.14: Fraction of particles remaining in the initial cloud radius with respect to the time measured from the trap quench. Expansion for $\mu = 1.4U$, $\phi = \pi$ (black) and $\phi = 0$ (red) for $J = 0.025U$. The dashed line corresponds to $\mu = 0.4U$, $\phi = \pi$, $J = 0.025U$.

model [155, 140, 144, 156] are suppressed by the condensation on singular modes appearing in the dispersion relation when $\phi = \pi$. Similar incoherent self-trapping was found by A. R. Kolovsky [157] in the discretized Gross-Pitaevskii limit, in a lattice with similar fluxes.

Expansions of soft-core clouds, $\rho > 1$, demonstrate self-trapping effects due to immobile doublon formations [152, 153, 154]. When synthetic fields are turned on the clouds are self-trapped by two different mechanisms. We found that at least in the mean-field limit, the doublon mechanism is dominant.

It will be interesting to repeat similar experiments using more quantitative methods as tDMRG [40]. To reproduce a similar field it is enough to just use a 3-legged ladder.

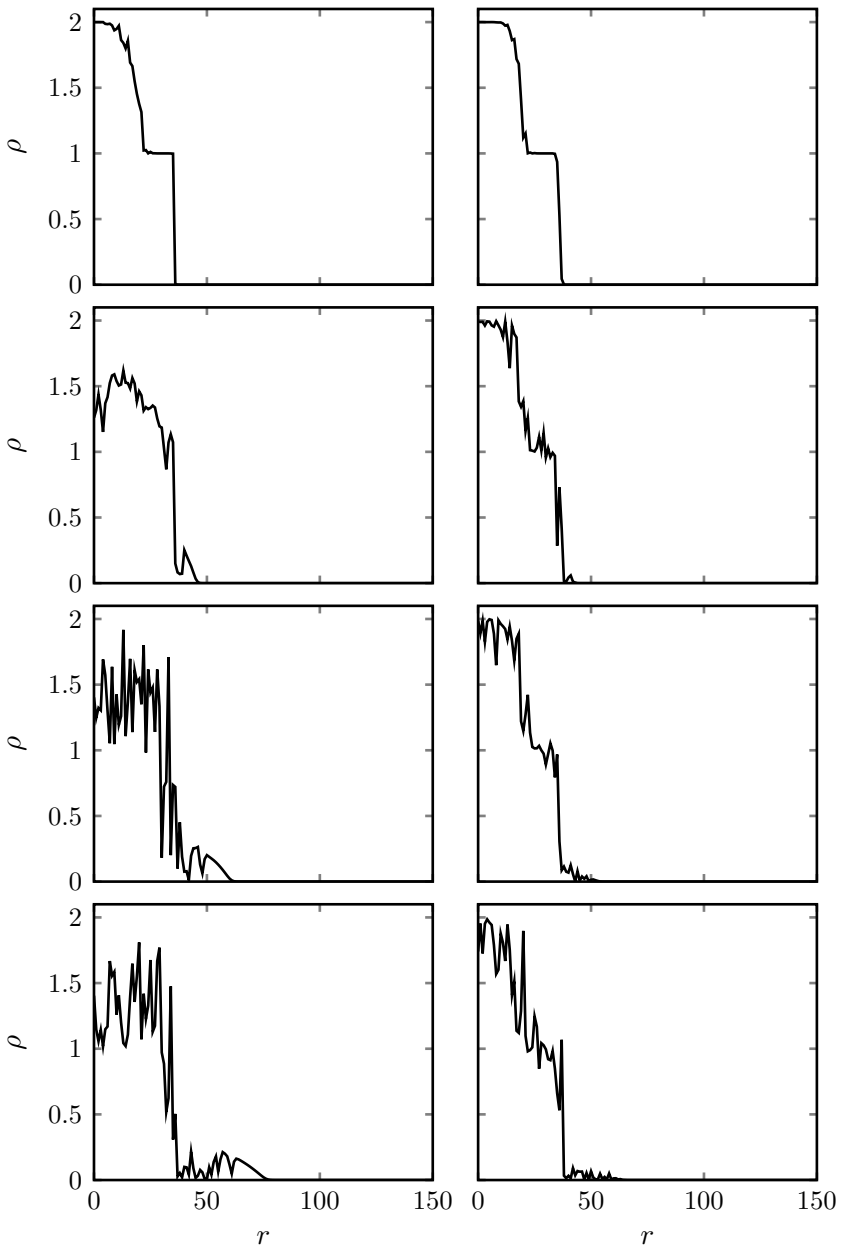


Figure 3.15: Local density diagrams of the expanding cloud across the cross section $x = y$, for $t = \{0, 8, 12, 16\}(1/J)$. The parameters are $J = 0.025U$, $\mu = 1.4U$ and phases $\phi = 0$ (left) and $\phi = \pi$ (right).

Outline

4.1 Summary

In this thesis we developed and applied numerical techniques on strongly correlated quantum systems.

Tensor-Networks

The first chapter reviews the formalism of a particular class of tensor network states, namely MPS and PEPS. We show how MPS can efficiently approximate 1D quantum states which feature the area-law property for entanglement entropy. In addition, the celebrated DMRG algorithm [21] is presented. DMRG is used to efficiently approximate (by MPS) the ground states of quantum Hamiltonians that admit an MPO representation. For $D > 1$, the area-law states cannot be approximated by MPS. The ansatz that can capture area-law in higher dimensions is known as PEPS [158]. We reviewed PEPS and a simple optimization scheme for ground states, based on imaginary time evolution and the well known iTEBD method [3, 57]. The calculation of local correlation functions is non-trivial in the PEPS formalism. We illustrate a lattice renormalization scheme (TRG) [4] which can by used to efficiently calculate nearest neighbour correlation functions.

Many-body localization and eDMRG

In the second chapter we focus on quantum systems which are in MBL phase. The MBL phase implies that every eigenvector of the Hamiltonian

features an area-law. This is in contrast to the typical quantum systems where area-law is only a feature of the low-energy spectrum. MBL systems are introduced through the phenomenological LIOM formalism [81]. To target eigenstates in the middle of the spectrum we develop a eDMRG algorithm which is a generalization of the DMRG algorithm that can target states everywhere in the spectrum [20]. This algorithm is not limited to MBL systems as it can be used to target area-law eigenstates of any Hamiltonian. Site-disordered XXZ chain is used to validate eDMRG algorithm and predict various properties of MBL eigenstates for much larger systems. In addition, the LIOM formalism is used to predict the power-law structure of the eigenvalues of the reduced density matrix along a bipartition of the system for all MBL eigenstates [20]. The results are backed up by eDMRG and ED simulations.

Strongly interacting bosons in 2D

In the last chapter we reviewed the ground state physics of Bose-Hubbard and Extended Bose-Hubbard models. The iPEPS ansatz is used to accurately approximate the ground state on the Honeycomb lattice providing accurate phase diagrams of the models. We compared the results with GA and published QMC studies [104, 103]. In the second part of the last chapter we studied the expansion dynamics of the strongly interacting Harper-Hofstadter Hamiltonian using GA ansatz. By comparing with Bose-Hubbard model we observed that expansion dynamics become massively slower in the presence of the flux.

4.2 Future Work

The writer is interested in understanding the MBL transition deeper. Is it a phenomenon that only appears in disordered or quasi-periodic 1D systems [159]? Can translation invariant systems generate a self-disordered environment that may allow for an MBL phase [160, 161, 162]? Is MBL allowed in higher dimensions or does the structure of the density of states eventually restores ergodicity [163, 78]? Such questions although simple to express

are rather challenging to approach either analytically or numerically. We believe that the eDMRG algorithm and a possible extension to an ePEPS algorithm could help to shed light in some of these questions.

Appendix A

Reduced-Rank-Randomized Singular Value Decomposition

The bottleneck of SU optimization is the SVD step which scales as $O((d\chi^{z-1})^3)$. Furthermore, in TRG/SRG algorithms a considerable amount of time is spent on SVD which scales as $O((\chi^4)^3)$. In both cases, a severe truncation takes place $d\chi^{z-1} \to \chi$ and $\chi^4 \to \chi^2$. Since the truncated rank is much smaller than the dimensionality of the matrix, we can use an approximate algorithm for the SVD. This is conceptually similar to arnoldi/lanczos methods which are used when only a small part of the spectrum of a matrix is needed.

We use a SVD variant called Reduced-Rank-Randomized SVD (RRSVD) first introduced by Halko et al. [58] and later used for 1D quantum systems [164]. The method and it's applicability to PEPS algorithms is briefly illustrated.

For simplicity, a square matrix A of dimension m by m is used. We aim for a rank(n) approximation of A, where $m \gg n$. First, we construct an orthogonal matrix Q of dimension n by m. The columns of Q form an approximate basis of the requested rank for the matrix A. Then $X = \text{SVD}(Q^\dagger QA)$ provides an approximate singular value spectrum up to rank n. An optimal answer (the answer we get when the exact SVD is truncated)

bounds the error as

$$\begin{aligned} \min_{\text{rank}(X)=n} \|A - X\|_F &= \sqrt{\sum_{i>n}^{m} \lambda_i^2}, \\ \min_{\text{rank}(X)=n} \|A - X\|_2 &= \lambda_{n+1}, \end{aligned} \tag{A.1}$$

where λ_i are the singular values of A. The error in terms of two different kind of norms is presented. The Frobenius norm is more common in physical applications, while the general error estimate of the proposed algorithm is proved for the spectral norm.

To determine a basis Q, a random Gaussian matrix Ω is generated, with dimensions $m \times n + r$. An additional r vectors are used as oversampling to the rank(n) approximation. The product of the matrix to the random vectors is taken and a QR decomposition is used to form an orthonormal basis Q,

$$\begin{aligned} Y &= A\Omega \\ \{Q, R\} &= \text{QRDecomposition}(Y). \end{aligned} \tag{A.2}$$

Instead of using Q to approximate the singular value spectrum, we construct a power-iteration step to further increase convergence, using the trivial fact that the singular values of $(AA^\dagger)^q A$ are λ_i^{2q+1}. So, instead of $Y = A\Omega$ we compute $Y = (AA^\dagger)^q A\Omega$. After calculating eq. (A.2) we loop q times

$$\begin{aligned} \text{For } 1 \leq j \leq q& \\ Y &= A^\dagger Q_j \\ \{\tilde{Q}_j, R\} &= \text{QRDecomposition}(Y) \\ Y &= A\tilde{Q}_j \\ \{Q_j, R\} &= \text{QRDecomposition}(Y) \end{aligned} \tag{A.3}$$

and extract the final Q_q. The SVD of matrix A is approximated as

$$\begin{aligned} \tilde{U}SV^\dagger &= \text{SVD}(Q_q^\dagger A), \\ U &= Q_q \tilde{U}. \end{aligned} \tag{A.4}$$

Given $n + r < m$ the full SVD in eq. (A.4) has asymptotic complexity $O((n + r)^2 m)$. The bottleneck of the whole computation are the $2q + 1$ matrix-matrix multiplications. Thus, the overall algorithm has asymptotic complexity $O((2q + 1)(r + n)m^2)$.

Given an oversampling parameter $r \geq 2$ and a target rank $n \geq 2$, the average spectral error for the power-method scheme is proved in [58] to be

$$\mathbb{E}\left\|A - Q_q^\dagger Q_q A\right\|_2 \leq \left\{(1 + \sqrt{\frac{n}{r-1}})\lambda_{n+1}^{2q+1} + \frac{e\sqrt{n+r}}{r}(\sum_{i>n}\lambda_i^{2(2q+1)})^{1/2}\right\}^{\frac{1}{2q+1}}. \tag{A.5}$$

A more convenient bound can be drawn by assuming that for $i > n$, $\lambda_i = \lambda_{n+1}$. This reduces eq. (A.5) to

$$\mathbb{E}\left\|A - Q_q^\dagger Q_q A\right\|_2 \leq \left\{1 + \sqrt{\frac{n}{r-1}} + \frac{e\sqrt{n+r}}{r}\sqrt{m-n}\right\}^{\frac{1}{2q+1}} \lambda_{n+1}. \tag{A.6}$$

It is clear that the power-iteration scheme offers an exponential rate of convergence to the optimal spectral norm eq. (A.1). In terms of the Frobenius norm, it is not possible to derive similar bounds. However, it is expected that if the singular values decay "fast" the spectral norm and Frobenius norm are approximately equal. If the singular values are bound by a power-law with exponent at least -1, RRSVD provides an efficient algorithm to solve problems with severe rank truncation [164].

In fig. A.1 we illustrate the speedup on the SU algorithm applied to the Extended Bose-Hubbard model on a Honeycomb lattice. The model parameters are $J = 1$, $U = 15J$, $V = J/0.3$, $\mu = 0.7U$, which correspond to a cloud in the superfluid phase. Rank χ oversampling and $q = 2$ power iterations are used. In the Honeycomb lattice we expect the ratio of execution times for SVD and RRSVD to increase linearly $O((d\chi^2)^3/(\chi(d\chi^2)^2)) \propto (\chi)$. The simulations were performed using Mathematica software. The CPU is a 4-core I7 HQ5700 @ 2.7Ghz. 8-MKL threads are used for the simulations. For small bond dimension, various overheads on the RRSVD algorithm reduce the speedup. Beyond $\chi = 15$, the expected linear increase is observed. For all singular values, the errors are very small, $\frac{|\lambda_{SVD} - \lambda_{RRSVD}|}{\lambda_{SVD}} < 10^{-3}$.

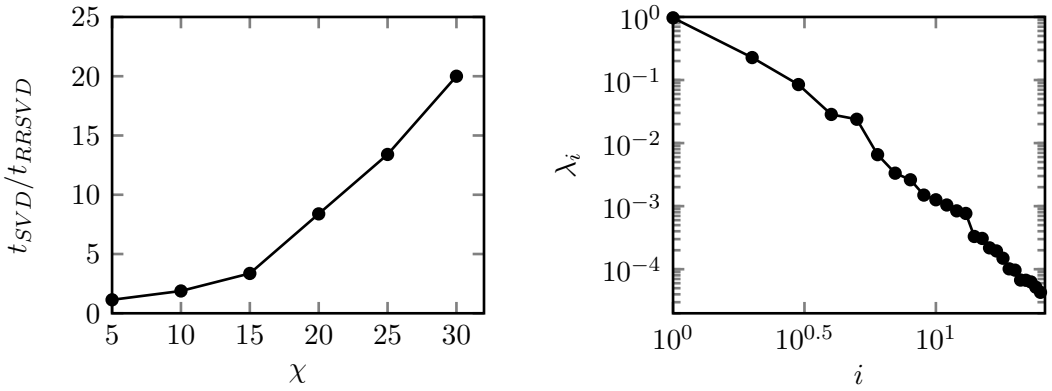


Figure A.1: *Left*: Speedup of the RRSVD algorithm over the standard SVD version with respect to the bond dimension χ in a Honeycomb lattice. The averaged time step over a few hundents of iterations is used. *Right*: The singular value spectrum where RRSVD is applied. The fast power-law decay ensures the accuracy of the algorithm.

Appendix B

Shift-invert algorithm

In this appendix we illustrate the shift-invert method for the local updates of the eDMRG algorithm presented in section 2.2. We are mainly interested in diagonalizing Hamiltonians, so Hermitian matrices will be assumed, however the algorithm can be straightforwardly generalized to apply to non-Hermitian matrices. In order to study the eigenstates of quantum systems, a Hermitian matrix H of dimensions $m \times m$ is diagonalized. The cost of the diagonalization is of order $O(m^3)$. The scaling of the full Hilbert space increases exponentially with respect to the size of the systems. For example, for 1D systems $m = d^L$, where d is the local Hilbert space dimension. Therefore only the spectrum of very small systems can be found. In DMRG algorithms the exact diagonalization of each local iteration scales as χ^6. Since, χ dictates the maximum amount of correlations which can fit into a MPS, resorting the exact diagonalization limits the algorithm to very slightly correlated systems.

Power Method. The scaling is improved, if the target is the ground state energy of the system (the largest in magnitude eigenvalue of H). Instead of a diagonalization, the ground state can be found using only matrix-vector multiplications which cost $O(m^2)$. For simplicity, we can assume that the ground state is non-degenerate. The initial state $|\psi_{init}\rangle = c_0 |\psi_0\rangle + c_1 |\psi_1\rangle + \ldots$ has finite overlap c_0 to the ground state, c_1 to the first excited state .... The normalized state after N matrix-vector multiplications is

Algorithm 1 Power-Method

1: Input vector $|\psi_0\rangle$, matrix M and number of iterations N_{power}
2: **for** $n = 1$ `to` $n = N_{PM}$ **do**
3: $\quad |\psi_n\rangle \leftarrow M\,|\psi_{n-1}\rangle$
4: $\quad |\psi_n\rangle \leftarrow \frac{|\psi_n\rangle}{\||\psi_n\rangle\|}$
5: **end for**

$$\begin{aligned}\frac{H^N\,|\psi_{init}\rangle}{\left\|H^N\,|\psi_{init}\rangle\right\|} &= \frac{E_0^N c_0\,|\psi_0\rangle + E_1^N c_1\,|\psi_1\rangle + \dots}{\sqrt{E_0^{2N}|c_0|^2 + E_1^{2N}|c_1|^2 + \dots}} \\ &\approx \frac{\frac{c_o}{|c_0|}\,|\psi_0\rangle + \Delta^N \frac{c_1}{|c_0|}\,|\psi_1\rangle}{\sqrt{1+\Delta^{2N}\left|\frac{c1}{c_0}\right|^2}} \approx e^{i\theta}\,|\psi_0\rangle + O(\Delta^N), |\psi_1\rangle\end{aligned} \tag{B.1}$$

where we have neglected all states which have smaller eigenvalues than $|\psi_1\rangle$. The global phase is $e^{i\theta} = \frac{c_o}{|c_0|}$ and $\Delta = \frac{E_1}{E_0}$. The energy converges to the ground state as

$$\langle H\rangle = \frac{E_0 + \Delta^{2N}\left|\frac{c1}{c_0}\right|^2 E_1}{1+\Delta^{2N}\left|\frac{c1}{c_0}\right|^2}. \tag{B.2}$$

Convergence to the ground state is thus geometric, with ratio $|\Delta| < 1$. Only a few iterations are usually enough to achieve an accurate approximation to the ground state when the gap $|E_0 - E_1|$ is finite. The power method is a simple method, rarely used in state-of-the-art algorithms. More sophisticated Krylov Subspace Iteration methods [31] are chosen since they are more accurate and can target a small part of the spectrum around the ground state. However, MPS optimization algorithms already have a layer of complexity regarding their iterative local variational nature. Usage of a simple power method makes the algorithm easier to control and more flexible.

Shift-Invert scheme. The power method described previously is only useful in order to target the ground state of a matrix. To go beyond the ground state and be able to target any eigenstate, matrix H must be modified to a new matrix whose ground state will be the targeted eigenstate of H.

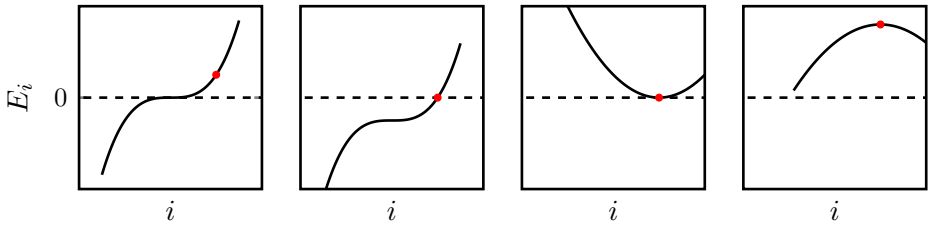


Figure B.1: *From Left to Right*: A schematic of the shift-square-invert opearation. The x axis labels the spectrum $\{E_i\}$ of the matrix and y axis shows the magnitude of each eigenvalue. We have chosen the centre of the band to be at $E = 0$ and have the highest spectral density. The targeted energy is the red mark. The shift operation transforms the spectrum in order for the eigenvalue closer to the target to have the smallest magnitude. The square operation makes the spectrum positive-definite. The inversion of the spectrum transforms the targeted eigenvalue to have the largest magnitude. The closer the target energy to the eigenvalue, the steeper the last plot.

The first step to construct the new matrix is to shift the initial matrix by the target energy $\tilde{H} = H - \lambda I$. The eigenstate of H with eigenvalue closest to λ is the eigenstate of $\tilde{H}$ with eigenvalue closest to 0. The second step consists of inverting $\tilde{H}$ in order to transform the smallest magnitude eigenvalue to the largest magnitude eigenvalue of the inverse matrix. The power method using $\tilde{H}^{-1}$, has a convergence rate

$$|\Delta| = \left| \frac{\frac{1}{E_1 - \lambda}}{\frac{1}{E_0 - \lambda}} \right| = \left| \frac{E_0 - \lambda}{E_1 - \lambda} \right|, \tag{B.3}$$

where E_0, E_1 are the closest in magnitude eigenvalues to λ. It is important to note that in quantum systems the spectral density around the middle of the spectrum scales exponentially with respect to the system size $\rho(E) \propto e^L$. Even though the gap $|E_0 - E_1| \approx e^{-L}$, the ratio $|\Delta| \ll 1$, if the magnitude of the energy shift is the same as that of the eigenvalues. In the limit of $E_0 \to \lambda$ the ratio $|\Delta| \to 0$ provides "instantaneous" convergence to the targeted state.

We showed how to use Shift-Invert with a power method to obtain eigenstates anywhere in the spectrum. However, the cost of inverting the matrix is $O(m^3)$. This scaling is higher than the typical power method scaling of $O(m^2)$. The cost is reduced if for each power iteration $|\psi_{n+1}\rangle = \tilde{H}^{-1} |\psi_n\rangle$

we solve the linear system $|\psi_n\rangle = \tilde{H}\,|\psi_{n+1}\rangle$. The linear system can be efficiently solved using iterative algorithms. For eDMRG, a conjugate gradient algorithm is used.

Conjugate gradient algorithm. Various versions of conjugate gradient algorithms exist, see [165]. The conjugate gradient algorithm converges only when the matrix M of the linear system of equations, is Hermitian and sign-definite. If the matrix is not Hermitian or sign-definite the conjugate gradient algorithm can be applied to the normal equations $M^\dagger M\,|\psi_{n+1}\rangle = M^\dagger\,|\psi_n\rangle$, since $M^\dagger M$ always satisfies these constraints. The shifted Hamiltonian is Hermitian by default, however, it is not sign-definite. If the Hamiltonian is not symmetric under $\tilde{H} \to -\tilde{H}$, instead of the normal equations it is equivalent to solve:

$$\tilde{H}^\dagger \tilde{H}\,|\psi_{n+1}\rangle = |\psi_n\rangle\,. \tag{B.4}$$

Algorithm 2 is the algorithm used to solve the linear system of eq. (B.4) and corresponds to one iteration of the power method. This is the standard CG algorithm with conjugation parameter β calculated using Polak-Ribière formula [166]. This formula was chosen after testing various common formulas, as it provides better convergence rate in the eDMRG algorithm. The cost of inversion using N_{CG} iterations scales as $O(N_{CG}m^2)$.

To sum up, we have presented an iterative shift-invert method to target arbitrary eigenstates of a matrix H. The cost of the method is of the order of $O(N_{CG}N_{power}m^2)$, where N_{power} is the number of power method iterations. For large matrices this cost is significantly smaller than the $O(m^3)$ cost of exact diagonalization. For the local update of eDMRG the effective Hamiltonian has a dimension $m = (d\chi)^2$, where $\chi = 100 - 1000$. However, the matrix-vector multiplication can be performed in $O(\chi)^3$ steps (fig. 1.5). The acceleration provided by the CG algorithm is $\approx \chi^3/(N_{CG}N_{power})$. For the typical values used in the numerical applications, $N_{CG} = 100 - 500$ and $N_{power} = 1$ a speedup of $10^4 - 10^5$ times is achieved.

Algorithm 2 Conjugate Gradient Method (Polak-Ribière)

Initialize vector $|x_0\rangle$, cutoff and number of iterations N_{CG}
$|R_0\rangle \leftarrow |\psi_n\rangle - \tilde{H}^2 |x_0\rangle$ ▷ residual vector
$|P_0\rangle \leftarrow |R_0\rangle$ ▷ direction of descend
for $i = 0$ `to` $i = N_{CG}$ **do**
    $|\text{temp}\rangle \leftarrow \tilde{H}^2 |P_i\rangle$
    if $\left|\langle P_i|temp\rangle\right| <$ cutoff **then**
        $|\psi_{n+1}\rangle \leftarrow \frac{|x_i\rangle}{\||x_i\rangle\|}$
        break
    else
        $\alpha_i \leftarrow \frac{\langle R_i|R_i\rangle}{\langle P_i|temp\rangle}$
        $|x_{i+1}\rangle \leftarrow |x_i\rangle + \alpha_i |P_i\rangle$
        $|R_{i+1}\rangle \leftarrow |R_i\rangle - \alpha_i |temp\rangle$
        $\beta_i \leftarrow \max\{\frac{\langle R_{i+1}|(|R_{i+1}\rangle - |R_i\rangle)}{\langle R_i|R_i\rangle}, 0\}$
        $|P_{i+1}\rangle \leftarrow |R_{i+1}\rangle + \beta_i |P_i\rangle$
    end if
end for
$|\psi_{n+1}\rangle \leftarrow \frac{|x_N\rangle}{\||x_N\rangle\|}$ ▷ power method normalization

Appendix C

Gutzwiller ansatz and Mean Field theory

In this appendix we illustrate the mean field and GA approximations to the Bose-Hubbard model used in chapter 3. First we illustrate mean field theory and find the MI-SF boundary using Landau's paradigm. We then describe GA and the algorithms used in section 3.3: A variational scheme to obtain the ground state using GA (section C.2.1) and a variational solution to the Schroedinger equation which is used for real-time evolution (section C.2.2). Finally, in section C.2.3, we illustrate the effects of parabolic traps on Bose-Hubbard model.

C.1 Mean field theory

To diagonalize Bose-Hubbard model

$$H_{BH} = -\sum_{<i,j>} J_{ij}\hat{a}_i^\dagger \hat{a}_j + \frac{U}{2}\sum_i \hat{n}_i(\hat{n}_i - 1) - \mu \sum_i \hat{n}_i \tag{C.1}$$

in the strongly interacting case $J \ll U$, it is possible to approximate the off-diagonal term of the Hamiltonian using

$$\hat{a}_j = \langle \hat{a}_j \rangle + \delta \hat{a}_j, \tag{C.2}$$

where the second term denotes fluctuations around the expectation value of the operator. The self-consistent mean field approximation was introduced in [128] and consists of substituting eq. (C.2) to the tunnelling term and keeping up to the first order in δ. To make the approach self-consistent, the fluctuation term is then substituted by $\hat{a}_j - \langle \hat{a}_j \rangle$. The resulting approximation is the decoupling of operators in the tunneling term as:

$$\hat{a}_i^\dagger \hat{a}_j = \langle \hat{a}_i^\dagger \rangle \, \hat{a}_j + \hat{a}_i^\dagger \, \langle \hat{a}_j \rangle - \langle \hat{a}_i^\dagger \rangle \, \langle \hat{a}_j \rangle \, . \tag{C.3}$$

Substituting eq. (C.3) to eq. (C.1) leads to the following MF Hamiltonian:

$$\begin{aligned} H_{MF} &= \sum_i H_{MF}^{[i]}, \\ H_{MF}^{[i]} &= -\sum_j J_{ij} \{ \hat{a}_i^\dagger \, \langle \hat{a}_j \rangle + \langle \hat{a}_i^\dagger \rangle \, \hat{a}_j - \mathrm{Re}(\langle \hat{a}_i^\dagger \rangle \, \langle \hat{a}_j \rangle) \} + H_{loc}^{[i]} \\ &= -\hat{a}_i^\dagger \Phi_i - \hat{a}_i \Phi_i^* + C_i + H_{loc}^{[i]} \\ &= H_{MF,hop}^{[i]} + C_i + H_{loc}^{[i]} \end{aligned} \tag{C.4}$$

where $\Phi_i = \sum_j J_{ij} \, \langle \hat{a}_j \rangle$ and $C_i = \sum_j J_{ij} \, \mathrm{Re}(\langle \hat{a}_i^\dagger \rangle \, \langle \hat{a}_j \rangle)\}$ is a real number. We denote the local mean fields as $\phi_i = \langle \hat{a}_i \rangle$. It is obvious that H_{MF} breaks $U(1)$ symmetry if $\Phi_i \neq 0$, since it does not commute with the total particle number operator $\hat{N}$. This feature allows H_{MF} to capture both superfluid and insulating phases. Furthermore, H_{MF} is a direct sum of local Hamiltonians $H_{MF}^{[i]}$[1], where non-local effects are approximated self-consistently by the complex field Φ_i.

C.1.1 Mott Insulator-Superfluid boundary

The boundary of the MI-SF transition can be calculated analytically using mean fields. For simplicity, we can assume a homogeneous system ($J_{ij} = J$, $\phi_i = \phi$,$n_i = n$) and a real-valued Hamiltonian. The phase boundary can be approached by Landau procedure: calculate the energy using second order perturbation theory, $E = \text{const.} + m^2 |\phi|^2 + \ldots$. The phase boundary corresponds to a determination of the zero crossing of the second order mass

[1] Within this context, local denotes the locality of the quantum (or operator) part.

term m. Using eq. (C.4) the second order expansion at site i can be formed as:

$$\begin{aligned} E_n^2 &= E_n^0 + \sum_{k \neq n} \frac{\left| \langle k | \, H_{MF,hop}^{[i]} \, | n \rangle \right|^2}{E_n^0 - E_k^0} \\ &= H_{loc}^{[i]} + Jz|\phi|^2 + (Jz|\phi|)^2 \left(\frac{n}{U(n-1) - \mu} + \frac{n+1}{\mu - Un} \right) \\ \Rightarrow m^2 &= Jz \left\{ 1 + Jz \left(\frac{n}{U(n-1) - \mu} + \frac{n+1}{\mu - Un} \right) \right\}, \end{aligned} \tag{C.5}$$

where $\{n\}$ denotes the local Fock basis. The zeroth order energy is $E_n^0 = \frac{U}{2} n(n-1) - \mu n + Jz|\phi|^2$. The phase boundary corresponds to

$$1 + Jz \left(\frac{n}{U(n-1) - \mu} + \frac{n+1}{\mu - Un} \right) = 0. \tag{C.6}$$

C.2 Gutzwiller ansatz

In many cases, for example conducting time evolution in the Schroedinger picture, it is convenient to work with an ansatz for the states instead of approximating the Hamiltonian. Instead substituting non-local terms in the Hamiltonian with mean fields, the eigenstates are taken to be factorized. This is known as Gutzwiller ansatz and is simply an ansatz of product states,

$$|\psi\rangle_{GA} = \prod_i \sum_{n_i}^{n_{max}} f_{n_i}^{[i]} \, |n_i\rangle \, , \tag{C.7}$$

where the product extends over all the sites and the sum is taken up to some cutoff value n_{max}. The total Hilbert space dimension scales linearly with respect to the size of the system Vn_{max}, V being the number of sites. This scaling is the same as that of a PEPS with bond dimension $\chi = 1$. Actually, GA is the trivial member of the PEPS family. The basic disadvantage of GA is that it does not capture non-local quantum fluctuations (non-local entanglement). However, the simple and cost efficient optimization algorithms based on GA, provide a flexible scheme that can qualitatively capture the ground state physics. The main advantage is the linear scaling with respect to the systems size for any dimension. This allows for simulations of large

systems which would otherwise be inaccessible.

Expectation values can be straightforwardly calculated using eq. (C.7). In particular, for some commonly used correlation functions we get:

$$\begin{aligned}
\langle \hat{n}_i \rangle_{GA} &= \sum_{n_i=0}^{n_{max}} \left| f_{n_i}^{[i]} \right|^2 n_i, \\
\phi_i = \langle \hat{a}_i \rangle_{GA} &= \sum_{n_i=0}^{n_{max}} f_{n_i}^{[i]*} f_{n_i+1}^{[i]} \sqrt{n_i+1}, \\
\langle \hat{a}_i^\dagger \hat{a}_j \rangle_{GA} &= \sum_{n_i=0}^{n_{max}} f_{n_i+1}^{[i]*} f_{n_i}^{[i]} \sqrt{n_i+1} \sum_{n_j=0}^{n_{max}} f_{n_j}^{[j]*} f_{n_j+1}^{[j]} \sqrt{n_j+1} = \langle \hat{a}_i^\dagger \rangle_{GA} \langle \hat{a}_j \rangle_{GA},
\end{aligned} \tag{C.8}$$

where the non-local correlations correspond to the disconnected part of the correlation function. The total number of particles is

$$N = \sum_{i}^{n_{max}} n_i, \tag{C.9}$$

and the number of particles in the condensate

$$N_0 = \sum_{i}^{n_{max}} |\phi_i|^2 . \tag{C.10}$$

C.2.1 Ground state optimization

A variational method is used to optimize the Gutzwiller state. The variational approach presented below can be used both for real and complex vectors. However, complex vector calculus is not a trivial extension of the real vector calculus. For a detailed analysis we refer to the pedagogical preprint [167]. The important property is: Complex gradient and cogradient operators $\nabla_{|\psi\rangle}$ and $\nabla_{\langle\psi|}$ are partial derivative operators. Note that the variational optimization scheme derived in this section is equivalent to the DMRG algorithm when the MPS has bond dimension $\chi = 1$. In that case the gauge of the MPS as well as the effective Hamiltonian become trivial. The Hamiltonian optimization corresponds to the optimization of the

quadratic form:

$$\begin{aligned} &\mathrm{Min}\left(\frac{\langle\psi_{GA}|\, H\,|\psi_{GA}\rangle}{\langle\psi_{GA}|\psi_{GA}\rangle}\right) \\ &= \mathrm{Min}\big(\,\langle\psi_{GA}|\, H\,|\psi_{GA}\rangle - \lambda\,\langle\psi_{GA}|\psi_{GA}\rangle\,\big), \end{aligned} \tag{C.11}$$

where a Lagrange multiplier λ has been used. The quadratic form can be optimized locally by requesting the action of the gradient with respect to the local state $|\psi_i\rangle$ to vanish. This is possible, since the GA state is factorized, $|\psi_{GA}\rangle = \prod_i |\psi_i\rangle$. It is also useful to rewrite the Bose-Hubbard Hamiltonian as

$$\begin{aligned} &H = H^{[i]} + H_{rest}, \\ &H^{[i]} = \sum_{<j>_i} (J_{ij}\hat{a}_i^\dagger \hat{a}_j + H.C.) + \frac{U}{2}\sum_i \hat{n}_i(\hat{n}_i - 1) - \mu\sum_i \hat{n}_i, \end{aligned} \tag{C.12}$$

where $< j >_i$ denotes all NN j of site i. The optimization step can now be straightforwardly derived as

$$\begin{aligned} &\frac{\partial}{\partial\,\langle\psi_i|}\big(\,\langle\psi_{GA}|\, H\,|\psi_{GA}\rangle - \lambda\,\langle\psi_{GA}|\psi_{GA}\rangle\,\big) = 0 \\ &\Rightarrow \Big(\prod_{<j>_i}\langle\psi_j|\, H^{[i]} \prod_{<l>_i}|\psi_l\rangle - \lambda\Big)\,|\psi_i\rangle = 0 \\ &\Rightarrow H^{[i]}_{MF}\,|\psi_i\rangle = \lambda\,|\psi_i\rangle\,. \end{aligned} \tag{C.13}$$

The local states are assumed to be orthonormal $\langle\psi_j|\psi_i\rangle = \delta_{i,j}$ and eq. (C.8) is used. As it turns out, local optimization just requires a diagonalization of the local MF Hamiltonian eq. (C.4). A simple recipe for the numerical scheme is presented below.

1. Generate random real (or complex if necessary) numbers for the mean fields ϕ_i for all sites i.

2. Diagonalize the local Hamiltonian $H_{MF}^{[i]}$ for all sites i.

3. Find the normalized ground state of each $H_{MF}^{[i]}$, $|\psi_i\rangle$.

4. Using eq. (C.7), calculate the new mean fields $\phi_i = \langle a_i \rangle_{GA}$.

5. Repeat steps 2-5, until the energy of the system converges sufficiently. Alternatively, convergence of the total superfluid order parameter N_0 and density N can be used. Typically, even for systems composed of $O(10^5)$ lattice sites, < 100 iterations are enough.

This approach works for the standard Bose-Hubbard model, as well as for modified versions where the tunnelling terms in the Hamiltonian are complex. The optimization of complex states usually requires more iterations. Each iteration can either be processed serially (site by site) or in parallel.

C.2.2 Time-Dependent Gutzwiller Ansatz

The Time Dependent Variational Principle (TDVP) can be solved efficiently using GA formalism [147, 148]. Solutions of TDVP using GA wavefunctions are only qualitative approximations of the exact state evolution. A rigorous proof of the solution starting from the definition of the TDVP. is presented:

$$\begin{aligned} &\mathrm{Min}\left(\langle \psi_{GA}| \, i\hbar \frac{d}{dt} - H \, |\psi_{GA}\rangle \right) \\ &= \mathrm{Min}\left(\prod_j \langle \psi_j| \, i\hbar \frac{d(\prod_i |\psi_i\rangle)}{dt} - \prod_j \langle \psi_j| \, H \prod_i |\psi_i\rangle \right) \\ &= \mathrm{Min}\left(\sum_i \left\{ \langle \psi_i| \, i\hbar \frac{d(|\psi_i\rangle)}{dt} \right\} - \prod_j \langle \psi_j| \, H \prod_i |\psi_i\rangle \right), \end{aligned} \tag{C.14}$$

where we denote $|\psi_i\rangle = \sum_{n_i}^{n_{max}} f_{n_i}^{[i]} |n_i\rangle$. In the third row Leibniz rule and local state orthonormality $\langle \psi_j | \psi_i \rangle = \delta_{i,j}$ is used. Eq. (C.14) can be optimized locally since, the derivative to acts only on local terms. For the state

at site k,

$$\begin{aligned}
&\frac{\partial}{\partial \langle\psi_k|}\left(\sum_i \left\{ \langle\psi_i| \, i\hbar \frac{d(|\psi_i\rangle)}{dt} \right\} - \prod_j \langle\psi_j| \, H \prod_i |\psi_i\rangle \right) = 0 \\
&\Rightarrow \frac{\partial}{\partial \langle\psi_k|}\left(\sum_i \left\{ \langle\psi_i| \, i\hbar \frac{d(|\psi_i\rangle)}{dt} \right\} - \prod_j \langle\psi_j| \, H^{[k]} + H_{rest} \prod_i |\psi_i\rangle \right) = 0 \\
&\Rightarrow \frac{\partial}{\partial \langle\psi_k|}\left(\sum_i \left\{ \langle\psi_i| \, i\hbar \frac{d(|\psi_i\rangle)}{dt} \right\} - \prod_j \langle\psi_j| \, H^{[k]} \prod_i |\psi_i\rangle + const. \right) = 0 \\
&\Rightarrow i\hbar \frac{d(|\psi_k\rangle)}{dt} - \prod_{<j>_k} \langle\psi_j| \, H^{[k]} \prod_{<l>_k} |\psi_l\rangle \, |\psi_k\rangle = 0.
\end{aligned} \tag{C.15}$$

The constant in the 3rd row denotes a constant with respect to $\langle\psi_k|$. Substituting eq. (C.7) into eq. (C.15) and using the definitions of eq. (C.8) the resulting equations of motion for the state elements are

$$i\hbar \frac{df_{n_i}^{[i]}}{dt} = \left(U\frac{(n_i-1)}{2} - \mu \right) n_i f_{n_i}^{[i]} - \Phi_i \sqrt{n_i} f_{n_i-1}^{[i]} - \Phi_i^* \sqrt{n_i+1} f_{n_i+1}^{[i]}. \tag{C.16}$$

The numerical integration of eq. (C.16) can be performed by standard Runge-Kutta algorithms. In this thesis a 4th order Runge-Kutta integration scheme is used. The error of the 4th order Runge-Kutta method scales as $O(dt^5)$. Using eq. (C.16) we can derive the equations of motion for the superfluid order parameter:

$$\begin{aligned}
&\frac{d\langle\hat{a}_i\rangle}{dt} = \sum_{n_i=0}^{n_{max}} \frac{df_{n_i}^{[i]*}}{dt} f_{n_i+1}^{[i]} \sqrt{n_i+1} + \sum_{n_i=0}^{n_{max}} f_{n_i}^{[i]*} \frac{df_{n_i+1}^{[i]}}{dt} \sqrt{n_i+1} \\
&\Rightarrow i\hbar \frac{d\phi_i}{dt} = -\Phi_i - \mu\phi_i + U \sum_{n_i}^{n_{max}} n_i \sqrt{n_i+1} f_{n_i}^{[i]*} f_{n_i+1}^{[i]}.
\end{aligned} \tag{C.17}$$

Eq. (C.17) is a generalization of the discretized Gross-Pitaevskii equation (DGPE) [168], valid for weakly interacting systems $U \ll J$. The connection to DGPE is clear if a coherent state $f_{n_i}^{[i]} = e^{-|\phi_i|^2/2} \phi_i^{n_i} / \sqrt{n_i!}$ approximation is considered. Substituting the coherent state to the interacting term in eq. (C.17) the signature interaction term of the DGPE equation is retrieved: $U|\phi_i|^2 \phi_i$. Furthermore, eq. (C.17) becomes closed, as it contains only mean fields, so there is no need of GA to time-evolve a weakly

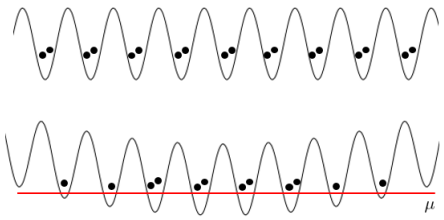


Figure C.1: Harmonic lattice and the addition of the trapping potential. Particles are confined in a finite area of space. If the local trap potential becomes higher than chemical potential, the lattice is empty.

interacting superfluid.

C.2.3 Trapped boson gasses

In experiments, particle clouds are trapped using harmonic potentials $V(\mathbf{r}) = 1/2V_0\mathbf{r}^2$. The characteristic trap frequency is much smaller than the frequency associated with the optical lattice in order to trap thousands of atoms, see fig. C.1. The trap couples a classical field to the particle number on a given site of the lattice. It can, thus, be absorbed by the chemical potential $\mu'(\mathbf{r}) = \mu - V(\mathbf{r})$ in the BH model. The phase spectrum of homogeneous BH model along the chemical potential axis is projected to the radial axis of the trapped cloud. The starting point of the projection is $(\mu/U, J/U)$, which corresponds to the centre of the trap. The final point, $(0, J/U)$, corresponds to the edge of the cloud. Beyond the radius $R_{cloud} \approx \sqrt{2\mu/V_0}$, the lattice is empty.

In fig. C.2, the local density and superfluid order parameter are plotted for various values of μ, in square lattices. The Gutzwiller wavefunction is the only computationally efficient algorithm for large scale systems and is used for trapped lattices considered in this thesis. The local variational algorithm (section C.2.1) is used for the ground state optimization. An important property of trapped atom clouds is that the edge of the system is always in the superfluid regime, since as $\mu \to 0$ the phase is not insulating for any non-vanishing hopping parameter J.

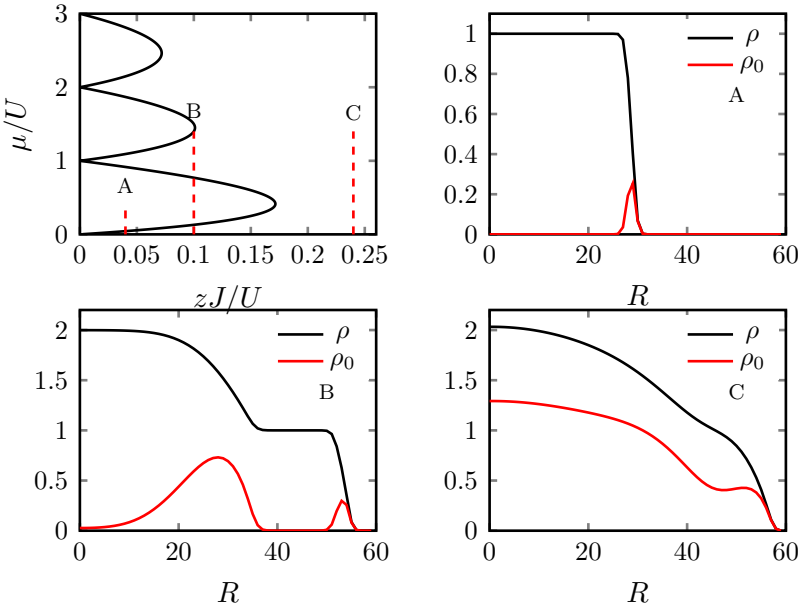


Figure C.2: *Top-Left*: First three Mott lobes analytically calculated using mean field theory. The perpendicular red lines show the part of the spectrum projected by a trapped atom cloud for various cases. The tip of the line corresponds to the centre of the cloud. At the edge of the cloud the chemical potential is effectivelly zero. *Top-Right, Bottom*: Local particle number and superfluid order parammeter plotted with respect to the distance from the centre of the trap.

Bibliography

[1] G. Vidal, J. I. Latorre, E. Rico, and A. Kitaev, Phys. Rev. Lett. **90**, 227902 (2003), URL http://link.aps.org/doi/10.1103/PhysRevLett.90.227902.

[2] F. Verstraete and J. I. Cirac, arXiv preprint cond-mat/0407066 (2004).

[3] G. Vidal, Phys. Rev. Lett. **98**, 070201 (2007).

[4] M. Levin and C. P. Nave, Phys. Rev. Lett. **99**, 120601 (2007), URL http://link.aps.org/doi/10.1103/PhysRevLett.99.120601.

[5] I. Bengtsson and K. Zyczkowski, *Geometry of quantum states: an introduction to quantum entanglement* (Cambridge University Press, 2007).

[6] M. B. Hastings, Journal of Statistical Mechanics: Theory and Experiment **2007**, P08024 (2007), URL http://stacks.iop.org/1742-5468/2007/i=08/a=P08024.

[7] F. G. Brandão and M. Horodecki, Nature physics **9**, 721 (2013).

[8] D. J. Luitz, N. Laflorencie, and F. Alet, Phys. Rev. B **91**, 081103 (2015), URL http://link.aps.org/doi/10.1103/PhysRevB.91.081103.

[9] A. Pal and D. A. Huse, Phys. Rev. B **82**, 174411 (2010), URL http://link.aps.org/doi/10.1103/PhysRevB.82.174411.

[10] P. Calabrese and J. Cardy, Journal of Statistical Mechanics: Theory and Experiment **2004**, P06002 (2004), URL http://stacks.iop.org/1742-5468/2004/i=06/a=P06002.

[11] P. Calabrese and J. Cardy, Journal of Physics A: Mathematical and Theoretical **42**, 504005 (2009), URL http://stacks.iop.org/1751-8121/42/i=50/a=504005.

[12] J. Cho, Phys. Rev. Lett. **113**, 197204 (2014), URL http://link.aps.org/doi/10.1103/PhysRevLett.113.197204.

[13] M. A. Metlitski and T. Grover, arXiv preprint arXiv:1112.5166 (2011).

[14] I. Frérot and T. Roscilde, Phys. Rev. Lett. **116**, 190401 (2016), URL http://link.aps.org/doi/10.1103/PhysRevLett.116.190401.

[15] H. Li and F. D. M. Haldane, Phys. Rev. Lett. **101**, 010504 (2008), URL http://link.aps.org/doi/10.1103/PhysRevLett.101.010504.

[16] N. Regnault, B. A. Bernevig, and F. D. M. Haldane, Phys. Rev. Lett. **103**, 016801 (2009), URL http://link.aps.org/doi/10.1103/PhysRevLett.103.016801.

[17] L. Fidkowski, Phys. Rev. Lett. **104**, 130502 (2010), URL http://link.aps.org/doi/10.1103/PhysRevLett.104.130502.

[18] F. Pollmann, A. M. Turner, E. Berg, and M. Oshikawa, Phys. Rev. B **81**, 064439 (2010), URL http://link.aps.org/doi/10.1103/PhysRevB.81.064439.

[19] V. Alba, M. Haque, and A. M. Läuchli, Phys. Rev. Lett. **108**, 227201 (2012), URL http://link.aps.org/doi/10.1103/PhysRevLett.108.227201.

[20] M. Serbyn, A. A. Michailidis, D. A. Abanin, and Z. Papić, Phys. Rev. Lett. **117**, 160601 (2016), URL http://link.aps.org/doi/10.1103/PhysRevLett.117.160601.

[21] S. R. White, Phys. Rev. Lett. **69**, 2863 (1992), URL http://link.aps.org/doi/10.1103/PhysRevLett.69.2863.

[22] C. Eckart and G. Young, Psychometrika **1**, 211 (1936).

[23] B. Pirvu, G. Vidal, F. Verstraete, and L. Tagliacozzo, Phys. Rev. B **86**, 075117 (2012), URL https://link.aps.org/doi/10.1103/PhysRevB.86.075117.

[24] D. Perez-Garcia, F. Verstraete, M. M. Wolf, and J. I. Cirac, arXiv preprint quant-ph/0608197 (2006).

[25] R. Orús, Annals of Physics **349**, 117 (2014).

[26] B. Pirvu, V. Murg, J. I. Cirac, and F. Verstraete, New Journal of Physics **12**, 025012 (2010), URL http://stacks.iop.org/1367-2630/12/i=2/a=025012.

[27] F. Fröwis, V. Nebendahl, and W. Dür, Phys. Rev. A **81**, 062337 (2010), URL http://link.aps.org/doi/10.1103/PhysRevA.81.062337.

[28] G. M. Crosswhite and D. Bacon, Phys. Rev. A **78**, 012356 (2008), URL http://link.aps.org/doi/10.1103/PhysRevA.78.012356.

[29] K. G. Wilson, Rev. Mod. Phys. **47**, 773 (1975), URL http://link.aps.org/doi/10.1103/RevModPhys.47.773.

[30] I. P. McCulloch, Journal of Statistical Mechanics: Theory and Experiment **2007**, P10014 (2007), URL http://stacks.iop.org/1742-5468/2007/i=10/a=P10014.

[31] J. Liesen and Z. Strakos, *Krylov subspace methods: principles and analysis* (OUP Oxford, 2012).

[32] S. R. White, Phys. Rev. B **72**, 180403 (2005), URL http://link.aps.org/doi/10.1103/PhysRevB.72.180403.

[33] C. Hubig, I. P. McCulloch, U. Schollwöck, and F. A. Wolf, Physical Review B **91**, 155115 (2015).

[34] U. Schollwöck, Annals of Physics **326**, 96 (2011).

[35] A. Weichselbaum, Annals of Physics **327**, 2972 (2012), ISSN 0003-4916, URL http://www.sciencedirect.com/science/article/pii/S0003491612001121.

[36] B. Bauer, P. Corboz, R. Orús, and M. Troyer, Phys. Rev. B **83**, 125106 (2011), URL http://link.aps.org/doi/10.1103/PhysRevB.83.125106.

[37] Z.-C. Yang, C. Chamon, A. Hamma, and E. R. Mucciolo, Phys. Rev. Lett. **115**, 267206 (2015), URL http://link.aps.org/doi/10.1103/PhysRevLett.115.267206.

[38] E. H. Lieb and D. W. Robinson, in *Statistical Mechanics* (Springer, 1972), pp. 425–431.

[39] G. Vidal, Phys. Rev. Lett. **91**, 147902 (2003), URL http://link.aps.org/doi/10.1103/PhysRevLett.91.147902.

[40] S. R. White and A. E. Feiguin, Phys. Rev. Lett. **93**, 076401 (2004), URL http://link.aps.org/doi/10.1103/PhysRevLett.93.076401.

[41] J. Haegeman, J. I. Cirac, T. J. Osborne, I. Pižorn, H. Verschelde, and F. Verstraete, Phys. Rev. Lett. **107**, 070601 (2011).

[42] J. Haegeman, C. Lubich, I. Oseledets, B. Vandereycken, and F. Verstraete, arXiv preprint arXiv:1408.5056 (2014).

[43] J. Haegeman, T. J. Osborne, and F. Verstraete, Phys. Rev. B **88**, 075133 (2013), URL http://link.aps.org/doi/10.1103/PhysRevB.88.075133.

[44] L. Vanderstraeten, F. Verstraete, and J. Haegeman, Phys. Rev. B **92**, 125136 (2015), URL http://link.aps.org/doi/10.1103/PhysRevB.92.125136.

[45] N. Nakatani, S. Wouters, D. Van Neck, and G. K.-L. Chan, The Journal of chemical physics **140**, 024108 (2014).

[46] V. Zauner, D. Draxler, L. Vanderstraeten, M. Degroote, J. Haegeman, M. M. Rams, V. Stojevic, N. Schuch, and F. Verstraete, New Journal of Physics **17**, 053002 (2015), URL http://stacks.iop.org/1367-2630/17/i=5/a=053002.

[47] D. Pekker and B. K. Clark, arXiv preprint arXiv:1410.2224 (2014).

[48] X. Yu, D. Pekker, and B. K. Clark, arXiv preprint arXiv:1509.01244 (2015).

[49] V. Khemani, F. Pollmann, and S. L. Sondhi, Phys. Rev. Lett. **116**, 247204 (2016), URL http://link.aps.org/doi/10.1103/PhysRevLett.116.247204.

[50] S. P. Lim and D. N. Sheng, Phys. Rev. B **94**, 045111 (2016), URL http://link.aps.org/doi/10.1103/PhysRevB.94.045111.

[51] F. Verstraete and J. I. Cirac, Phys. Rev. Lett. **104**, 190405 (2010), URL http://link.aps.org/doi/10.1103/PhysRevLett.104.190405.

[52] J. Haegeman, J. I. Cirac, T. J. Osborne, and F. Verstraete, Phys. Rev. B **88**, 085118 (2013), URL http://link.aps.org/doi/10.1103/PhysRevB.88.085118.

[53] E. Stoudenmire and S. R. White, Annual Review of Condensed Matter Physics **3**, 111 (2012), http://dx.doi.org/10.1146/annurev-conmatphys-020911-125018, URL http://dx.doi.org/10.1146/annurev-conmatphys-020911-125018.

[54] Y. Ge and J. Eisert, New Journal of Physics **18**, 083026 (2016), URL http://stacks.iop.org/1367-2630/18/i=8/a=083026.

[55] J. Jordan, R. Orús, G. Vidal, F. Verstraete, and J. I. Cirac, Phys. Rev. Lett. **101**, 250602 (2008), URL http://link.aps.org/doi/10.1103/PhysRevLett.101.250602.

[56] R. Orús and G. Vidal, Phys. Rev. B **80**, 094403 (2009), URL http://link.aps.org/doi/10.1103/PhysRevB.80.094403.

[57] H. C. Jiang, Z. Y. Weng, and T. Xiang, Phys. Rev. Lett. **101**, 090603 (2008), URL http://link.aps.org/doi/10.1103/PhysRevLett.101.090603.

[58] N. Halko, P.-G. Martinsson, and J. A. Tropp, SIAM review **53**, 217 (2011).

[59] M. Lubasch, J. I. Cirac, and M.-C. Bañuls, New Journal of Physics **16**, 033014 (2014), URL http://stacks.iop.org/1367-2630/16/i=3/a=033014.

[60] N. Schuch, M. M. Wolf, F. Verstraete, and J. I. Cirac, Phys. Rev. Lett. **98**, 140506 (2007), URL http://link.aps.org/doi/10.1103/PhysRevLett.98.140506.

[61] Z. Y. Xie, H. C. Jiang, Q. N. Chen, Z. Y. Weng, and T. Xiang, Phys. Rev. Lett. **103**, 160601 (2009), URL http://link.aps.org/doi/10.1103/PhysRevLett.103.160601.

[62] L. De Lathauwer, B. De Moor, and J. Vandewalle, SIAM journal on Matrix Analysis and Applications **21**, 1253 (2000).

[63] Z. Y. Xie, J. Chen, M. P. Qin, J. W. Zhu, L. P. Yang, and T. Xiang, Phys. Rev. B **86**, 045139 (2012), URL http://link.aps.org/doi/10.1103/PhysRevB.86.045139.

[64] G. Evenbly and G. Vidal, Phys. Rev. Lett. **115**, 180405 (2015), URL http://link.aps.org/doi/10.1103/PhysRevLett.115.180405.

[65] G. Vidal, Phys. Rev. Lett. **101**, 110501 (2008), URL http://link.aps.org/doi/10.1103/PhysRevLett.101.110501.

[66] M. Friesdorf, A. H. Werner, W. Brown, V. B. Scholz, and J. Eisert, Phys. Rev. Lett. **114**, 170505 (2015), URL http://link.aps.org/doi/10.1103/PhysRevLett.114.170505.

[67] M.-C. Chung and I. Peschel, Phys. Rev. B **64**, 064412 (2001), URL http://link.aps.org/doi/10.1103/PhysRevB.64.064412.

[68] P. W. Anderson, Phys. Rev. **109**, 1492 (1958), URL http://link.aps.org/doi/10.1103/PhysRev.109.1492.

[69] F. Evers and A. D. Mirlin, Rev. Mod. Phys. **80**, 1355 (2008), URL http://link.aps.org/doi/10.1103/RevModPhys.80.1355.

[70] A. Polkovnikov, K. Sengupta, A. Silva, and M. Vengalattore, Rev. Mod. Phys. **83**, 863 (2011), URL http://link.aps.org/doi/10.1103/RevModPhys.83.863.

[71] D. Basko, I. Aleiner, and B. Altshuler, Annals of physics **321**, 1126 (2006).

[72] I. V. Gornyi, A. D. Mirlin, and D. G. Polyakov, Phys. Rev. Lett. **95**, 206603 (2005), URL http://link.aps.org/doi/10.1103/PhysRevLett.95.206603.

[73] V. Oganesyan and D. A. Huse, Phys. Rev. B **75**, 155111 (2007), URL http://link.aps.org/doi/10.1103/PhysRevB.75.155111.

[74] M. Žnidarič, T. c. v. Prosen, and P. Prelovšek, Phys. Rev. B **77**, 064426 (2008), URL http://link.aps.org/doi/10.1103/PhysRevB.77.064426.

[75] A. D. Luca and A. Scardicchio, EPL (Europhysics Letters) **101**, 37003 (2013), URL http://stacks.iop.org/0295-5075/101/i=3/a=37003.

[76] F. Andraschko, T. Enss, and J. Sirker, Phys. Rev. Lett. **113**, 217201 (2014), URL http://link.aps.org/doi/10.1103/PhysRevLett.113.217201.

[77] M. Schreiber, S. S. Hodgman, P. Bordia, H. P. Lüschen, M. H. Fischer, R. Vosk, E. Altman, U. Schneider, and I. Bloch, Science **349**, 842 (2015), ISSN 0036-8075, http://science.sciencemag.org/content/349/6250/842.full.pdf, URL http://science.sciencemag.org/content/349/6250/842.

[78] J.-y. Choi, S. Hild, J. Zeiher, P. Schauß, A. Rubio-Abadal, T. Yefsah, V. Khemani, D. A. Huse, I. Bloch, and C. Gross, arXiv preprint arXiv:1604.04178 (2016).

[79] M. Rigol, V. Dunjko, and M. Olshanii, Nature **452**, 854 (2008).

[80] M. Jimbo, *Yang-Baxter equation in integrable systems*, vol. 10 (World Scientific, 1990).

[81] M. Serbyn, Z. Papić, and D. A. Abanin, Phys. Rev. Lett. **111**, 127201 (2013), URL http://link.aps.org/doi/10.1103/PhysRevLett.111.127201.

[82] D. A. Huse, R. Nandkishore, and V. Oganesyan, Phys. Rev. B **90**, 174202 (2014), URL http://link.aps.org/doi/10.1103/PhysRevB.90.174202.

[83] S. Inglis and L. Pollet, Phys. Rev. Lett. **117**, 120402 (2016), URL http://link.aps.org/doi/10.1103/PhysRevLett.117.120402.

[84] T. O'Brien, D. A. Abanin, G. Vidal, and Z. Papić, arXiv preprint arXiv:1608.03296 (2016).

[85] J. Z. Imbrie, Journal of Statistical Physics **163**, 998 (2016).

[86] V. Ros, M. Müller, and A. Scardicchio, Nuclear Physics B **891**, 420 (2015), ISSN 0550-3213, URL http://www.sciencedirect.com/science/article/pii/S0550321314003836.

[87] M. Serbyn, Z. Papić, and D. A. Abanin, Phys. Rev. X **5**, 041047 (2015), URL http://link.aps.org/doi/10.1103/PhysRevX.5.041047.

[88] S. D. Geraedts, R. Bhatt, and R. Nandkishore, arXiv preprint arXiv:1608.01328 (2016).

[89] D. M. Kennes and C. Karrasch, Phys. Rev. B **93**, 245129 (2016), URL http://link.aps.org/doi/10.1103/PhysRevB.93.245129.

[90] V. Hernandez, J. E. Roman, and V. Vidal, ACM Transactions on Mathematical Software (TOMS) **31**, 351 (2005).

[91] I. P. McCulloch, arXiv preprint arXiv:0804.2509 (2008).

[92] B. Bauer and C. Nayak, Journal of Statistical Mechanics: Theory and Experiment **2013**, P09005 (2013), URL http://stacks.iop.org/1742-5468/2013/i=09/a=P09005.

[93] P. Calabrese and A. Lefevre, Phys. Rev. A **78**, 032329 (2008), URL http://link.aps.org/doi/10.1103/PhysRevA.78.032329.

[94] V. A. Marcenko and L. A. Pastur, Mathematics of the USSR-Sbornik **1**, 457 (1967), URL http://stacks.iop.org/0025-5734/1/i=4/a=A01.

[95] C. Monthus, Entropy **18**, 122 (2016).

[96] W. De Roeck, F. Huveneers, M. Müller, and M. Schiulaz, Phys. Rev. B **93**, 014203 (2016), URL http://link.aps.org/doi/10.1103/PhysRevB.93.014203.

[97] W. De Roeck and F. Huveneers, in *From Particle Systems to Partial Differential Equations II* (Springer, 2015), pp. 173–192.

[98] N. Yao, C. Laumann, J. I. Cirac, M. Lukin, and J. Moore, arXiv preprint arXiv:1410.7407 (2014).

[99] M. Schiulaz, A. Silva, and M. Müller, Phys. Rev. B **91**, 184202 (2015), URL http://link.aps.org/doi/10.1103/PhysRevB.91.184202.

[100] Z. Papić, E. M. Stoudenmire, and D. A. Abanin, Annals of Physics **362**, 714 (2015), ISSN 0003-4916, URL http://www.sciencedirect.com/science/article/pii/S0003491615003280.

[101] M. P. A. Fisher, P. B. Weichman, G. Grinstein, and D. S. Fisher, Phys. Rev. B **40**, 546 (1989), URL http://link.aps.org/doi/10.1103/PhysRevB.40.546.

[102] T. Ohgoe, T. Suzuki, and N. Kawashima, Phys. Rev. B **86**, 054520 (2012), URL http://link.aps.org/doi/10.1103/PhysRevB.86.054520.

[103] B. Capogrosso-Sansone, i. m. c. G. m. c. Söyler, N. Prokof'ev, and B. Svistunov, Phys. Rev. A **77**, 015602 (2008), URL http://link.aps.org/doi/10.1103/PhysRevA.77.015602.

[104] J. Y. Gan, Y. C. Wen, J. Ye, T. Li, S.-J. Yang, and Y. Yu, Phys. Rev. B **75**, 214509 (2007), URL http://link.aps.org/doi/10.1103/PhysRevB.75.214509.

[105] D. R. Hofstadter, Phys. Rev. B **14**, 2239 (1976), URL http://link.aps.org/doi/10.1103/PhysRevB.14.2239.

[106] I. Bloch, Nature Physics **1**, 23 (2005).

[107] W. Zwerger, Journal of Optics B: Quantum and Semiclassical Optics **5**, S9 (2003), URL http://stacks.iop.org/1464-4266/5/i=2/a=352.

[108] C. Menotti, M. Lewenstein, T. Lahaye, and T. Pfau, AIP Conference Proceedings **970**, 332 (2008), URL http://scitation.aip.org/content/aip/proceeding/aipcp/10.1063/1.2839130.

[109] T. Lahaye, C. Menotti, L. Santos, M. Lewenstein, and T. Pfau, Reports on Progress in Physics **72**, 126401 (2009), URL http://stacks.iop.org/0034-4885/72/i=12/a=126401.

[110] C. Trefzger, C. Menotti, B. Capogrosso-Sansone, and M. Lewenstein, Journal of Physics B: Atomic, Molecular and Optical Physics **44**, 193001 (2011), URL http://stacks.iop.org/0953-4075/44/i=19/a=193001.

[111] W. Krauth, M. Caffarel, and J.-P. Bouchaud, Phys. Rev. B **45**, 3137 (1992), URL http://link.aps.org/doi/10.1103/PhysRevB.45.3137.

[112] P. Sengupta, L. P. Pryadko, F. Alet, M. Troyer, and G. Schmid, Phys. Rev. Lett. **94**, 207202 (2005), URL http://link.aps.org/doi/10.1103/PhysRevLett.94.207202.

[113] T. Kimura, Phys. Rev. A **84**, 063630 (2011), URL http://link.aps.org/doi/10.1103/PhysRevA.84.063630.

[114] K. Yamamoto, S. Todo, and S. Miyashita, Phys. Rev. B **79**, 094503 (2009), URL http://link.aps.org/doi/10.1103/PhysRevB.79.094503.

[115] T. Ohgoe, T. Suzuki, and N. Kawashima, Phys. Rev. Lett. **108**, 185302 (2012), URL http://link.aps.org/doi/10.1103/PhysRevLett.108.185302.

[116] E. Kim and M. Chan, Nature **427**, 225 (2004).

[117] D. Y. Kim and M. H. W. Chan, Phys. Rev. Lett. **109**, 155301 (2012), URL http://link.aps.org/doi/10.1103/PhysRevLett.109.155301.

[118] A. Haziot, X. Rojas, A. D. Fefferman, J. R. Beamish, and S. Balibar, Phys. Rev. Lett. **110**, 035301 (2013), URL http://link.aps.org/doi/10.1103/PhysRevLett.110.035301.

[119] M. W. Ray and R. B. Hallock, Phys. Rev. Lett. **100**, 235301 (2008), URL http://link.aps.org/doi/10.1103/PhysRevLett.100.235301.

[120] M. W. Ray and R. B. Hallock, Phys. Rev. Lett. **105**, 145301 (2010), URL http://link.aps.org/doi/10.1103/PhysRevLett.105.145301.

[121] Z. G. Cheng, J. Beamish, A. D. Fefferman, F. Souris, S. Balibar, and V. Dauvois, Phys. Rev. Lett. **114**, 165301 (2015), URL http://link.aps.org/doi/10.1103/PhysRevLett.114.165301.

[122] S. Ejima, F. Lange, and H. Fehske, Phys. Rev. Lett. **113**, 020401 (2014), URL http://link.aps.org/doi/10.1103/PhysRevLett.113.020401.

[123] Z.-C. Gu and X.-G. Wen, Phys. Rev. B **80**, 155131 (2009), URL http://link.aps.org/doi/10.1103/PhysRevB.80.155131.

[124] T. Holstein and H. Primakoff, Phys. Rev. **58**, 1098 (1940), URL http://link.aps.org/doi/10.1103/PhysRev.58.1098.

[125] V. Alba, M. Haque, and A. M. Läuchli, Phys. Rev. Lett. **110**, 260403 (2013), URL http://link.aps.org/doi/10.1103/PhysRevLett.110.260403.

[126] I. Frérot and T. Roscilde, Phys. Rev. B **92**, 115129 (2015), URL http://link.aps.org/doi/10.1103/PhysRevB.92.115129.

[127] M. C. Gutzwiller, Phys. Rev. Lett. **10**, 159 (1963), URL http://link.aps.org/doi/10.1103/PhysRevLett.10.159.

[128] K. Sheshadri, H. R. Krishnamurthy, R. Pandit, and T. V. Ramakrishnan, EPL (Europhysics Letters) **22**, 257 (1993), URL http://stacks.iop.org/0295-5075/22/i=4/a=004.

[129] G. G. Batrouni, F. Hébert, and R. T. Scalettar, Phys. Rev. Lett. **97**, 087209 (2006), URL http://link.aps.org/doi/10.1103/PhysRevLett.97.087209.

[130] J. Ye, arXiv preprint cond-mat/0503113 (2005).

[131] J. Jordan, R. Orús, and G. Vidal, Phys. Rev. B **79**, 174515 (2009), URL http://link.aps.org/doi/10.1103/PhysRevB.79.174515.

[132] S. Wessel, Phys. Rev. B **75**, 174301 (2007), URL http://link.aps.org/doi/10.1103/PhysRevB.75.174301.

[133] P. Corboz, Phys. Rev. B **94**, 035133 (2016), URL http://link.aps.org/doi/10.1103/PhysRevB.94.035133.

[134] J. R. Abo-Shaeer, C. Raman, J. M. Vogels, and W. Ketterle, Science **292**, 476 (2001), ISSN 0036-8075, http://science.sciencemag.org/content/292/5516/476.full.pdf, URL http://science.sciencemag.org/content/292/5516/476.

[135] J. Struck, M. Weinberg, C. Ölschläger, P. Windpassinger, J. Simonet, K. Sengstock, R. Höppner, P. Hauke, A. Eckardt, M. Lewenstein, et al., Nature Physics **9**, 738 (2013).

[136] Y.-J. Lin, R. L. Compton, K. Jiménez-García, J. V. Porto, and I. B. Spielman, Nature **462**, 628 (2009).

[137] M. Aidelsburger, M. Atala, M. Lohse, J. T. Barreiro, B. Paredes, and I. Bloch, Phys. Rev. Lett. **111**, 185301 (2013), URL http://link.aps.org/doi/10.1103/PhysRevLett.111.185301.

[138] H. Miyake, G. A. Siviloglou, C. J. Kennedy, W. C. Burton, and W. Ketterle, Phys. Rev. Lett. **111**, 185302 (2013), URL http://link.aps.org/doi/10.1103/PhysRevLett.111.185302.

[139] M. A. Cazalilla, R. Citro, T. Giamarchi, E. Orignac, and M. Rigol, Rev. Mod. Phys. **83**, 1405 (2011), URL http://link.aps.org/doi/10.1103/RevModPhys.83.1405.

[140] M. Rigol and A. Muramatsu, Phys. Rev. Lett. **93**, 230404 (2004), URL http://link.aps.org/doi/10.1103/PhysRevLett.93.230404.

[141] S. Aktaş and Ü. Atav, arXiv preprint arXiv:1408.3323 (2014).

[142] A. Jreissaty, J. Carrasquilla, and M. Rigol, Phys. Rev. A **88**, 031606 (2013), URL http://link.aps.org/doi/10.1103/PhysRevA.88.031606.

[143] K. Winkler, G. Thalhammer, F. Lang, R. Grimm, J. H. Denschlag, A. Daley, A. Kantian, H. Büchler, and P. Zoller, Nature **441**, 853 (2006).

[144] J. P. Ronzheimer, M. Schreiber, S. Braun, S. S. Hodgman, S. Langer, I. P. McCulloch, F. Heidrich-Meisner, I. Bloch, and U. Schneider, Phys. Rev. Lett. **110**, 205301 (2013), URL http://link.aps.org/doi/10.1103/PhysRevLett.110.205301.

[145] U. Schneider, L. Hackermüller, J. P. Ronzheimer, S. Will, S. Braun, T. Best, I. Bloch, E. Demler, S. Mandt, D. Rasch, et al., Nature Physics **8**, 213 (2012).

[146] M. Jreissaty, J. Carrasquilla, F. A. Wolf, and M. Rigol, Phys. Rev. A **84**, 043610 (2011), URL http://link.aps.org/doi/10.1103/PhysRevA.84.043610.

[147] D. Jaksch, V. Venturi, J. I. Cirac, C. J. Williams, and P. Zoller, Phys. Rev. Lett. **89**, 040402 (2002), URL http://link.aps.org/doi/10.1103/PhysRevLett.89.040402.

[148] M. Snoek, EPL (Europhysics Letters) **95**, 30006 (2011), URL http://stacks.iop.org/0295-5075/95/i=3/a=30006.

[149] E. Hairer, C. Lubich, and M. Roche (1989).

[150] J. Nickolls, I. Buck, M. Garland, and K. Skadron, Queue **6**, 40 (2008), ISSN 1542-7730, URL http://doi.acm.org/10.1145/1365490.1365500.

[151] C. J. Kennedy, W. C. Burton, W. C. Chung, and W. Ketterle, Nature Physics (2015).

[152] D. Petrosyan, B. Schmidt, J. R. Anglin, and M. Fleischhauer, Phys. Rev. A **76**, 033606 (2007), URL http://link.aps.org/doi/10.1103/PhysRevA.76.033606.

[153] F. Heidrich-Meisner, S. R. Manmana, M. Rigol, A. Muramatsu, A. E. Feiguin, and E. Dagotto, Phys. Rev. A **80**, 041603 (2009), URL http://link.aps.org/doi/10.1103/PhysRevA.80.041603.

[154] D. Muth, D. Petrosyan, and M. Fleischhauer, Phys. Rev. A **85**, 013615 (2012), URL http://link.aps.org/doi/10.1103/PhysRevA.85.013615.

[155] K. Rodriguez, S. R. Manmana, M. Rigol, R. M. Noack, and A. Muramatsu, New Journal of Physics **8**, 169 (2006), URL http://stacks.iop.org/1367-2630/8/i=8/a=169.

[156] J. Ren, Y.-Z. Wu, and X.-F. Xu, Scientific reports **5** (2015).

[157] A. R. Kolovsky, Phys. Rev. A **82**, 011601 (2010), URL http://link.aps.org/doi/10.1103/PhysRevA.82.011601.

[158] F. Verstraete, M. M. Wolf, D. Perez-Garcia, and J. I. Cirac, Phys. Rev. Lett. **96**, 220601 (2006), URL https://link.aps.org/doi/10.1103/PhysRevLett.96.220601.

[159] S. Iyer, V. Oganesyan, G. Refael, and D. A. Huse, Phys. Rev. B **87**, 134202 (2013), URL https://link.aps.org/doi/10.1103/PhysRevB.87.134202.

[160] Z. Papić, E. M. Stoudenmire, and D. A. Abanin, Annals of Physics **362**, 714 (2015), ISSN 0003-4916, URL http://www.sciencedirect.com/science/article/pii/S0003491615003280.

[161] N. Y. Yao, C. R. Laumann, J. I. Cirac, M. D. Lukin, and J. E. Moore, Phys. Rev. Lett. **117**, 240601 (2016), URL https://link.aps.org/doi/10.1103/PhysRevLett.117.240601.

[162] M. van Horssen, E. Levi, and J. P. Garrahan, Phys. Rev. B **92**, 100305 (2015), URL https://link.aps.org/doi/10.1103/PhysRevB.92.100305.

[163] A. Chandran, A. Pal, C. R. Laumann, and A. Scardicchio, Phys. Rev. B **94**, 144203 (2016), URL https://link.aps.org/doi/10.1103/PhysRevB.94.144203.

[164] D. Tamascelli, R. Rosenbach, and M. B. Plenio, Phys. Rev. E **91**, 063306 (2015), URL http://link.aps.org/doi/10.1103/PhysRevE.91.063306.

[165] J. R. Shewchuk, Tech. Rep., Pittsburgh, PA, USA (1994).

[166] E. Polak and G. Ribière, Rev. Francaise Informat Recherche Operationnelle, 3e. Année **16**, 35 (1969).

[167] K. Kreutz-Delgado, arXiv preprint arXiv:0906.4835 (2009).

[168] J.-K. Xue, A.-X. Zhang, and J. Liu, Phys. Rev. A **77**, 013602 (2008), URL http://link.aps.org/doi/10.1103/PhysRevA.77.013602.